Assessment of microstructure and mechanical properties of dual phase C-Mn AHSS during thermomechanical processing via electron microscopy and high speed nanoindentation

A thesis

Submitted

by

Chavan Akash Naik

In partial fulfillment of the requirements for the award of the degree of

Doctor of Philosophy

In

Materials Engineering

Under the supervision of

Dr. Jai Prakash Gautam	**Dr. P. Sudharshan Phani**
Professor, School of Engineering Sciences and Technology, University of Hyderabad	Professor, School of Engineering Sciences and Technology, University of Hyderabad

School of Engineering Sciences and Technology,

University of Hyderabad, Hyderabad,

India.

DECLARATION

I, **CHAVAN AKASH NAIK** declare that this thesis work entitled "**Assessment of microstructure and mechanical properties of dual phase C-Mn AHSS during thermomechanical processing via electron microscopy and high speed nanoindentation"**, submitted in partial fulfillment of the requirements for the award of **Doctor of Philosophy**, in Materials Engineering at the School of Engineering Sciences and Technology (SEST), University of Hyderabad is completely my own work except for those referred. This work was carried out under the supervision of **Dr. Jai Prakash Gautam** and **Dr. Sudharshan Phani Pardhasaradhi**. This report is a record of bonafide work carried out by me and the results incorporated in it have not been reproduced/copied from any source. This work has not been submitted to any other University or Institute for the award of any other degree or equivalent.

CHAVAN AKASH NAIK

Reg. No.: 19ETPM01
School of Engineering Sciences and Technology
University of Hyderabad

CERTIFICATE

This is to certify that the thesis work entitled **“Assessment of microstructure and mechanical properties of dual phase C-Mn AHSS during thermomechanical processing via electron microscopy and high speed nanoindentation”**, submitted by **CHAVAN AKASH NAIK** bearing Reg. No. **19ETPM01** in partial fulfillment of the requirements for the award of the degree of **Doctor of Philosophy** in **Materials Engineering** is a bonafide record of the work that has been carried out by him under my supervision. This thesis has not been submitted previously in part or in full to this or any other University or Institution for the award of any degree or diploma.

Thesis Supervisor

Dr. Jai Prakash Gautam
Professor, School of Engineering
Sciences and Technology,
University of Hyderabad

Dr. Jai Prakash Gautam
Professor, SEST
University of Hyderabad
Hyderabad-500 046.

Dr. P. Sudharshan Phani
Professor, School of Engineering
Sciences and Technology,
University of Hyderabad

Approved by

2/9/2024

Dr. *Jai Prakash Gautam*
Dean,
School of Engineering Sciences and Technology,
University of Hyderabad

प्रो. जय प्रकाश गौतम
Prof. Jai Prakash Gautam
डीन /DEAN
एस.ई.एस.टी / School of Engineering Sciences & Technology
हैदराबाद विश्वविद्यालय
UNIVERISTY OF HYDERABAD
हैदराबाद / Hyderabad - 500046

CERTIFICATE

This is to certify that the thesis entitled "**Assessment of microstructure and mechanical properties of dual phase C-Mn AHSS during thermomechanical processing via electron microscopy and high speed nanoindentation**" submitted by **CHAVAN AKASH NAIK** bearing registration number **19ETPM01** in partial fulfillment of the requirements for the award of **Doctor of Philosophy,** in **Materials Engineering** at the School of Engineering Sciences and Technology (SEST) is a bonafide work carried out by him under my supervision and guidance.

This thesis is free from plagiarism and has not been submitted previously in part or in full to this or any other University or Institution for the award of any degree or diploma.

a. Part of this thesis has been published in,
   1. *Materials today communications,*
      https://doi.org/10.1016/j.mtcomm.2023.107696.

Further, the student has passed the following courses towards the fulfillment of coursework requirements for Ph.D.

Course Code	Title of the course	Credits	Results
PD801	RESEARCH METHODOLOGY	4	Pass
PD802	MATERIALS PROCESSING & CHARACTERIZATION LABORATORY	4	Pass
PD803	ADVANCED ENGINEERING MATHEMATICS	4	Pass
PD804	THERMODYNAMICS AND PHASE EQUILIBRIA OF MATERIALS	4	Pass
PD807	RESEARCH AND PUBLICATION ETHICS	2	Pass

Supervisor
School
Dr. Jai Prakash Gautam
Professor, SEST
University of Hyderabad
Hyderabad-500 046.

2/4/2024
Dean of
प्रो. जय प्रकाश गौतम
Prof. Jai Prakash Gautam
डीन /DEAN
एस.ई.एस.टी / School of Engineering Sciences & Technology
हैदराबाद विश्वविद्यालय
UNIVERISTY OF HYDERABAD
हैदराबाद / Hyderabad - 500046

ACKNOWLEDGEMENTS

First and foremost, I express my deep sense of gratitude and respect to my research supervisor ***Prof. Jai Prakash Gautam,*** for his keen interest, constant and valuable guidance, strong motivation, and constant encouragement during my research work.
I express my deep sense of gratitude and respect to my research co-supervisor ***Prof. Sudharshan Phani Pardhasaradhi,*** for helping me with Nanoindentation testing, analysis, his keen interest, constant and valuable guidance, strong motivation, and encouragement during my research work. I thank Director ARCI for granting permission to carry out the experiments at ARCI.

I express my deep sense of gratitude and respect to my research collaborator ***Prof. Leo A.I. Kestens and Pina Mecozzi*** *Ghent University, Ghent, Belgium* for helping me with all the technical discussions and valuable guidance, during my research work.

My doctoral review committee members ***Prof. Swati Ghosh Acharyya and Dr. Venkata Girish Kotnur*** have been helpful, critical and supportive over the last several years in making this work better. I am also thankful to the Dean of School of Engineering Sciences and Technology, ***Prof. Jai Prakash Gautam*** and all other faculties in the department for providing me the facilities to carry out my research work.
I express

I would also like to thank the technicians and non-teaching staff of SEST.

I would like to thank Tata Steel Research, (RD&T), IJmuiden, The Netherlands for supplying the materials and DST FIST and DST PURSE for funding the instrumentation facility (FESEM-EBSD).

I would like to thank University Grants Commission (UGC), Ministry of Tribal Affairs Government of India for proving fellowship in the form of NFHE-ST.

I express my gratitude to Dr. Damodar, Dr. Janakiram, Dr. Vamsi Krishna Rentala, Dr. Aqil, Sarath Kumar Busi, Harita Seekala, Subhadeep, Swati, Harita, Deekshit, Hasan, Dr. Kamal, Dr. Sunil, Dr. Ravikiran, Dr. Feba, Dr. Vikas, Dr. Charan, Sourabh, Sushmita, Jagdeesh, Pawan, Srujan, Sreenu, Charan, Vinay, Nitin, Dr. Pooja, Dr. Razi, Vinod and the entire team led by Prof. Jai Prakash Gautam. They provided invaluable assistance with numerous challenging problems sets and evolved into some of my cherished friends.

Lastly, I thank my mom-dad and brother for always supporting me in every endeavour. I would probably be somewhere else if it were not for my family's invincible and contagious optimism in me.

CHAVAN AKASH NAIK

Table of contents

Chapter 4 The influence of coiling temperature and cooling rate on microstructure and mechanical properties of dual phase microstructures 52

List of Tables

List of Figures

Abstract

This study employs a correlative methodology, utilizing nanoindentation and electron microscopy, to understand the microstructure and local mechanical properties of Advanced High Strength Steels (AHSS). These steels consist of a ferrite matrix combined with a reinforcing secondary constituent such as pearlite, bainite, or martensite. The initial microstructure is obtained by hot rolling above the austenite non-recrystallization temperature (TnR) and subsequent coiling at various transformation temperatures. This process resulted in microstructures comprising of ferrite combined with pearlite, bainite, and martensite, while maintaining a similar nominal carbon content. Subsequent processing, including cold rolling and annealing in the recrystallization and intercritical regimes, was employed to study the microstructural and mechanical property evolution. Local mechanical properties were assessed using high-speed nanoindentation mapping. Hardness data was deconvoluted using a clustering algorithm to determine the hardness of individual constituents. , Excellent agreement between microstructure and hardness at the micrometer length scale was observed in all cases. Despite identical nominal compositions, the three distinct dual-phase initial microstructures exhibited differences in the area fraction and hardness of ferrite and secondary constituents. Similar trend was observed after subsequent thermomechanical processing, such as cold rolling, recrystallization, and intercritical annealing, the experimental observations were reconciled based on processing conditions and the length scale of the microstructure and potential underlying mechanisms are presented. This study showcases the capability of nanoindentation mapping to capture local variations in hardness at the length scale encountered in DP steels, opening avenues for correlative characterization and the development of next-generation AHSS and multiphase steels.

Chapter 1 Introduction

Throughout history, automotive manufacturers globally have opted to utilize steel as their predominant material. The body weight of the average car is made up of about 70% steel. The evolution of dual-phase steel, possessing a combination of strength, lightweight, and formability, has profoundly transformed the automotive sector across a range of applications [1–3]. Its special characteristics aid in improving fuel economy, crashworthiness, and manufacturing procedures that are affordable[4,5]. Currently the steel industry's focus is on third generation AHSS, which have a complex microstructure consisting of different phases such as retained austenite, bainite, ferrite, and martensite. Dual phase steel is still a key component for satisfying these changing expectations as the automotive industry works to improve safety, effectiveness, and sustainability. To increase passenger safety and vehicle performance, vehicle weight reduction is currently the top objective for the automobile industry[3–5]. High strength steels and the Advanced High strength steels offer a persuasively plausible solution to the aforementioned conflicting needs by putting forth the idea of lightweight design.

1.1 High strength and advanced high strength steels:

Steels that have a tensile strength of more than 550 MPa are generally considered to be high strength steels. In order to improve their strength, they are produced utilising specific alloying and heat treatment methods. High strength steels are more durable, deformation resistant, and capable of bearing more weight than conventional steels. The development of AHSS grades has a specific goal of offering materials with outstanding mechanical characteristics, such as high tensile strength, excellent ductility, increased energy absorption during deformation, and exceptional resistance to fracture and fatigue. The use of lightweight materials with superior crash performance is essential for both the safety and fuel efficiency of automobiles, and AHSS is an ideal material for this application because of its specific combination of properties. Fig. 1-1 below illustrates the relationship between strength and elongation to fracture for diverse steels. Advanced High-Strength Steels exhibit varying strength and elongation properties based on different steel grades to cater to multiple applications.

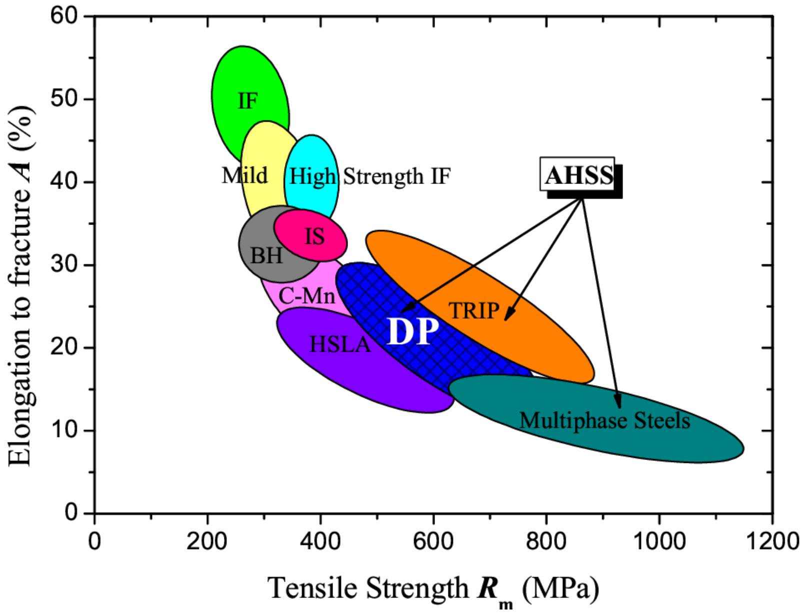

Figure 1-1: Tensile strength-to-total elongation relationships for low strength, HSS, and AHSS steels [6].

1.2 HSS and AHSS usage in Future steel vehicles (FSV):

The Future Steel Vehicle (FSV) project, led by WorldAutoSteel and Edag Inc, aims to develop and promote new high-strength steels for lightweight design in electric and conventional vehicles, continuing the evolution of steel in the automotive industry[7]. Fig. 1-2 depicts the utilization of diverse steel grades in fabrication of the car body components within the automotive industry. In the automotive industry, the use of steel is expected to continue in the future due to its numerous advantages, such as strength, durability, and cost-effectiveness. However, advancements in steel technology are likely to lead to the development of new types of steel and manufacturing processes[2,8]. AHSS is already being used in modern vehicles, offering improved strength and reduced weight compared to traditional steel. The future will likely see further development of AHSS grades, allowing automakers to create lighter and more fuel-efficient vehicles while maintaining structural integrity and safety. Ultra HSS is an even stronger and lighter type of steel that is currently being researched and developed. It has the potential to be used in critical areas of vehicles, such as crash zones, to enhance safety without adding significant weight.

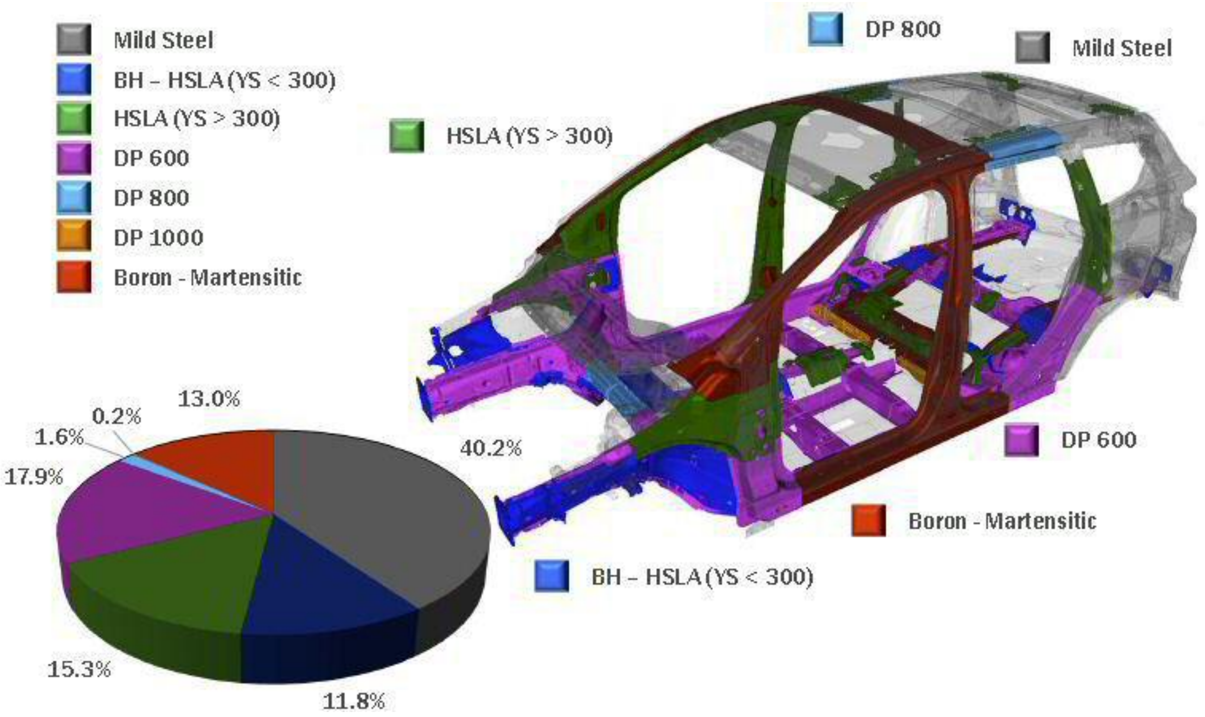

Figure 1-2: Different grades of steels in automotive body[3].

1.3 Thermomechanical processing of HSS/AHSS

TMCP (thermomechanical control processing) is essential in the production of high strength steels and advanced high strength steels [5,9], It combines heat treatment and the mechanical deformation to tailor the microstructure and the mechanical properties of steel. TMCP allows for specific control of grain size, phase distribution, and mechanical strength. The thermomechanical processing of HSS and AHSS typically involves hot rolling, cooling, coiling, cold rolling and annealing, including inter-critical annealing. All these processes will be investigated in the present study for a specific composition. Fig. 1-3 shows a schematic of these thermomechanical processing steps with specific reference to this work.

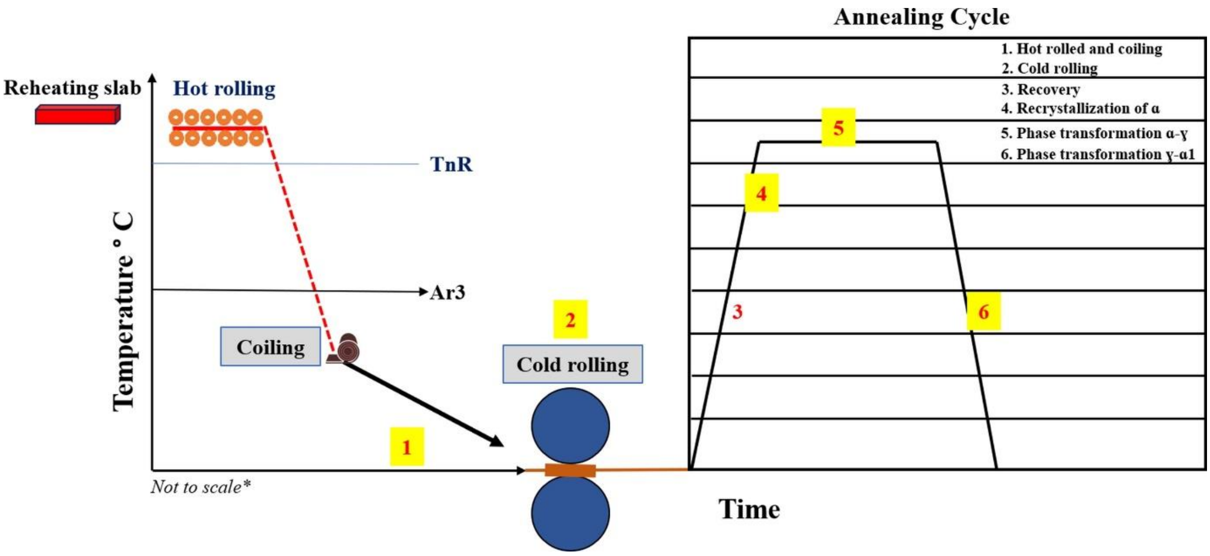

Figure 1-3: Schematic of thermomechanical processing of AHSS used in this work.

The steel slab is reheated to homogenize the material. The presence of microalloying components and the chemical composition affect the reheating temperature and time. This is followed by hot rolling, which involves heating the steel above the temperature of recrystallization in order to reduce its thickness. During hot rolling, the steel's initial microstructure develops. After hot rolling, the steel goes through a controlled rapid cooling procedure. Among the methods that can be utilised to speed up cooling include air cooling, direct water spray, and water quenching. The cooling rate and cooling mediums are carefully regulated to produce an appropriate microstructure. Coiling is the intermediate step during cooling where the desired microstructures are produced and avoid the development of undesired phases at different temperatures and varying cooling rates. After coiling, cold rolling is done to further decrease the thickness and enhance its surface finish. Additionally, cold rolling increases the material's strength via strain hardening. Subsequently annealing is carried out, which causes other significant structural changes in the microstructure as a result of phenomena like recovery, recrystallization, phase transformation and tempering.

In terms of microstructural changes, during heating of dual phase steels, depending on the initial microstructure several changes can occur, such as cementite spheroidization, bainite and martensite tempering / decomposition, ferrite recovery and recrystallization etc [10–12]. The rate of heating, chemical composition, and the amount of cold rolling all play an important role in determining this. Furthermore, during intercritical annealing multiple phenomena such as ferrite recrystallization (α), carbide dissolution, austenite (γ) nucleation and growth, etc. can concurrently occur. The degree of austenite nucleation depends on the temperature during the phase change, the soaking period, and its chemical composition. Finally, upon rapid cooling, the austenite transforms and forms martensite, ferrite recrystallizes and forms the ferrite-martensite dual phase structure. After formation of dual phase structure with ferrite as matrix and the second phase as martensite, tempering can be carried out to improve the ductility.

Most studies on industrial-grade high-strength steel or low-carbon steel have focussed on the processing, chemical composition, and competition between ferrite recrystallization and austenite transformation in intercritical annealing regime [13–15]. A systematic comprehensive study of different thermomechanical processing steps is yet to be reported. Such a study will contribute to a holistic interpretation of all the micro-structural changes during processing of advanced high strength steels.

1.4 Motivation

Most AHSS are dual or multi-phase steels and there is a continuous ongoing effort globally to modify the processing to obtain the desired microstructure and thereby the properties. Establishing the inter-relationship between the processing, microstructural and mechanical characteristics of the distinct constituents of these AHSS, then becomes the key to developing AHSS with the desired mechanical properties. In this regard, close coupling of microstructure and mechanical properties at the micrometer length is critically required. Hence, a comprehensive study of the microstructure and local mechanical properties of dual phase steels during various processing steps such as hot rolling, coiling, cold rolling and annealing is carried out to establish the much-needed relationship between processing, microstructure and property at the micrometer length scale.

1.5 Thesis objectives

The main objective of the thesis is to assess the correlation between microstructural and mechanical properties at the micrometer length scale during each stage of thermomechanical processing, including hot rolling, coiling, cold rolling, recrystallization annealing, and intercritical annealing. Three distinct microstructures, ferrite-pearlite (FP), ferrite-bainite (FB), and ferrite-martensite (FM) with a fixed carbon content but different distribution of carbon and thereby the strengthening phase are developed by varying the hot rolling and coiling conditions followed by cold rolling and annealing. The different samples thus obtained exhibit different secondary constituents, morphologies, etc. However, how the various processing steps influence the microstructure and its subsequent effect on local mechanical properties is not well investigated. These aspects thus form the basis for framing the following objectives.

1. Obtain dual phase microstructures with different matrix and secondary phases/constituents (ferrite-pearlite, ferrite-bainite and ferrite-martensite) at a fixed nominal composition.
2. Thermomechanical processing of the different samples via cold rolling, recrystallization annealing and intercritical annealing
3. Microstructural characterization using SEM and EBSD and mechanical characterization using high speed nanoindentation mapping.
4. Deconvolution of the high speed nanoindentation mapping data and coupling with microstructural data
5. Establishing the relationship between the micro-structure and the mechanical property at micron scale during all the stages of processing including hot rolling followed by coiling, cold rolling, recrystallization annealing and intercritical annealing.

1.6 Outline of thesis

This thesis is divided into eight chapters that cover a variety of topics related to the research conducted throughout the tenure of the PhD work.

Chapter 1: This chapter presents an introduction and background to the current thesis.

Chapter 2: This chapter presents a literature review on major process parameters and their effects during thermomechanical processing steps such as hot rolling and coiling, cold rolling, recrystallization annealing and intercritical annealing.

Chapter 3: This chapter provides details of the AHSS steel grade chosen with the chemical compositions and thermomechanical processing histories for all the steps. Details of experimental setup, microstructural and mechanical characterization methods, and sample preparation required for microstructural analysis are all provided. Also, the details of post-processing procedures for analysing the experimental data are presented.

Chapter 4: This chapter discusses the development of the microstructures at different coiling temperatures after hot rolling and its effect on morphology and mechanical property of each individual phases. Assessment of the relationship between microstructure and mechanical property at micrometer length scale studied by high speed nanoindentation and electron microscopy is presented.

Chapter 5: This chapter discusses the effect of cold rolling to 60% and 80% after hot rolling and coiling for the different dual phase microstructures. The variation in mechanical properties of individual constituents with cold rolling is presented along with correlations with microstructure.

Chapter 6: This chapter presents the microstructural changes and corresponding mechanical properties of ferrite and secondary constituents such as pearlite, bainite and martensite upon annealing treatment at 725°C. The effect of second phase constituents on the recrystallization kinetics and the underlying mechanisms are presented.

Chapter 7: This chapter presents the microstructural changes and corresponding mechanical property during intercritical annealing treatment at 770°C as a function of soaking time. The effect of secondary phase constituents on the austenite to martensite transformation kinetics and the underlying mechanisms are presented.

Chapter 8: This chapter presents the summary of the thesis and an overall assessment of the structure-property correlations during each stage of thermomechanical processing of AHSS.

1.7 References:

[1] T. Gladman, Precipitation-hardening of metals., Mater. Sci. Technol. 15 (1999) 205–211. https://doi.org/https://doi.org/10.1179/026708399773002782.

[2] O. Grässel, L. Krüger, G. Frommeyer, L.W. Meyer, High strength Fe-Mn-(Al, Si) TRIP/TWIP steels development - properties - application, Int. J. Plast. 16 (2000) 1391–1409. https://doi.org/10.1016/S0749-6419(00)00015-2.

[3] M.S. Rashid, Dual-phase steels, Automot. Steels Des. Metall. Process. Appl. (1981) 169–216. https://doi.org/10.1016/B978-0-08-100638-2.00007-9.

[4] B. Chongthairungruang, V. Uthaisangsuk, S. Suranuntchai, S. Jirathearanat, Experimental and numerical investigation of springback effect for advanced high strength dual phase steel, Mater. Des. 39 (2012) 318–328. https://doi.org/10.1016/j.matdes.2012.02.055.

[5] R. Kuziak, R. Kawalla, S. Waengler, Advanced high strength steels for automotive industry: A review, Arch. Civ. Mech. Eng. 8 (2008) 103–117. https://doi.org/10.1016/s1644-9665(12)60197-6.

[6] Jose Gerbase-Filho, Mechanical properties of dual phase steels, Mater. Sci. Eng. (1979).

[7] M. Ten Broek, C., Singh, H. & Hillebrecht, LIGHTWEIGHT DESIGN FOR, Autotechreview. 1 (2012) 24–30. https://doi.org/https://doi.org/10.1007/s38311-012-0203-z.

[8] C.C. Tasan, M. Diehl, D. Yan, M. Bechtold, F. Roters, L. Schemmann, C. Zheng, N. Peranio, D. Ponge, M. Koyama, K. Tsuzaki, D. Raabe, An Overview of Dual-Phase Steels: Advances in Microstructure-Oriented Processing and Micromechanically Guided Design,

Annu. Rev. Mater. Res. 45 (2015) 391–431. https://doi.org/10.1146/annurev-matsci-070214-021103.

[9] D.K. Matlock, J.G. Speer, Third Generation of AHSS: Microstructure Design Concepts, Microstruct. Texture Steels. (2009) 185–205. https://doi.org/10.1007/978-1-84882-454-6_11.

[10] J. Cornide, G. Miyamoto, F.G. Caballero, T. Furuhara, M.K. Miller, C. Garcia-Mateo, Distribution of dislocations in nanostructured bainite, Solid State Phenom. 172–174 (2011) 117–122. https://doi.org/10.4028/www.scientific.net/SSP.172-174.117.

[11] R. Grossterlinden, R. Kawalla, U. Lotter, H. Pircher, Formation of pearlitic banded structures in ferritic-pearlitic steels, Steel Res. 63 (1992) 331–336. https://doi.org/10.1002/srin.199200529.

[12] P.I. Kambilinya, C.W. Siyasiya, K.M. Banks, R.J. Mostert, Effect of intercritical annealing of normalised Nb-Ti-V microalloyed plate steel on microstructural evolution, IOP Conf. Ser. Mater. Sci. Eng. 655 (2019). https://doi.org/10.1088/1757-899X/655/1/012004.

[13] E. Erişir, O.G. Bilir, Effect of intercritical annealing temperature on phase transformations in medium carbon dual phase steels, J. Mater. Eng. Perform. 23 (2014) 1055–1061. https://doi.org/10.1007/s11665-013-0848-9.

[14] C. Philippot, J. Drillet, P. Maugis, V. Hebert, M. Dumont, Austenite formation in a ferrite/martensite cold-rolled microstructure during annealing of advanced high-strength steels, Metall. Res. Technol. 111 (2014) 3–8. https://doi.org/10.1051/metal/2014004.

[15] J. Huang, W.J. Poole, M. Militzer, Austenite formation during intercritical annealing, Metall. Mater. Trans. A Phys. Metall. Mater. Sci. 35 A (2004) 3363–3375. https://doi.org/10.1007/s11661-004-0173-x.

Chapter 2 Literature Review

This chapter provides a concise overview of the fundamental micro mechanisms operating during thermomechanical processing, specifically during hot rolling and coiling, as well as cold rolling and annealing, with a primary emphasis on recrystallization and phase transformation pertinent to the thesis. The microstructure evolves during hot rolling and coiling at various temperatures and cooling rates. Subsequently, cold rolling imparts significant deformation that acts as the driving force for recrystallization and transformation. These processes are invariably intertwined.

DP sheet steels can be manufactured through various processing routes. In the traditional approach, these steels are produced via intercritical annealing, wherein the material is heated to the $\alpha + \gamma$ regime. Subsequent to this, a rapid cooling or quenching process ensues, yielding a matrix predominantly composed of soft ferrite interspersed with hard martensite particles[1]. The elevated cooling rate in this approach necessitates reduced quantities of alloying elements[2].

Thermomechanical controlled processing (TMCP) mentioned above, is employed to attain the targeted mechanical properties in the final steel sheet, encompassing a favorable blend of strength, fracture toughness, and weldability [3].

2.1 Hot rolling and coiling:

Hot rolling and coiling are essential processes in the manufacturing of metal products, particularly in the production of steel. These processes are part of thermomechanical processing, which involves shaping the metal at elevated temperatures to improve its mechanical properties and final product characteristics. The integration of hot rolling and coiling plays a vital role in the fabrication of diverse steel items, such as sheets, plates, and coils, enhancing their mechanical attributes and dimensional features. The stored energy resulting from deformation during hot rolling is typically reduced through three mechanisms: recovery, recrystallization, and grain growth [4]. Recovery and recrystallization may occur both during and after deformation, with the former is termed dynamic and the latter termed static to differentiate between them [5]. Many researchers have specifically looked into hot rolling temperature and coiling temperature as detailed here.

2.1.1 Effect of hot rolling temperature:

Compared to conventional micro-alloyed steels, AHSS are multi-phase steels, which usually contain a mix of different microstructural constituents, such as ferrite, martensite, bainite and retained austenite[6]. This microstructure enables high yield and tensile strength[7]. The hot rolling temperature has a significant impact on the development of microstructures and the mechanical properties of these material as reported by Zhuang et. al. [7]. In dual phase steel processing, accurately identifying critical temperatures, including the non-recrystallization temperature (TNR), holds significant importance, especially within the domain of hot rolling processes. Hot rolling, a pivotal manufacturing technique for shaping metals, involves the passage of metal through a sequence of rollers at elevated temperatures. The non-recrystallization temperature (TNR) denotes the threshold temperature beneath which recrystallization does not occur during the hot rolling procedure. Recrystallization is characterized by the replacement of deformed grains in the metal with new, strain-free grains, thereby enhancing mechanical properties. Sub-TNR temperatures induce plastic deformation in the metal without substantial grain rearrangement or recrystallization compared to the ones rolled above TNR. This holds paramount significance in preserving specific mechanical attributes and attaining desired microstructures in the ultimate product. By staying below, the TNR during certain stages of hot rolling, manufacturers can prevent premature recrystallization. This is important when a specific level of strain hardening or specific mechanical properties need to be retained in the final product.

Similar to the DP steels, the microstructure of multiphase TRIP steels is also influenced by finishing rolling temperatures and reduction, resulting in the formation of polygonal ferrite, granular bainite, and a higher quantity of stabilized retained austenite, The enhancement of mechanical properties [8] is observed with a decrease in finishing rolling temperature and an increase in deformation. This phenomenon stabilizes retained austenite, attributed to refined particle size, elevated dislocation density, and increased carbon enrichment. Furthermore, the strain-induced transformation from retained austenite to martensite occurs gradually during tensile testing when the steel undergoes deformation. The below Fig. 2-1 represents the microstructural changes occurring during the hot rolling process. Recovery is characterized by a modest degree of softening compared to recrystallization, which entails the initiation of new, strain-free grains at grain boundaries[9]. Under conditions of elevated temperatures and low strain rates, as encountered in the roughing mill and initial passes of the finishing mill, dynamic recrystallization may occur during the rolling of steels[9].

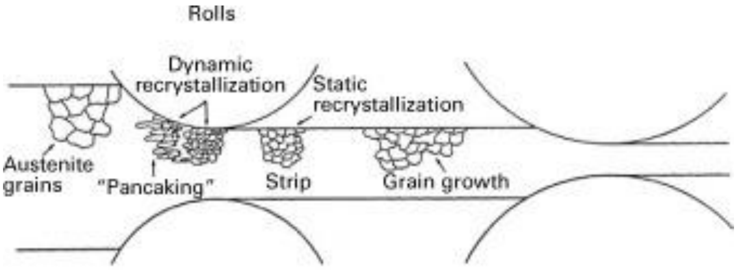

Figure 2-1: Schematic illustration of microstructural alterations taking place during hot rolling[9].

2.1.2 Effect of coiling temperature:

The microstructure and mechanical characteristics of dual phase steels are significantly impacted by the coiling temperature[9]. In low carbon steel at higher coiling temperature, ferrite matrix with the combination of second phase as pearlite is formed, whereas at lower coiling temperature the formation of bainite and martensite takes place[10]. Along with coiling temperature, the cooling rates [11] also have an effect on the microstructure. At low cooling rate coarse grains ate formed, whereas at higher cooling rate grain refinement occurs i.e., fine distribution of second phase in the material. Yang Zhao et. al., [12] reported that coiling at lower temperatures results in a microstructure characterized by elongated ferrite grains. Conversely, coiling at elevated temperatures can induce the formation of polygonal ferrite, leading to reduced yield strength and ultimate tensile strength. As the coiling temperature decreases, the predominant mechanism of strengthening transitions from precipitation strengthening to fine grain strengthening [6]. Exceptional microstructure and mechanical properties stem from the presence of finely polygonal ferrite grains, a high dislocation density, and martensitic laths interspersed within the ferrite grains[10].

2.2 Cold rolling:

Metallic materials are subjected to plastic deformation such as cold rolling, forging, drawing, etc, to produce useful end products. Cold rolling is a deformation process wherein the thickness of metal sheets or strips is reduced by passing then between rollers at temperatures below their recrystallization temperatures. This induces strain hardening and grain refinement, enhancing hardness, surface finish, and the dimensional accuracy of the metal. Cold rolling is essential for the fabrication of flat-rolled steel products such as sheets and coils. Cold rolling is typically conducted at temperatures below approximately 0.3 times the absolute melting point (Tm) of the material. During cold rolling of metallic polycrystalline material, a series of changes take place. These include alterations in the morphology of grains, wherein equiaxed grains evolve into pancake-like structures after cold rolling. The grains also elongate along the rolling direction, increasing the grain boundary area. Within the grains, substructures develop and point defects are created. The substructure evolution is related to the generation and accumulation of dislocations.

2.2.1. Deformation in two-phase alloys

The microstructural constitution of most AHSS alloys employed in industry comprises of at least two phases or constituents: a matrix phase and a dispersed second phase / constituent. The second phase plays a key role in the microstructural evolution during deformation [13], which in turn determines the annealing response. Specifically, the second phase or particles influences the overall dislocation density[14]. This effect holds the potential to amplify the driving force for recrystallization. The particles or second phase influence the deformation process, inducing matrix inhomogeneity. Consequently, this influences the accessibility of recrystallization sites and the character of the deformation structure in the vicinity of the particles[15].

In instances involving substantial second-phase particles during deformation, notable strain inhomogeneities emerge. The presence of large particles hinders dislocation slip, leading to the accumulation of dislocations in their proximity. This accumulation is accompanied by local lattice rotation, typically around the <112> orientation axis, resulting in regions with relatively high dislocation density and significant orientation gradients. These regions are denoted as particle deformation zones (PDZ) and are influenced by factors such as strain, particle size, particle shape, interface strength, and properties of the matrix phase [16].

Owing to numerous experimental challenges, there is a paucity of quantitative data concerning deformation zones in polycrystalline materials [3]. Deformed zones in rolled alloys are frequently observed to extend along the rolling direction. In the proximality of the second-phase particles, small sub-grains with dimensions <0.1 µm are generated. At a slightly greater distance from the particles, sub-grains exhibit distortion and elongation. Utilizing Transmission Electron Microscopy (TEM) and High-Resolution Electron Backscatter Diffraction (HR-EBSD) techniques, the orientation spread (gradient), size, shape, and orientation of deformed zones in rolled polycrystalline materials have been studied [3].

In the cold-rolling process, the original structure's grains, possessing either random or non-random orientations, undergo rotation towards more thermodynamically stable orientations. Specifically, the (223) [110] orientation is recognized as the stable end configuration in the resulting cold-rolled texture [17]. It is observed that, during rolling, grains oriented with the γ fiber orientation rotate more readily than those with α orientations. The susceptibility to reorientation within the rolling texture components correlates with the accumulated stored energy, indicative of inter-granular misorientation. Notably, [17] the inter-granular misorientation is comparatively higher for components associated with the γ fiber than those aligned with the α fiber [18].

2.3 Annealing

Annealing involves the application of heat to a previously cold-deformed material to alter the microstructure. This thermal treatment enables engineers to optimize various material properties. Cold deformation typically results in increased hardness and strength, accompanied by a reduction in ductility. Annealing is undertaken to enhance ductility, albeit at the cost of a reduction in strength and hardness.

During the annealing process, various temperature-induced phenomena occur, traditionally categorized into distinct stages.

i. **Recovery,** which predominantly involves defect rearrangement to lower energy configurations**; Recrystallization**, involves migration of high angle boundaries; and **Grain growth**, involves coarsening of microstructure to much lower energy state. The grain growth process is typically slower than recrystallization because it has a much lower driving force.

ii. **Phase transformation,** involving heating the steel to the two-phase regime to induce phase transformation, typically followed by quenching resulting in a completely different microstructure.

2.3.1 Recrystallization:

Recrystallization is a phenomenon characterized by the migration of high-angle grain boundaries (HAGBs) within a deformed or recovered grain. During this process, strain-free grains form from nuclei generated within the deformed grain. Recrystallization is the sole mechanism through which a completely new grain structure, featuring variations in grain size, shape, orientation, or texture, can be established subsequent to deformation. The outcome of recrystallization includes enhanced ductility and a reduction in strength as compared to the recovery process.

In the context of recrystallization, there are five key aspects that are typically observed, which are summarized here [19].

- Recrystallization initiation requires only a minimal level of deformation at elevated temperatures.
- As the degree of deformation decreases, the necessary recrystallization temperature rises.

- Increasing the soaking times during annealing diminishes the temperature needed for recrystallization.
- The size of recrystallized grains is predominantly influenced by the extent of deformation, wherein smaller grains are a consequence of increased deformation.
- The temperature of recrystallization at a given degree of deformation will be increased by large initial grain size and higher temperature of deformation.

Below are brief descriptions of some of the key factors that influence the rate of recrystallization in materials[20].

Prior deformation: A higher extent of cold deformation corresponds to a heightened density of dislocations, indicating an increase in the stored energy within materials. The higher degree of strain results in greater disparities in stored energy, creating favourable sites for recrystallization. Consequently, this increase in strain level accelerates the rate of recrystallization.

Grain size: A finer grain size provides more stored energy after a small degree of deformation The increase in grain size enhances the inhomogeneous deformation such as shear banding, which provides preferential sites for nucleation. Nucleation is favoured at grain boundaries, where the boundary fraction increases with decreasing grain size.

Texture: The uneven distribution of stored energy aligns with the distinct orientations of texture components. Consequently, the rate of recrystallization varies among different texture components. Deformation texture is also influenced by grain size and determines the recrystallization texture.

Annealing temperature: The rate of recrystallization increases with temperatures, given that it is a thermally activated process. In the recrystallization process, the relationship between time and temperature is typically governed by the Arrhenius relationship [20]. If the rate of recrystallization is employed as a metric, the relationship can be expressed in terms of the time required for 50% recrystallization ($t_{0.5}$).

$$\text{Rate} = 1/t_{0.5} = C \exp(-Q/RT)$$

In the above equation, C is a constant, Q represents the activation energy (in J/mol) for recrystallization, R is the gas constant, and T signifies the temperature in Kelvin. Plotting ln ($t_{0.5}$) against 1/T yields a straight line with a specific slope if a single process drives the recrystallization.

Heating rate: The heating rate is an important variable in annealing. An increase in the heating rate leads to less consumption of stored energy during recovery, consequently leading to a higher rate of recrystallization.

Finally, recrystallization is also hindered by solutes, which reduce the recrystallization rate as their solid solution concentration increases.

Underlying mechanism

The most commonly observed recrystallization mechanisms are briefly discussed here.

Nucleation and growth

The classical nucleation mechanism in recrystallization entails the generation of a defect-free new grain surrounded by High-Angle Grain Boundary (HAGB) within the deformed material[21]. This process is believed to occur in the vicinity of grain boundaries, second-phase particles, and within deformation bands, including shear bands.

Strain-induced boundary migration (SIBM)

SIBM is the second mechanism that develops when the stored energy across the grain boundary differs significantly. Fig. 2-2 shows a schematic of SIBM. With the expansion of single or many sub grains, HAGB bulges out from one grain to the next. As per this mechanism new grains are oriented similar to the old grains from which they bulge. SIBM is observed in low strain conditions in which nucleation sites are less frequent as reported elsewhere[22].

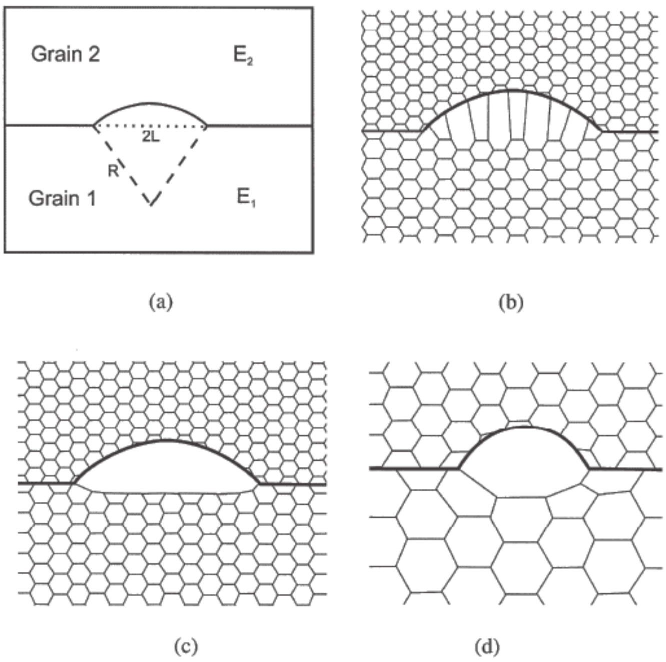

Figure 2-2: SIBM of a boundary dividing a grain with low stored energy (E_1) from one with higher stored energy (E_2), (b) pulling of the dislocation structures behind the migrating boundary [23], (c) migration of boundary free of the dislocation structure, and (d) SIBM beginning at a single big sub grain[20].

Sub grain coalescence

The third mechanism for recrystallization nucleation is proposed in references [24,25]. In this process, during annealing, two neighbouring sub-grains undergo rotation. The sub-grain boundary between these two grains is eliminated as their orientations converge. The iterative coalescence process leads to the formation of a High-Angle Grain Boundary (HAGB) and, consequently, the initiation of recrystallization.

The initial two mechanisms of recrystallization share a similarity in that both are triggered by boundary migration. Numerous studies indicate that, in the case of iron, the most prevalent method for generating new, strain-free grains involves the mobility of pre-existing grain boundaries [26].

2.3.1.1 Impact of second phase on recrystallization:

The interaction of recrystallization with second-phase particles results in alterations to the microstructure in one of two ways, as elucidated by reference [20]. The following points delineate the notable influences on recrystallization with second-phase particles.

- It is feasible to elevate the stored energy, thereby augmenting the driving force for recrystallization.
- Large particles can serve as sites for recrystallization nucleation.
- Closely positioned particles are subject to the pinning effect on both Low-Angle Grain Boundaries (LAGB) and High-Angle Grain Boundaries (HAGB).

Recrystallization is promoted by the first two effects, while the third tends to impede it. Consequently, the kinetics of recrystallization, as well as the resulting grain size and texture, are determined by the predominant influence among these effects. The distribution, size, and volume fraction of second-phase particles are dictated by the alloy composition and processing. By manipulating these factors, the microstructure and texture can be controlled during recrystallization.

When the material-containing particles undergo distortion, a particle with a significant diameter can generate a heightened local concentration of stored energy and substantial misorientation in the adjacent microstructure, thus serving as a favourable nucleation site [27,28]. These high-energy zones typically extend to a distance of approximately one diameter from the particle surface, indicating that the size of these zones is dictated by the particle’s dimensions. Consequently, if the strained region surpasses the critical nucleus size, nuclei can form within these strained zones and promptly initiate growth owing to the misorientation of the surrounding microstructure.

In the case of finely dispersed particles ($d < 0.1$ µm), the nucleation process experiences a delay due to Zener drag. Fine particles act as inhibitors to both dislocation movement and grain boundary motion [29,30].

2.3.1.2 Recrystallization in low carbon steels

Cementite is the second phase in ferritic low carbon steels. Hutchinson et al. [31] showed that annealing causes carbon to migrate from cementite to ferrite, creating a competition between carbide dissolution and recrystallization nucleation (see Fig. 2-3). They reported that recrystallization is more favoured than cementite dissolution at high temperatures, especially for fast heating rates, depending on the inter-particle spacing.

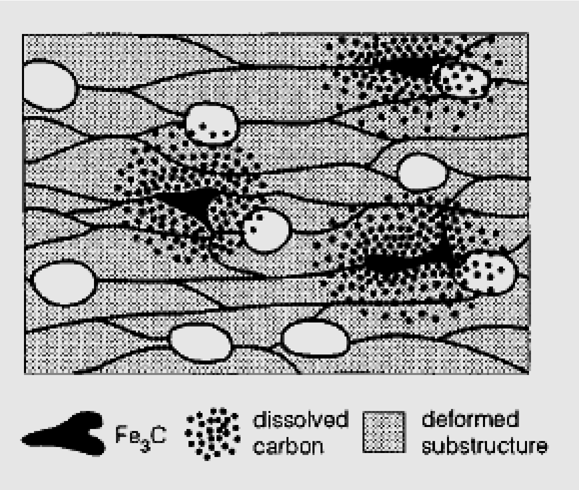

Figure 2-3: Schematic microstructure showing a concurrent process of cementite dissolution and recrystallization [31].

Hutchinson et al. [31] varied the inter-particle spacing and computed the dissolved carbon content as a function of the heating rate, as depicted in Fig. 2-4. The results in Fig. 2-4 distinctly demonstrate that in the case of finely spaced particles (λ = 20 μm), the average dissolved content in the matrix is 50 ppm, while coarse carbide spacing (λ = 80 μm) results in less than 10 ppm under rapid annealing conditions.

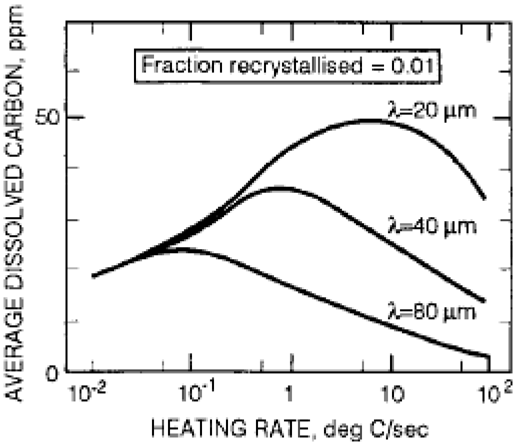

Figure 2-4: Dissolved carbon content as a function of heating rate and dispersion of cementite particle with varying particle spacing (λ) [31].

2.3.2 Phase Transformation:

2.3.2.1 Formation of dual phase microstructure

DP sheet steels are typically obtained by intercritical annealing treatment utilizing the continuous annealing procedures [29]. In an uninterrupted annealing process, the steel sheet, characterized by a ferrite-and second phase such as pearlite/bainite/martensite microstructure, undergoes a brief exposure to the intercritical temperature range, leading to the formation of ferrite-austenite mixture. Subsequent rapid cooling induces the transformation of the austenite phase into martensite.

2.3.2.2 Formation of austenite during intercritical annealing

Fig. 2-5 shows a part of the iron-carbide phase diagram with the two phase (α+γ) region for intercritical annealing at a given carbon content [32].

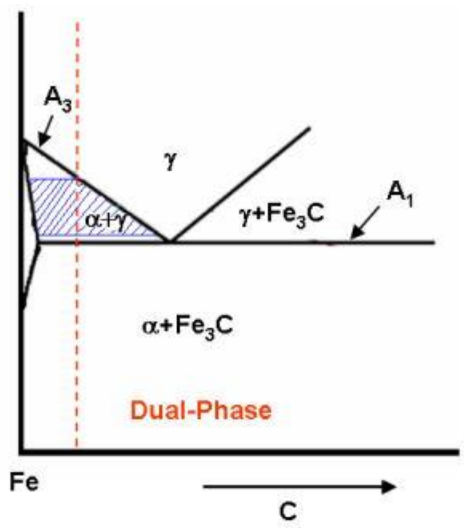

Figure 2-5: Simplified Iron-Carbon diagram that illustrates the annealing temperature is associated with a specified composition of the steel [32].

Based on the lever rule, at a constant carbon concentration, the fraction of austenite increases with increasing intercritical temperature, until it becomes the sole phase at the A3 temperature. Similarly, when subjected to a constant intercritical temperature, the proportion of austenite experiences a gradual rise as the carbon concentration increases, reaching a point where it becomes the dominant phase at a carbon concentration that aligns perfectly with the boundary between γ and γ+α phases [32].The process of austenite formation from a ferrite-pearlite microstructure close to commonly used DP600 grade during intercritical annealing can be delineated into multiple stages[33].

- The nucleation of austenite at pearlite particles happens instantly, and then the material grows quickly until the carbide phase dissolves [32].
- Austenite gradually expands into ferrite, with the rate of development determined by the diffusion of the carbon in austenite at 850°C and the diffusion of the manganese in austenite at 750°C temperature [32].

The ultimate equilibration between ferrite and austenite occurs at an extremely slow pace, regulated by the diffusion of manganese in austenite.

The initial stage involves the dissolution of pearlite and the expansion of austenite into the pearlite structure. This advancement is mainly controlled by the distribution of carbon within the austenite. The preferred path of carbon mobility is the boundary between pearlite and austenite, with the extent of mobility roughly matching the spacing between pearlite lamellae [32].

At the end of the first phase, a high-C austenite is formed, exhibiting a non-equilibrium state with ferrite. The subsequent progression involves the gradual transformation of this austenite into ferrite, aiming to attain partial stability with the ferrite, marking the second phase [32]. The decelerated expansion of austenite during this stage can be regulated either by carbon distribution within the austenite or by manganese distribution within ferrite matrix [32].

In the third step, an exceedingly slow attainment of the ultimate equilibrium between ferrite and austenite occurs, facilitated by manganese diffusion through the austenite [32]. It is noteworthy that the diffusion rate of manganese in austenite is three orders of magnitude slower compared to its diffusion in ferrite[33].

The rate of formation of austenite during intercritical annealing depends on the ferrite grain-size. The initial rapid formation of austenite is attributed to high density of nucleation sites at the FP boundaries [32]. In addition, the smaller the grain size of ferrite, the easier it is for replacing solutes, such as Mn, to get distributed within the ferrite throughout the subsequent growth of the austenite[34].

2.3.2.3 Phase transformation during intercritical annealing

While the transformation of austenite in DP steel following intercritical annealing shares similarities with the growth of austenite following the conventional austenitizing, two characteristics render this transformation process distinct[32]:

The intercritical temperature serves as the primary determinant of the carbon content in austenite, thereby resulting variation in the hardness of the austenite across varying intercritical temperatures [32]. Specifically, at lower temperature characterized by higher carbon content in austenite, the hardenability of the phase is proportionately high. Conversely, at higher temperatures resulting in reduced carbon content in austenite, the hardenability of the austenite diminishes. Also, due to the pre-existing presence of ferrite, the transformation from γ to α can advance through the epitaxial growth of the existing ferrite into austenite without necessitating a nucleation step[22,33].

A diverse spectrum of morphologies and evolution products do arise from the austenite subsequent to intercritical heat treatment, contingent upon factors such as heat treatment duration, and cooling rate [32]. In dual-phase steel, the hardness of austenite is mostly dependent on the added fusing elements[22,33].

The formation of martensite from the austenite at lower temperature and the ferrite phase allow the plastic deformation in it has more tendency to nuclei first and then it transforms in to austenite, the transforming austenite then subsequently transfer to martensite [32]. As a result, this procedure generates a substantial dislocation density and imparts residual stresses within the ferrite in close proximity to martensite particle. Even though the residual stresses are too small to be directly measured, theoretical analysis indicates that their maximum magnitude would be roughly on the order of the yield strength of the ferrite (at the Ms temperature), gradually decreasing exponentially as one moves away from the interface between martensite and ferrite[32][22,33].

2.3.2.4 Transformation of ferrite during sub-critical heat treatment and cooling

During intercritical heat treatment, if the heating rate applied to the cold-rolled steel sheets exceeds a certain threshold, the characteristics of the ferrite can undergo changes. When recrystallization occurs, various characteristics of ferrite have been observed, including full recrystallization and partial recrystallization. Austenite nucleation commences at the fully recrystallized ferrite grains, where grain growth takes place. These recrystallized grains are influenced by the presence of the austenite phase at the grain boundaries. [32].

Alterations in the carbon percentage of the ferrite can take place during sub-critical annealing as detailed below [32].

- The dispersion of carbon in the ferrite phase could be reduced at the sub-critical temperature compared to its original concentration in the as-received material's ferrite phase. This reduction in carbon solubility within the ferrite is associated with the escalation of the intercritical temperature, and it may also be significantly influenced by an elevation in the overall alloy percentage of the steel [32].

- Deviations in the cooling rate from the sub-critical temperature can impact the carbon composition of the ferrite matrix [32]. A decrease in the cooling rate may lead to the precipitation of cementite within the ferrite, leading to a reduction in the carbon content of the ferrite [22].

In the majority of intercritically annealed DP steels, two distinct forms of ferrite can be discerned: "retained ferrite," which exists at the intercritical annealing temperature [32], and "epitaxial ferrite," which develops from austenite during the cooling phase as shown in Fig. 2-6. Research has demonstrated the absence of a structural interface between these two ferrite types, establishing that epitaxial ferrite extends from the retained ferrite grains [22].

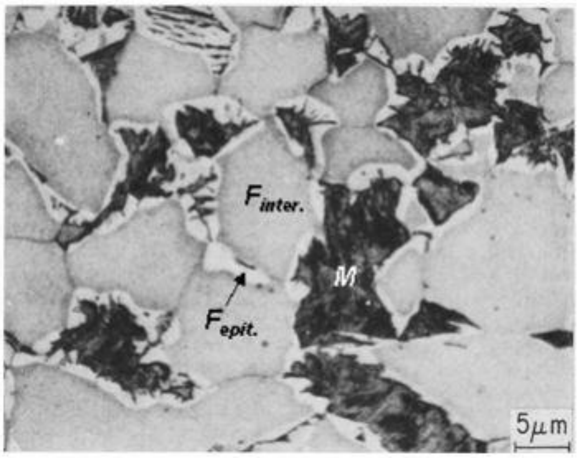

Figure 2-6: Ferrite variants in a DP steel can be categorized as follows: Gray denotes retained ferrite, white represents epitaxial ferrite, and black indicates martensite[22].

2.4 A critical review of literature:

Thermomechanical processing of advanced high strength steels mainly involves hot rolling, coiling, cold rolling and intercritical annealing. The different processing steps and process parameters accordingly affect the microstructure and mechanical properties. The important process parameters that determine the initial microstructure are hot rolling temperature and coiling temperature after the hot rolling [12,35,36]. The steel's chemical composition and the cooling rate [32] from the hot rolling regime also affect the microstructures [6,10,37]. Subsequent to hot rolling and coiling, the samples are cold rolled to enhances the strength and also to obtain the desired crystallographic texture [38–40] [41,42]. The next processing step is recovery / recrystallization annealing and intercritical annealing. The microstructural evolution during the recrystallization of dual phase steel has been previously reported[43], along with the interaction between recovery, recrystallization and transformation [44]. Intercritical annealing of cold rolled DP microstructures has been reported by Karmakar et al. [45] and Mazaheri et al. [46]. Most of the previously reported works have studied the effect of processing parameters such as coiling temperature, extent of cold rolling and annealing temperature with different chemical compositions and constituent phases. However, the effect of these process parameters on microstructure and local mechanical properties during all the processing steps at a given chemical composition has not been reported. Furthermore, given the dual or multi-phase nature of most AHSS, in addition to macro scale testing, it is important to study the mechanical properties at the length scale of the individual constituents, which has not been systematically studied as well.

Most AHSS are dual or multi-phase steels and there is a continuous ongoing effort globally to modify the processing to obtain the desired microstructure and thereby the properties. Establishing the relationship between the processing, microstructural and mechanical characteristics at the length scale of distinct constituents of these AHSS is the key to developing AHSS with the desired combination of mechanical properties. In this regard, closely coupling the microstructure with the mechanical properties at the micrometer length scale is critically required. Hence, a comprehensive study of the microstructure and local mechanical properties of dual phase steels during various processing steps such as hot rolling, coiling, cold rolling and annealing is carried out to establish the much-needed relationship between processing, microstructure and property at the micrometer length scale.

2.5 References:

[1] J. Huang, W.J. Poole, M. Militzer, Austenite formation during intercritical annealing, Metall. Mater. Trans. A Phys. Metall. Mater. Sci. 35 A (2004) 3363–3375.

https://doi.org/10.1007/s11661-004-0173-x.

[2] T. Heller, A. Nuss, Effect of alloying elements on microstructure and mechanical properties of hot rolled multiphase steels, Ironmak. Steelmak. 32 (2005) 303–308. https://doi.org/10.1179/174328105X47981.

[3] A.J. DeArdo, Physical Metallurgy of the Thermomechanical Processing of Microalloyed Steels, THERMEC 97 Int. Conf. Thermomechanical Process. Steels Other Mater. (1997) 13–29.

[4] J.R. Bradley, J.M. Rigsbee, H.I. Aaronson, Growth kinetics of grain boundary ferrite allotriomorphs in Fe-C alloys, Metall. Trans. A. 8 (1977) 323–333. https://doi.org/10.1007/BF02661647.

[5] M. Asadi, H. Palkowski, Influence of the hot rolling process on the mechanical behaviour of martensitic steel, 2012. https://doi.org/10.4028/www.scientific.net/AMR.409.653.

[6] J. Xue, Z. Zhao, C. Bin, X. Liu, H. Wu, H. Li, W. Xiong, Effects of rolling and coiling temperature on the microstructure and mechanical properties of hot-rolled high strength complex phase steel, Mater. Res. Express. 6 (2019). https://doi.org/10.1088/2053-1591/ab1404.

[7] Z. Li, D. Wu, Effects of finishing rolling temperatures and reduction on the mechanical properties of hot rolled multiphase steel, J. Zhejiang Univ. Sci. A. 8 (2007) 797–804. https://doi.org/10.1631/jzus.2007.A0797.

[8] M.D. and D.B. Subhankar Das BAKSHI, Effect of Finish Hot Rolling Temperature on the Surface Quality of Galvannealed IF-HS Steel Sheets, ISIJ Int. 45 (2005) 1368–1370.

[9] Anon, Hot Rolling., Nippon Steel Tech. Rep. (1983) 101–107. https://doi.org/10.2464/jilm.51.253.

[10] G.L. Wu, X.B. Liu, C.Y. Zhou, Effects of rolling and cooling process on mechanical properties and microstructure of 600 MPa microalloyed dual-phase steel produced by compact

strip production, J. South. African Inst. Min. Metall. 116 (2016) 49–53. https://doi.org/10.17159/2411-9717/2016/v116n1a8.

[11] T. Lolla, G. Cola, B. Narayanan, B. Alexandrov, S.S. Babu, Development of rapid heating and cooling (flash processing) process to produce advanced high strength steel microstructures, Mater. Sci. Technol. 27 (2011) 863–875. https://doi.org/10.1179/174328409X433813.

[12] Y. Zhao, X. Huang, B. Yu, X. Yuan, X. Liu, Effect of coiling temperature on microstructure, properties and resistance to fish-scaling of hot rolled enamel steel, Materials (Basel). 10 (2017). https://doi.org/10.3390/ma10091012.

[13] J. Singh, M.S. Kim, J.H. Lee, H. Guim, S.H. Choi, Microstructure evolution and deformation behaviors of E-form and AZ31 Mg alloys during ex-situ mini-V-bending tests, J. Alloys Compd. 778 (2019) 124–133. https://doi.org/10.1016/j.jallcom.2018.11.138.

[14] R.B. CALHOUN, D.C. DUNAND, Dislocations in Metal Matrix Composites, Compr. Compos. Mater. (2000) 27–59. https://doi.org/10.1016/b0-08-042993-9/00002-4.

[15] K.K. Alaneme, E.A. Okotete, Recrystallization mechanisms and microstructure development in emerging metallic materials: A review, J. Sci. Adv. Mater. Devices. 4 (2019) 19–33. https://doi.org/10.1016/j.jsamd.2018.12.007.

[16] N. Bloom, J. Van Reenen, FUNDAMENTAL ASPECTS OF DISLOCATION THEORY, NBER Work. Pap. (2013) 89. http://www.nber.org/papers/w16019.

[17] J.F. Nie, K.S. Shin, Z.R. Zeng, Microstructure, Deformation, and Property of Wrought Magnesium Alloys, Springer US, 2020. https://doi.org/10.1007/s11661-020-05974-z.

[18] J.-Y. Kang, D.-I. Kim, H.-C. Lee, Texture Development in Low Carbon Sheet Steels for Automotive Application, Microstruct. Texture Steels. (2009) 85–101. https://doi.org/10.1007/978-1-84882-454-6_5.

[19] J.E. Burke, D. Turnbull, Recrystallization and grain growth, Prog. Met. Phys. 3 (1952). https://doi.org/10.1016/0502-8205(52)90009-9.

[20] F.J. Humphreys, M. Hatherly, Recrystallization and Related Annealing Phenomena, Recryst. Relat. Annealing Phenom. (2012) 1–497. https://doi.org/10.1016/C2009-0-07986-0.

[21] F.J. Humphreys, Nucleation in recrystallization, Mater. Sci. Forum. 467–470 (2004) 107–116. https://doi.org/10.4028/www.scientific.net/msf.467-470.107.

[22] G.. Speich, Physical Metallurgy of Dual-Phase Steels. Fundemental of Dual-Phase steels, 26 (1981) 3–45.

[23] A. Laura, C. Fabiano, Modelling of crystal plasticity and grain boundary migration of 304L steel at the mesoscopic scale École doctorale n ° 364 : Sciences Fondamentales et Appliquées l ’ École nationale supérieure des mines de Paris, (2014).

[24] J.C.M. Li, Possibility of subgrain rotation during recrystallization, J. Appl. Phys. 33 (1962) 2958–2965. https://doi.org/10.1063/1.1728543.

[25] P.R. Rios, F. Siciliano, H.R.Z. Sandim, R.L. Plaut, A.F. Padilha, Nucleation and growth during recrystallization, Mater. Res. 8 (2005) 225–238. https://doi.org/10.1590/S1516-14392005000300002.

[26] W.C. Leslie, The quench-ageing of low-carbon iron and iron-manganese alloys an electron transmission study, Acta Metall. 9 (1961) 1004–1022. https://doi.org/10.1016/0001-6160(61)90244-9.

[27] F.J. Humphreys, The nucleation of recrystallization at second phase particles in deformed aluminium, Acta Metall. 25 (1977) 1323–1344. https://doi.org/10.1016/0001-6160(77)90109-2.

[28] M.A. Almojil, DEFORMATION AND RECRYSTALLISATION IN LOW CARBON STEELS, (2010).

[29] E. Nes, N. Ryum, O. Hunderi, On the Zener, Acta Mater. 33 (1985) 11–22.

[30] G.S. Rohrer, “introduction to grains, phases, and interfaces-an interpretation of

microstructure," Trans. AIME, 1948, vol. 175, pp. 15-51, by C.S. Smith, 2010. https://doi.org/10.1007/s11661-010-0215-5.

[31] B. Hutchinson, Practical aspects of texture control in low carbon steels, Mater. Sci. Forum. 157–6 (1994) 1917–1928. https://doi.org/10.4028/www.scientific.net/msf.157-162.1917.

[32] I. Pushkareva, Microstructural evolution of Dual Phase steel . Improvement of damage resistance To cite this version : HAL Id : tel-01748776 soutenance et mis à disposition de l ' ensemble de la Contact : ddoc-theses-contact@univ-lorraine.fr, (2018).

[33] G.R. Speich, V.A. Demarest, R.L. Miller, Formation of Austenite During Intercritical Annealing of Dual-Phase Steels., Metall. Trans. A, Phys. Metall. Mater. Sci. 12 A (1981) 1419–1428. https://doi.org/10.1007/bf02643686.

[34] I.A. El-Sesy, H.J. Klaar, A.H.A. Hussein, Effect of intercritical temperature and cold-deformation on the kinetics of austenite formation during the intercritical annealing of dual-phase steels, Steel Res. 61 (1990) 131–135. https://doi.org/10.1002/srin.199000317.

[35] S.J. Kim, C.G. Lee, T.H. Lee, S. Lee, Effects of coiling temperature on microstructure and mechanical properties of high-strength hot-rolled steel plates containing Cu, Cr and Ni, ISIJ Int. 40 (2000) 692–698. https://doi.org/10.2355/isijinternational.40.692.

[36] V.S.A. Challa, R.D.K. Misra, R. O'Malley, S.G. Jansto, The effect of coiling temperature on the mechanical properties of ultrahigh-strength 700 MPa grade processed via thin-slab casting, AISTech - Iron Steel Technol. Conf. Proc. 3 (2014) 2987–2997.

[37] S. Keeler, M. Kimchi, P.J. Mooney, Advanced High-Strength Steels Guidelines Version 6.0, WorldAutoSteel. (2017) 314. https://www.worldautosteel.org/projects/advanced-high-strength-steel-application-guidelines/.

[38] E. Bassini, G. Marchese, A. Sivo, P.A. Martelli, A. Gullino, D. Ugues, Effect of Cold Rolling on Microstructural and Mechanical Properties of a Dual-Phase Steel for Automotive Field, Materials (Basel). 15 (2022). https://doi.org/10.3390/ma15217482.

[39] N. Deeparekha, A. Gupta, M. Demiral, R.K. Khatirkar, Cold rolling of an interstitial free (IF) steel—Experiments and simulations, Elsevier Ltd, 2020. https://doi.org/10.1016/j.mechmat.2020.103420.

[40] Y. Zhang, Q. Yuan, J. Ye, X. Weng, Z. Wang, Effect of cold rolling reduction on microstructure, mechanical properties, and texture of deep drawing dual-phase (DP) steel, Mater. Res. Express. 6 (2019). https://doi.org/10.1088/2053-1591/ab2d71.

[41] Z. Wang, Y. Dong, J. Li, F. Chai, L. Wang, Q. Liu, B. Fu, M. Liu, Z. Wang, The Role of Cold Rolling Reduction on the Microstructure and Mechanical Properties of Ultra-Low Carbon Bainitic Steel, Materials (Basel). 15 (2022). https://doi.org/10.3390/ma15093070.

[42] R. Ueji, N. Tsuji, Y. Minamino, Y. Koizumi, Effect of rolling reduction on ultrafine grained structure and mechanical properties of low-carbon steel thermomechanically processed from martensite starting structure, Sci. Technol. Adv. Mater. 5 (2004) 153–162. https://doi.org/10.1016/j.stam.2003.10.017.

[43] N. Peranio, F. Roters, D. Raabe, Microstructure evolution during recrystallization in dual-phase steels, Mater. Sci. Forum. 715–716 (2012) 13–22. https://doi.org/10.4028/www.scientific.net/MSF.715-716.13.

[44] B. Bandi, J. Van Krevel, P. Srirangam, Interaction Between Ferrite Recrystallization and Austenite Formation in Dual-Phase Steel Manufacture, Metall. Mater. Trans. A Phys. Metall. Mater. Sci. 53 (2022) 1379–1393. https://doi.org/10.1007/s11661-022-06597-2.

[45] A. Karmakar, M. Ghosh, D. Chakrabarti, Cold-rolling and inter-critical annealing of low-carbon steel: Effect of initial microstructure and heating-rate, Mater. Sci. Eng. A. 564 (2013) 389–399. https://doi.org/10.1016/j.msea.2012.11.109.

[46] Y. Mazaheri, A. Kermanpur, A. Najafizadeh, Microstructures, Mechanical Properties, and Strain Hardening Behavior of an Ultrahigh Strength Dual Phase Steel Developed by Intercritical Annealing of Cold-Rolled Ferrite/Martensite, Metall. Mater. Trans. A Phys.

Metall. Mater. Sci. 46 (2015) 3052–3062. https://doi.org/10.1007/s11661-015-2918-0.

Chapter 3 Experimental Procedure

This chapter presents the details of the materials and experimental methods that includes the chemical composition, thermomechanical processes steps, the methods used to characterize the microstructures, and mechanical properties. Additionally, this chapter describes in detail a novel methodology that combines EBSD and nanoindentation mapping data to deconvolute the mechanical properties of the individual phases to enable assessment of the structure-property relationships at the micrometer length scale.

3.1 Materials and their chemical composition

In the present study, steel sheet with low C-Mn content was investigated with a composition close to commercial grade of DP 600 and is shown in Table 1. The steel sheets were received from TATA STEEL Europe Ijmuiden, the Netherlands.

Table 1: Nominal chemical composition of the steel sheet

Element	C	Mn	Si	Nb	Cr
wt. %	0.09	1.65	0.28	< 0.001	0.057

3.2 Thermomechanical processing

The thermomechanical processing carried out in this work is schematically shown in Fig. 3-1. A 37mm cast ingot undergoes a one-hour soak at 1200 °C, followed by hot rolling above the austenite recrystallization temperature (Tnr). The Tnr temperatures for these steel sheets were established by Gautam et al [1]. In the hot rolling process, the initial 37mm primary rolled industrial block undergoes six passes, progressively reducing to a 6mm sheet. Fig. 3-1 illustrates the percentage of rolling reduction in each pass. Subsequently, they were cooled at varying cooling rates of 5, 20 and 80°C/s, followed by coiling at 600 (Ps), 450 (Bs) and

250°C (Ms) respectively for 6 h followed by air cooling to room temperature, to obtain ferrite-pearlite, ferrite-bainite and ferrite-martensite microstructures. Following hot rolling and coiling, the samples undergo additional cold rolling, achieving reductions of 60% and 80%, resulting in a thickness reduction from 6 mm to 1.2 mm, as depicted in Fig. 3-1. Subsequently, these samples undergo annealing separately at recrystallization temperatures of 725ºC and intercritical annealing temperatures of 770ºC. Microstructural changes during these processing conditions are examined using scanning electron microscopy (SEM) and electron backscatter diffraction (EBSD). The mechanical properties were measured using a Vickers microhardness testing and nanoindentation. A detailed description of these methods is provided in the subsequent sections.

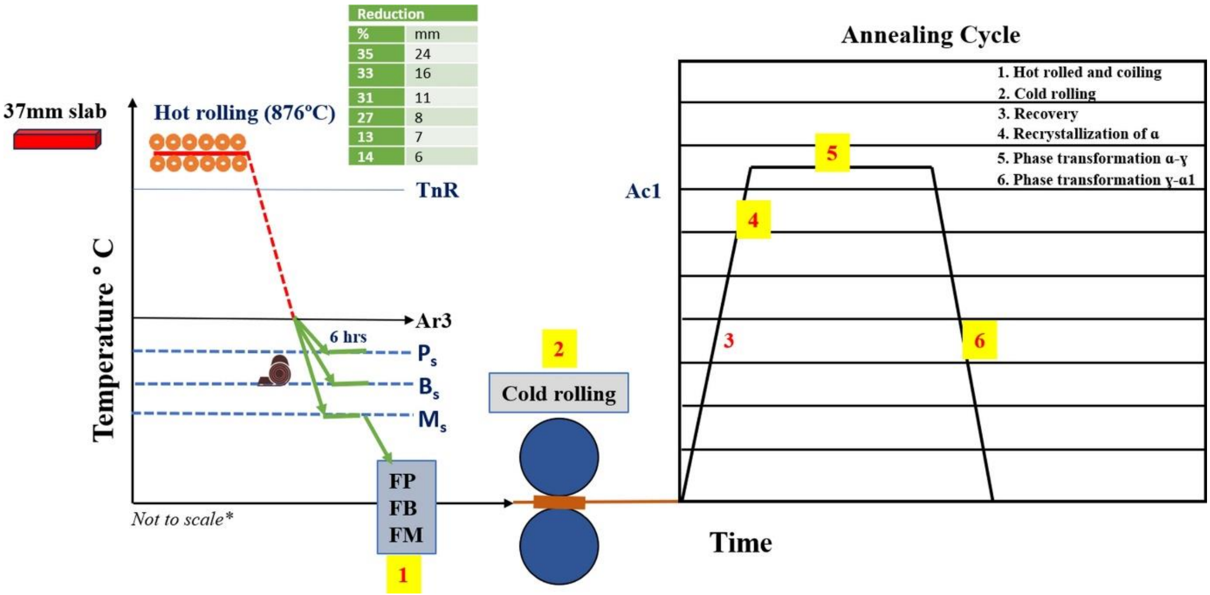

Figure 3-1: Schematic representation of thermomechanical processing of AHSS. (FP-ferrite-pearlite, FB-Ferrite-bainite, FM- Ferrite-martensite).

3.3 Annealing

Before the annealing treatment the hot rolled and coiled samples and cold rolled 60 and 80% samples are microstructurally and mechanically characterized. Annealing treatment was carried out to investigate the recrystallization and phase transformation behavior of all the 80% cold-rolled samples. Small rectangular specimens measuring 1.2x1 cm (LxW) were obtained from the middle portion of the cold-rolled sheets with a thickness of 1.2mm.

3.3.1 Recrystallization

Recrystallization annealing was conducted using a salt bath furnace, at a temperature of 725ºC with a rapid heating rate of 185ºC/s. Samples were drawn at different soaking times, including 10s, 30s, 60s, 180s, 300s, 600s, and 900s, followed by immediate quenching in water. A schematic representation of the recrystallization cycle is presented in Fig. 3-2.

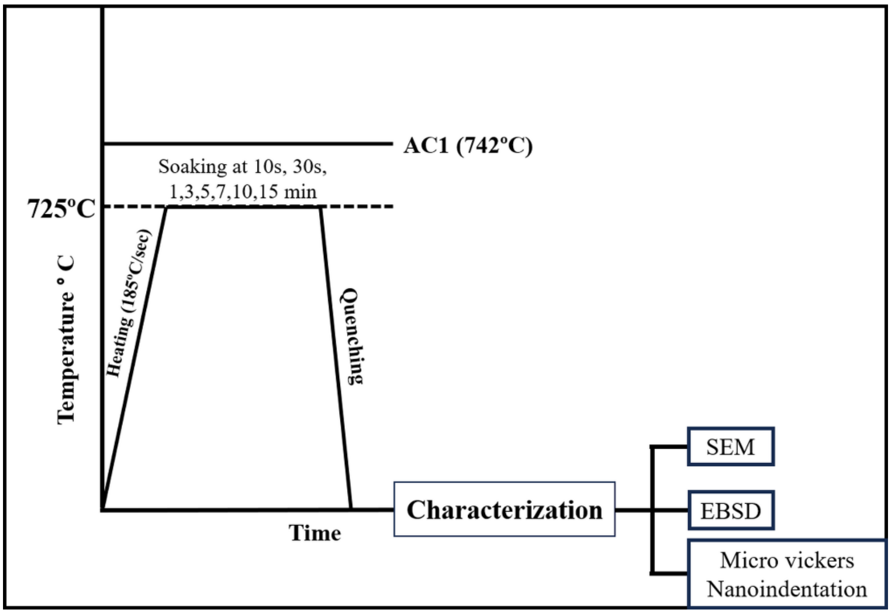

Figure 3-2: Schematic of recrystallization annealing procedure.

3.3.2 Phase transformation

Intercritical annealing was conducted using a salt bath furnace, maintaining a temperature of 770ºC with a rapid heating rate of 185ºC/s. Samples were drawn at different soaking times, including 60s, 180s, 300s, 420s, 600s, and 900s, followed immediate quenching in water. Fig. 3-3 provides a schematic illustration of the experimental intercritical annealing cycle.

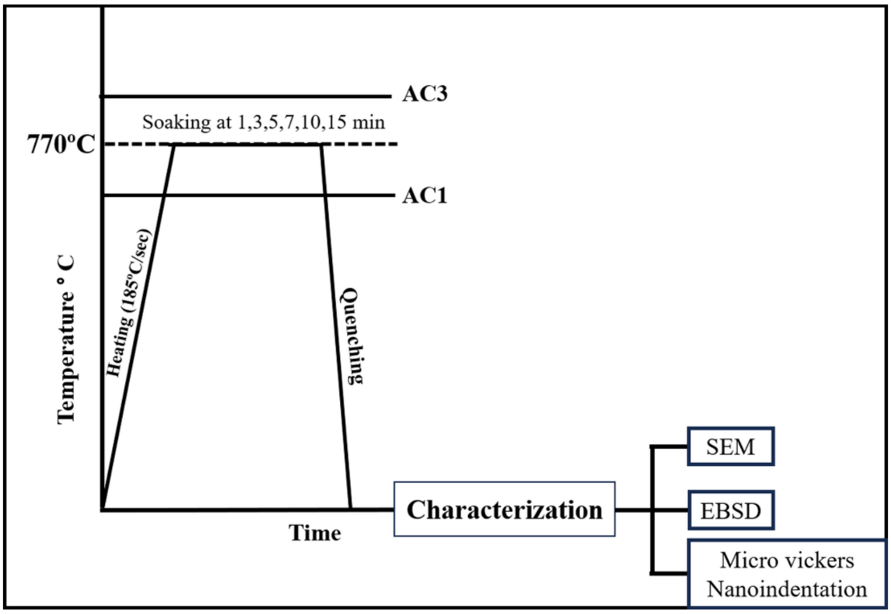

Figure 3-3: Schematic of intercritical annealing procedure.

3.4 Sample preparation

The preparation of samples, including hot-rolled, cold-rolled, and annealed specimens, is crucial for accurate data measurement and analysis using various characterization techniques. The samples must exhibit flatness, be devoid of debris, and remain free from strain induced by mechanical polishing to ensure accurate microstructure and property measurements. As part of the sample preparation process, mechanical polishing was carried out using SiC papers of varying grits (800, 1000, 1200, 1500, 2000, 2500), followed by progressively polishing with alumina suspension of 1µm, 0.3µm, 0.1µm and 0.05µm. Vibratory polishing was then performed using fine colloidal silica suspension (40 nm) for an 8-hour duration.

Micro-vickers hardness and nanoindentation hardness measurements were subsequently carried out on these meticulously polished specimens [2]. In this study, hardness, microstructural, and texture measurements were conducted on the cross-section in the RD-ND direction as shown in Fig. 3-4.

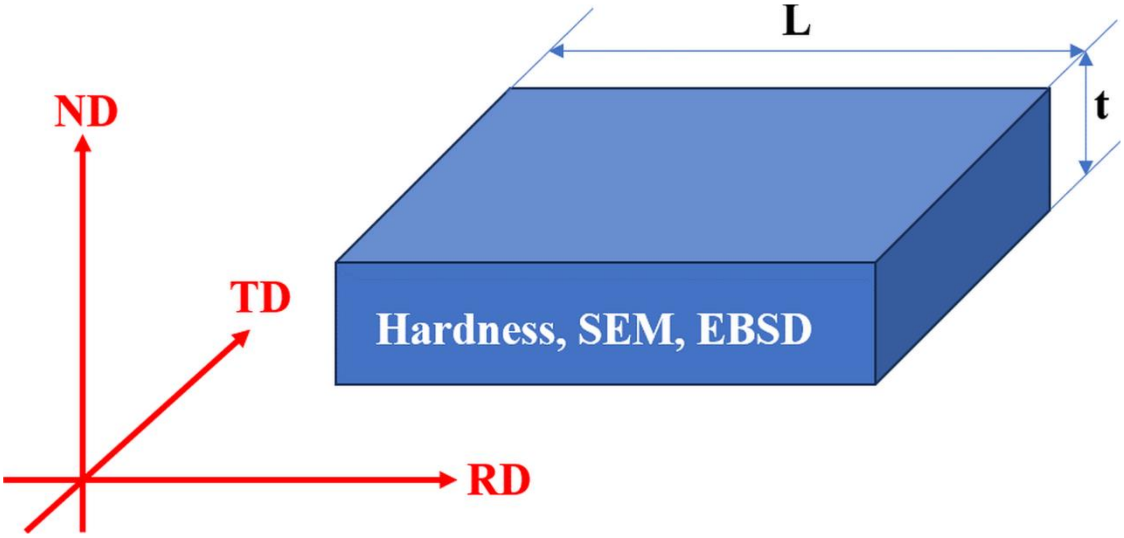

Figure 3-4: Schematic showing cross-section used for measurement by different characterization techniques.

3.4.1 EBSD sample preparation:

The sample preparation for EBSD analysis is similar to the procedure described earlier, which involves initial polishing with SiC polishing paper followed by alumina suspension and vibratory polishing with 40 nm colloidal silica suspension.

3.5 Microstructural characterization:

3.5.1 Optical and Scanning electron microscopy:

Microstructural examination following hot rolling was conducted using an optical microscope (OM), while cold rolling and annealing microstructures were observed utilizing a field emission scanning electron microscope (FE-SEM). All specimens were etched with 2% Nital for microstructural analysis using OM and FE-SEM. The optical microscope employed in this study was an Olympus model equipped with a digital camera.

3.5.2 Area fraction measurement:

The phase fractions of ferrite, pearlite, bainite and martensite were obtained by image analysis using Image J software [3]. Fig. 3-5(a) shows the optical micrographs of the samples, where ferrite appears as white and the other phases as grey. Fig. 3-5(b) shows the binary images obtained by applying a threshold to the contrast/brightness of the original image, where the different phases are highlighted by different colours. The phase fractions were calculated by averaging the results from 8-10 images taken from different locations of the samples.

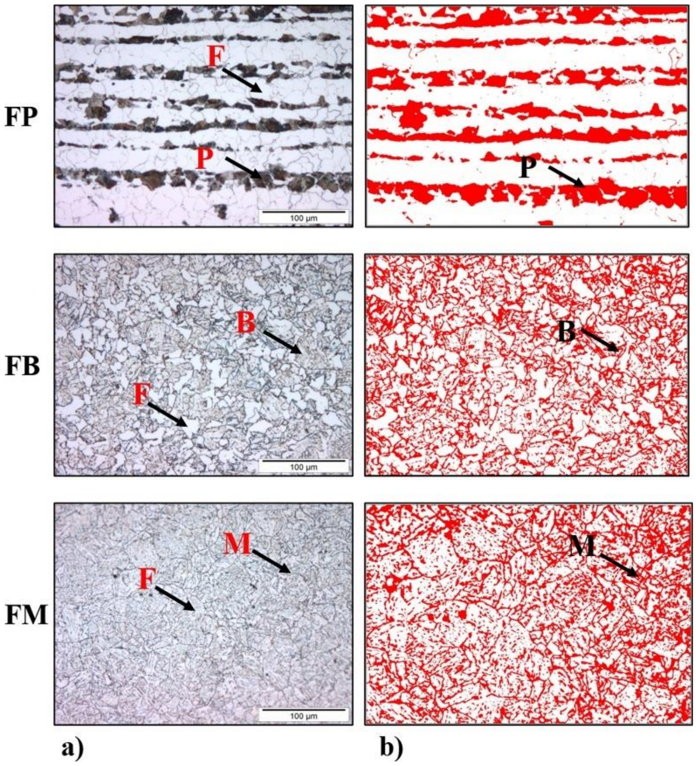

Figure 3-5: Optical micrographs of (a) ferrite-pearlite (FP), ferrite-bainite (FB) and ferrite-martensite (FM) (b) monochrome bitmap of pearlite, bainite and martensite.

The surface morphology and microstructure of the samples were examined by field emission scanning electron microscopy (FE-SEM). The microstructural investigations were performed using field emission scanning electron microscope (FESEM Model: FEI - NOVA NANOSEM 450) at an accelerating voltage of 20 kV and a working distance of 15 mm[4]. The microstructural evolution due to hot rolling and coiling, cold rolling, recrystallization and intercritical annealing on the ferrite and the other phases were analysed by FE-SEM.

3.5.3 Electron backscattered diffraction:

EBSD, a technique for characterizing materials using a scanning electron microscope (SEM), involves scanning the electron beam across the surface of a tilted crystalline sample. The diffracted electrons at each point create patterns that are detected and analysed using specialized hardware and software [5]. Through the indexing process at each point, valuable information about the phase and crystallographic orientation is obtained, allowing for the effective reconstruction of the microstructure. This comprehensive approach enables a thorough characterization of the microstructural properties of the sample. Figure 3-6 shows a schematic of EBSD setup.

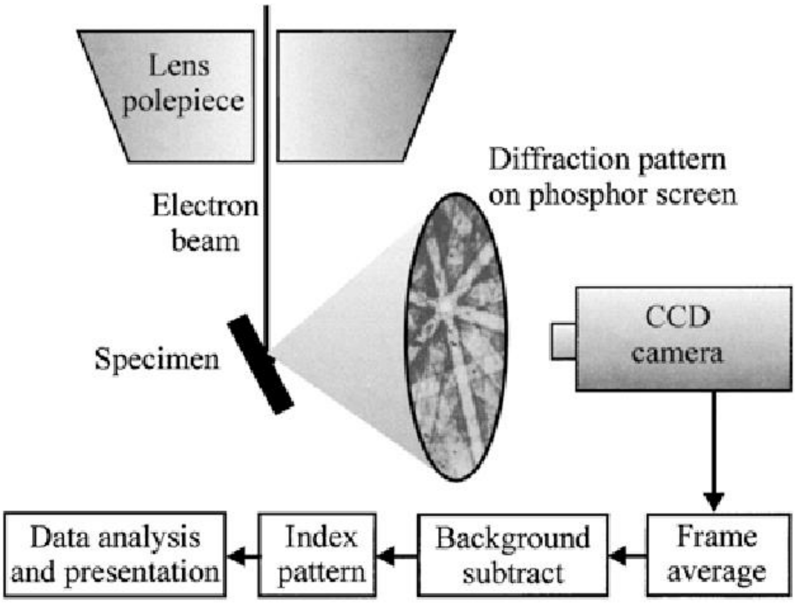

Figure 3-6: Schematic representation of a standard EBSD analysis setup[6].

Electron Backscatter Diffraction (EBSD) yields crucial insights into the crystallographic orientation of materials on a microscopic scale. including orientation maps, identification of grain boundaries, determination of grain size and shape, phase identification, analysis of deformation and strain, and examination of texture patterns [7]. The details of the EBSD technique is described elsewhere [7–9].

In the present work, grain orientation and local misorientation of the samples after different processing steps were characterized by electron backscatter diffraction (EBSD). The EBSD measurements were carried out on a FEI NOVANANO–SEM 450, with a beam voltage of 20KV, an aperture diameter of 50 µm and a working distance of 12-15 mm. The samples were tilted at 70 degrees towards the EBSD detector. The EBSD patterns were recorded by a

Velocity Pro camera using a hexagonal grid and processed by OIM-TSL software version 8.6. For high-resolution EBSD, a small area of 25 µm x 25 µm was scanned with a step size of 80 nm, covering at least two or three bands of different phases. For texture analysis, a larger area of 300 µm x 300 µm was scanned with a step size of 0.1 µm, using multiple measurements. Post-processing of data was performed using Version 8.6 of the OIM-analysis software. EBSD mis indexed data with a confidence index of less than 0.1 were excluded from subsequent analysis.

3.5.4 Partitioning of secondary constituents using EBSD data:

The EBSD data obtained for different dual phase microstructures in this study (Ferrite-pearlite, ferrite-bainite and ferrite-martensite) are partitioned to understand the changes in the corresponding phase/constituent. Prior work on partitioning of bainite and martensite from ferrite in multiphase steels ferrite-martensite was achieved by using IQ and KAM, which are sensitive to the lattice distortion of the phases [10,11]. Martensite usually shows lower IQ Kikuchi bands due to various crystalline defects such as sub grain, grain boundary, high dislocation density, lattice strain, and increased carbon content that distort the lattice [12]. Hence, one method to partition the images is to apply a filter to the original IQ image and generate multiple Gaussian distributions of the IQ values using a threshold IQ value [13]. However, this approach has been shown to be sensitive to the user-defined choice for the threshold number. Also, some prior work reports the relationship between IQ values and martensitic constituents [5] and has been used with some success [14]. However, they do not provide quantitative criteria to differentiate between ferrite, bainite, martensite, or high-angle grain boundaries, making the method very operator-dependent [15]. Stuart et al. [16] have suggested a kernel-based method for more precise measurement of phase discrimination in ferrite and martensite with minimum error compared to threshold method. Using the IQ of the diffraction pattern, the EBSD map data was employed to separate the regions of ferrite and second phase constituents, as suggested by [17]. Zaffrer et al. [18] have demonstrated that the KAM based approach is more dependable than other methods based on misorientation. However, it still is user dependent to some extent. In this work, image quality (IQ) map was used to separate the different phases based on their IQ values. Fig. 3-7 shows the SEM micrograph, IQ map and IQ-based partitioned map for Ferrite-Pearlite, where the pearlite phase has lower IQ values and the ferrite phase has higher IQ values. The partitioned map shows ferrite as grey coloured region and pearlite as red/yellow colored region, which matches well with the SEM micrograph and the IQ map. This IQ based partitioning technique[19] was then applied to KAM data to obtain the misorientations in ferrite and pearlite as shown in Fig. 3-7(d), where the pearlite phase has higher misorientation and the ferrite phase has lower misorientation. Good correlation of regions corresponding to ferrite and pearlite from SEM, IQ and partitioned IQ map can be observed from Fig. 3-7.

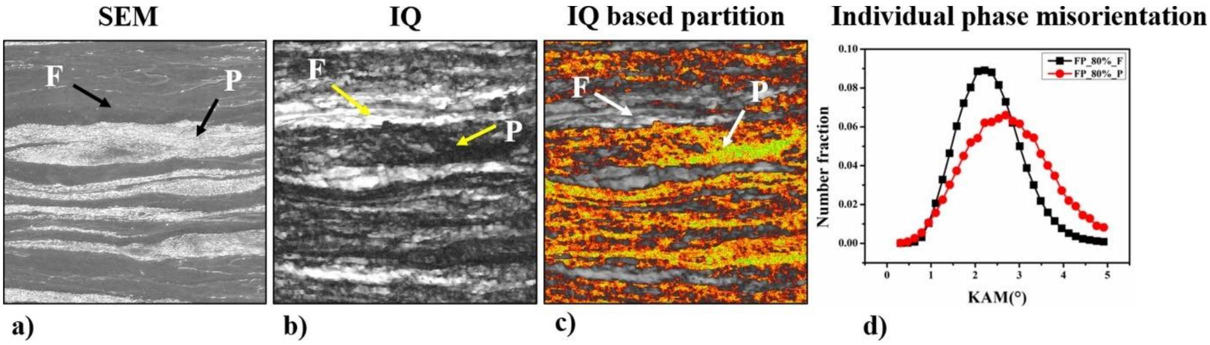

Figure 3-7: (a) SEM micrograph, (b) Image Quality map, (c) Image Quality-based partitioned map, and (d) the Kernel Average Misorientation (KAM) distribution of individual phases in Ferrite-Pearlite. "F" represents ferrite, and "P" represents pearlite.

3.6 Mechanical characterization:

In this study, hardness was measured by micro-Vickers hardness testing and nanoindentation testing to probe the mechanical properties at different length scales as described below.

3.6.1 Vickers micro hardness measurement:

The microhardness of the samples was measured by Vickers indentation using a Tinius Olsen FH-006 series instrument. The load was 500 gm and the dwell time was 15 s [20]. Fifteen indents were made on a flat and polished surface along the rolling direction for each sample. The hardness values obtained from the indents represent the average response of multiple grains of both constituents, i.e., ferrite-pearlite, ferrite-bainite and ferrite-martensite[4].

3.6.2 Nanoindentation hardness measurement:

High speed nanoindentation mapping was performed to measure the local mechanical properties at the micrometer length scale using a commercially available nanoindenter, iMicro® with an InForce50 actuator from Nanomechanics Inc. (now KLA), Oak Ridge, USA [19]. A high-speed mapping tool, NanoBlitz 3D+, was used to perform the mapping, with each indent taking less than a second to complete. The process involved navigating to the region of interest on the sample, making contact with the surface, loading, unloading, and withdrawing the tip further away from the surface [21]. The contact stiffness, hardness, and modulus were calculated from the load and depth information at each test point using the Oliver and Pharr method [22,23]. A diamond Berkovich tip was employed for all experiments [21]. Following the recommendation of Sudharshan Phani and Oliver in a previous work [22], the depth of indentation is limited to 100 nm and the spacing between the two consecutive indents is 1 micron which results in spacing to depth ratio of 10. Several maps of 60X60 sq. microns, with 3600 indents were carried out for all samples after different processing steps[19]. The outcome of constant strain rate testing (0.2 1/s) on fused silica were used to determine the load frame stiffness and tip area function [21]. For these experiments, the contact stiffness was measured continuously as a depth-dependent measurement using a phase lock amplifier with a frequency of 100 Hz and a constant ratio of dynamics load to means load of 0.2 as detailed elsewhere[4] [24]. It may be noted that the samples were etched after final polishing to capture the microstructure with SEM and EBSD. The samples were subsequently again polished with colloidal silica suspension to remove the etching effect before nanoindentation, wherein the material removal is minimal.

3.7 Deconvolution of data:

The k-means clustering algorithm was applied to the large data sets from hardness mapping to obtain the deconvoluted map also referred to as mechanical phase map that gives the local hardness of the different phases / constituents[19]. The k-means clustering algorithm [25] is a method to partition a set of ‘n’ observations into a set of ‘k’ groups, based on minimizing the within-cluster sum of squares of distances. The algorithm starts with k random cluster centres and iteratively updates them until the within-cluster distances cannot be reduced further and gives the deconvoluted map or the mechanical phase map [22,23]. The optimal number of clusters for the data can be determined by running the method for different values of k and choosing the best one based on error minimization, or by having prior knowledge of the number of phases present in the mapped region. The mean and standard deviation of the data points in each cluster can be used as a quantitative measure of the property of the respective phase / constituent after the clustering.

An example of the deconvolution is shown in Fig. 3-8. The SEM micrograph in Fig. 3-8(a) reveals the two-phase microstructure of ferrite and pearlite, while the hardness variation between these constituents is evident from Fig. 3-8(b). This nanoindentation mapping hardness data is deconvoluted into two bins corresponding to ferrite (blue) and pearlite (red), as shown in the deconvoluted map or mechanical phase map in Fig. 3-8(c). Good agreement is observed between the SEM micrograph, the hardness map and the deconvoluted hardness map in terms of the spatial distribution of ferrite and pearlite in Fig. 3-8(a-c). The mean and standard deviation of the hardness details for individual phases were calculated and used to plot the hardness histogram considering a Gaussian spread [21]. The histograms of the hardness data for ferrite and pearlite are depicted in Fig. 3-8(d), where the peak position indicates the average hardness and the peak area represents the area fraction of each phase. The changes in hardness after hot rolling and coiling, cold rolling, recrystallization and intercritical annealing were analysed in a similar way in the thesis.

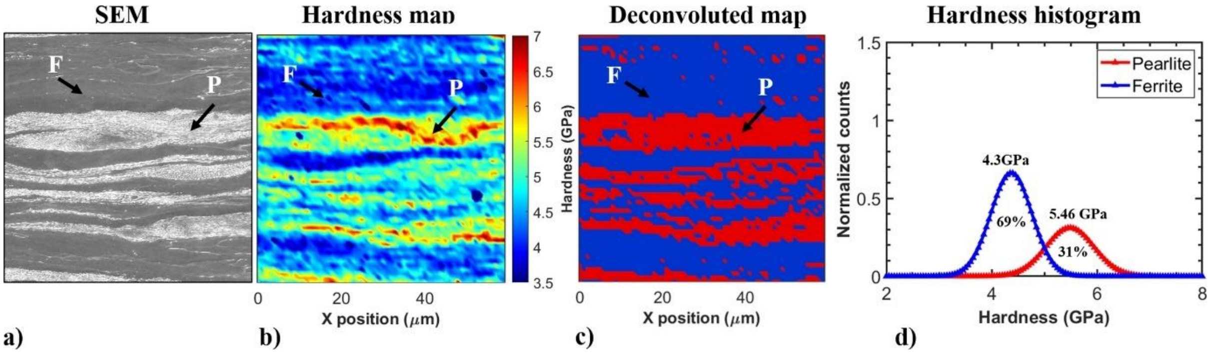

Figure 3-8: (a) SEM micrograph (b) nanoindentation-derived hardness mapping, (c) deconvoluted or mechanical phase map with ferrite (blue) and pearlite (red), and (d) histogram depicting the hardness distribution of individual constituents.

3.8 References:

[1] J. Gautam, A. Miroux, J. Moerman, C. Barbatti, P. Van Liempt, L.A.I. Kestens, Determination of the non-recrystallisation temperature (Tnr) of austenite in high strength C-Mn steels, Mater. Sci. Forum. 706–709 (2012) 2722–2727. https://doi.org/10.4028/www.scientific.net/MSF.706-709.2722.

[2] S. Janakiram, P.S. Phani, G. Ummethala, H.V. Jagdeesh, S.K. Malladi, J. Gautam, L.A.I. Kestens, Insights on early recovery kinetics in ferrite - pearlite cold rolled high strength sheet steels, Mater. Charact. 193 (2022). https://doi.org/10.1016/j.matchar.2022.112332.

[3] V.S. Hariharan, Phase fraction calculation of microstructure using ImageJ, Res. Gate. (2018) 17. https://doi.org/10.13140/RG.2.2.22990.51521.

[4] J.-Y. Kang, D.-I. Kim, H.-C. Lee, Texture Development in Low Carbon Sheet Steels for Automotive Application, Microstruct. Texture Steels. (2009) 85–101. https://doi.org/10.1007/978-1-84882-454-6_5.

[5] Oxford Instruments, Electron Backscatter Diffraction - EBSD, Elsevier Ltd, n.d. https://nano.oxinst.com/products/ebsd/.

[6] F. Humphreys, Grain and subgrain characterisation by electron backscatter diffraction, Mater. Sci. (2001) 17653.

[7] S. Suwas, R.K. Ray, Crystallographic Texture of Materials, 2014. https://doi.org/10.1007/978-1-4471-6314-5_5.

[8] B.L. (Eds.). Schwartz, A. J., Kumar, M., & Adams, Electron Backscatter Diffraction in Materials Science, 2000. https://doi.org/doi:10.1007/978-1-4757-3205-4 DOI 10.1007/978-0-387-88136-2.

[9] E. R. Davies, Introduction to Texture Analysis Handbook, An Autom. Irrig. Syst. Using Arduino Microcontroller. 1908 (2011) 2–6. https://doi.org/https://doi.org/10.1142/9781848161160_0001.

[10] M. Calcagnotto, Y. Adachi, D. Ponge, D. Raabe, Deformation and fracture mechanisms in fine- and ultrafine-grained ferrite/martensite dual-phase steels and the effect of aging, Acta Mater. 59 (2011) 658–670. https://doi.org/10.1016/j.actamat.2010.10.002.

[11] M. Calcagnotto, D. Ponge, E. Demir, D. Raabe, Orientation gradients and geometrically necessary dislocations in ultrafine grained dual-phase steels studied by

2D and 3D EBSD, Mater. Sci. Eng. A. 527 (2010) 2738–2746. https://doi.org/10.1016/j.msea.2010.01.004.

[12] E.A. Ariza-Echeverri, M. Masoumi, A.S. Nishikawa, D.H. Mesa, A.E. Marquez-Rossy, A.P. Tschiptschin, Development of a new generation of quench and partitioning steels: Influence of processing parameters on texture, nanoindentation, and mechanical properties, Mater. Des. 186 (2020) 108329. https://doi.org/10.1016/j.matdes.2019.108329.

[13] S.H. Choi, E.Y. Kim, W. Woo, S.H. Han, J.H. Kwak, The effect of crystallographic orientationonthe micromechanical deformation and failure behaviors of DP980 steel during uniaxial tension, Int. J. Plast. 45 (2013) 85–102. https://doi.org/10.1016/j.ijplas.2012.11.013.

[14] M.J. Santofimia, R.H. Petrov, L. Zhao, J. Sietsma, Microstructural analysis of martensite constituents in quenching and partitioning steels, Mater. Charact. 92 (2014) 91–95. https://doi.org/10.1016/j.matchar.2014.03.003.

[15] M. De Meyer, L. Kestens, B.C. De Cooman, Texture development in cold rolled and annealed C-Mn-Si and C-Mn-Al-Si TRIP steels, Mater. Sci. Technol. 17 (2001) 1353–1359. https://doi.org/10.1179/026708301101509557.

[16] S.I. Wright, M.M. Nowell, EBSD image quality mapping, Microsc. Microanal. 12 (2006) 72–84. https://doi.org/10.1017/S1431927606060090.

[17] J. Wu, P.J. Wray, C.I. Garcia, M. Hua, A.J. Deardo, Image quality analysis: A new method of characterizing microstructures, ISIJ Int. 45 (2005) 254–262. https://doi.org/10.2355/isijinternational.45.254.

[18] P.R.& F.F. S. ZAEFFERER∗, EBSD as a tool to identify and quantify bainite and

ferrite in low-alloyed Al-TRIP steels, J. OfMicroscopy. 230 (2008) 499–508. https://doi.org/https://doi.org/10.1111/j.1365-2818.2008.02010.x.

[19] S. Janakiram, P.S. Phani, G. Ummethala, S.K. Malladi, J. Gautam, L.A.I. Kestens, New insights on recovery and early recrystallization of ferrite-pearlite banded cold rolled high strength steels by high speed nanoindentation mapping, Scr. Mater. 194 (2021) 113676. https://doi.org/10.1016/j.scriptamat.2020.113676.

[20] S. Janakiram, J.P. Gautam, A. Miroux, J. Moerman, L. Kestens, Microstructure and Texture Control in Cold Rolled High Strength Steels, Diffus. Found. 22 (2019) 84–93. https://doi.org/10.4028/www.scientific.net/df.22.84.

[21] J.J. Roa, P. Sudharshan Phani, W.C. Oliver, L. Llanes, Mapping of mechanical properties at microstructural length scale in WC-Co cemented carbides: Assessment of hardness and elastic modulus by means of high speed massive nanoindentation and statistical analysis, Int. J. Refract. Met. Hard Mater. 75 (2018) 211–217. https://doi.org/10.1016/j.ijrmhm.2018.04.019.

[22] P. Sudharshan Phani, W.C. Oliver, A critical assessment of the effect of indentation spacing on the measurement of hardness and modulus using instrumented indentation testing, Mater. Des. 164 (2019) 107563. https://doi.org/10.1016/j.matdes.2018.107563.

[23] B. Vignesh, W.C. Oliver, G.S. Kumar, P.S. Phani, Critical assessment of high speed nanoindentation mapping technique and data deconvolution on thermal barrier coatings, Mater. Des. 181 (2019) 108084. https://doi.org/10.1016/j.matdes.2019.108084.

[24] P. Sudharshan Phani, W.C. Oliver, G.M. Pharr, Measurement of hardness and elastic modulus by load and depth sensing indentation: Improvements to the technique based on continuous stiffness measurement, J. Mater. Res. 36 (2021) 2137–2153.

https://doi.org/10.1557/s43578-021-00131-7.

[25] M.A.W. J. A. Hartigan, Algorithm AS 136 A K-Means Clustering Algorithm, J. R. Stat. Soc. Ser. B Methodol. 28 (2012) 100–108. https://doi.org/http://www.jstor.org/page/info/about/policies/terms.jsp .

Chapter 4 The influence of coiling temperature and cooling rate on microstructure and mechanical properties of dual phase microstructures

In this chapter, we explore the formation of dual-phase microstructures during the hot rolling and coiling process, utilizing a correlative approach that combines nanoindentation and electron microscopy for the analysis of Advanced High Strength Steels (AHSS). Our investigation resulted in microstructures characterized by the presence of ferrite in conjunction with pearlite, bainite, and martensite, all while maintaining an equivalent nominal carbon content. High-speed nanoindentation mapping was employed to capture the variation in local mechanical properties with respect to the processing parameters. Notably, we observed excellent agreement between the microstructure and hardness at the micrometer length scale. This chapter elucidates the outcomes concerning the influence of carbon distribution on the evolution of microstructure and properties during hot rolling and coiling.

4.1 Introduction

DP steel grades are a category of Advanced High Strength Steels that exhibit a unique combination of high ductility and strength. These grades have a microstructure consisting of about 70-80 volume percent of ferrite (α-iron) as the primary phase, with the remaining secondary phase/constituent being one or more of bainite, pearlite, and martensite. The morphology of the secondary phases/constituent and the relative distribution of constituent elements, especially carbon in these phases, influences the overall performance of the composite [1,2]. Specifically, thermomechanical control processing (TMCP) parameters such as rolling conditions, coiling temperature, soaking duration, cooling rates, etc. can affect the distribution and morphology of the secondary phase(s) and thereby the mechanical properties.

Prior work in this regard focused on obtaining dual phase microstructures with different morphologies and volume fractions. The choice of hot rolling temperature and the subsequent coiling temperature plays an important role [1–7], resulting in a wide range of microstructures, including ferrite-pearlite with banded type morphology [8–11] at high coiling temperature and ferrite-bainite and ferrite-martensite with non-banded morphology at low coiling temperature and higher cooling rate [12]. For example, Zhuang et al.[13], showed that low temperature rolling followed by rapid cooling results in materials with higher ultimate tensile strength due to refinement of ferrite grains and formation of martensite islands in the microstructure. Similarly, Gang et al. [14] showed that in high Al and low Si DP steel coiled at a temperature of 300ºC, dislocation density in ferrite was relatively low and auto tempering of martensite occurs that leads to softening and thereby a decrease in the hardness difference between ferrite and martensite. Apart from the coiling temperature and cooling rate effect, the evolution of the mechanical properties with thermo-mechanical processing and composition has not been comprehensively studied. The strength of many of these dual phase steels is usually measured by using Vickers micro hardness [15–18] and tensile testing [19,20]. While tensile testing naturally provides a composite response, indentation can potentially yield the properties of individual constituents. However, the size of the second phase is usually much smaller than the indent size in the case of micro Vickers hardness testing and hence only the composite response of ferrite and second phase is obtained [15–17]. However, nanoindentation testing, which can access much smaller length scales is a potential alternative. In this regard, recent advancements in high speed nanoindentation mapping have enabled the extraction of local mechanical properties of multiphase materials including DP steels [21–23].

In this chapter, a comprehensive study of the local mechanical properties of hot rolled and coiled dual phase steels is presented. Three different dual phase steel microstructures are obtained by hot rolling followed by coiling at different temperatures. Microstructural and mechanical properties are discussed in detail in the experimental procedure chapter. Insights on the effect of carbon distribution on local microstructure and the hardness of individual phases are presented. A critical assessment of microstructure and mechanical property correlation at the micrometer length scale is presented. These microstructures then become the basis for further thermomechanical processing steps such as cold rolling, recrystallization and inter-critical annealing that are the other key processing steps for DP steels which are discussed in subsequent chapters.

4.2 Experimental procedure

4.2.1 Processing of steel

A 37 mm thick industrial grade DP600 steel slab, sourced from Tata Steel in Europe, was subjected to hot rolling at a temperature of 876°C, which exceeds the austenite recrystallization temperature. This hot rolling process resulted in a reduction of the slab's thickness to 6 mm, representing an 83% reduction in thickness[24], and coiling at different temperature with different cooling rate to develop the three distinct microstructures with ferrite as matrix and secondary constituent / phase comprising of pearlite, bainite and martensite. The processing steps are detailed in the chapter 3.

4.2.2 Microstructural and mechanical characterization

Microstructural investigations were carried out using field emission scanning electron microscope (FESEM Model: FEI - NOVA NANOSEM450) at an accelerating voltage of 20 kV and a working distance of 15 mm. EBSD measurements were performed using a velocity pro detector from EDAX, and TSL OIM software (version 8.5) was used for further analysis. Local misorientations were studied using the Kernel average misorientation (KAM) maps which are obtained with respect to 5th nearest neighbor and maximum threshold of 3° misorientation. As mentioned earlier, mechanical testing was performed on well-polished samples by microhardness and nanoindentation testing. Vickers micro hardness tests were carried out using Tinius Olsen FH-006 series at a load of 500 gm and dwell time of 15 s [25]. High speed nanoindentation mapping was performed to measure the local mechanical properties at the micrometer length scale using a commercially available nanoindenter, iMicro® with an InForce50 actuator from Nanomechanics Inc. (now KLA), Oak Ridge, USA [26–28]. Further details of material characterization are provided in chapter 3.

4.3 Results

4.3.1 Microstructural observations from SEM micrographs

The difference in coiling temperatures during the hot rolling process is clearly visible in the SEM micrographs shown in Fig. 4-1 in terms of variations in microstructural features. As seen in Fig. 4-1(a-c), these variations are seen in the morphology and distribution of microstructural characteristics. In all micrographs, the matrix phase is ferrite (dark grey), while the second phase or constituent (light grey) is either pearlite (as shown in Fig. 4-1(a, d)), bainite (as seen in Fig. 4-1(b, e)), or martensite (as observed in Fig. 4-1(c, f)). Higher magnification images of the regions shown in the inset are shown in Fig. 4-1(d-f) that clearly show the differences in the morphology and length scale of the second phase / constituent. Slow cooling followed by coiling at 600°C resulted in ferrite and a colony of pearlite and is banded in nature as shown in Fig. 4-1(a) and (d). Faster cooling followed by coiling at 450°C resulted in formation of bainite, wherein the bainite shows a lath-type morphology with fragmented iron carbides and ferrite as shown in Fig. 4-1(b) and (e). Finally, much faster cooling followed by coiling at 250°C, resulted in fine martensitic islands dispersed across the ferrite region. It may be noted that coiling at 450°C and 250°C did not result in banding. Also, with decreasing coiling temperature, ferrite grain size decreases. The grain size of ferrite estimated to be 14±3.89 µm, 10.5±3.9 µm and 5.64±2.4 µm for FP, FB and FM, respectively. In summary, despite having similar composition, significant difference in area fraction and distribution of the constituent phases can be clearly observed.

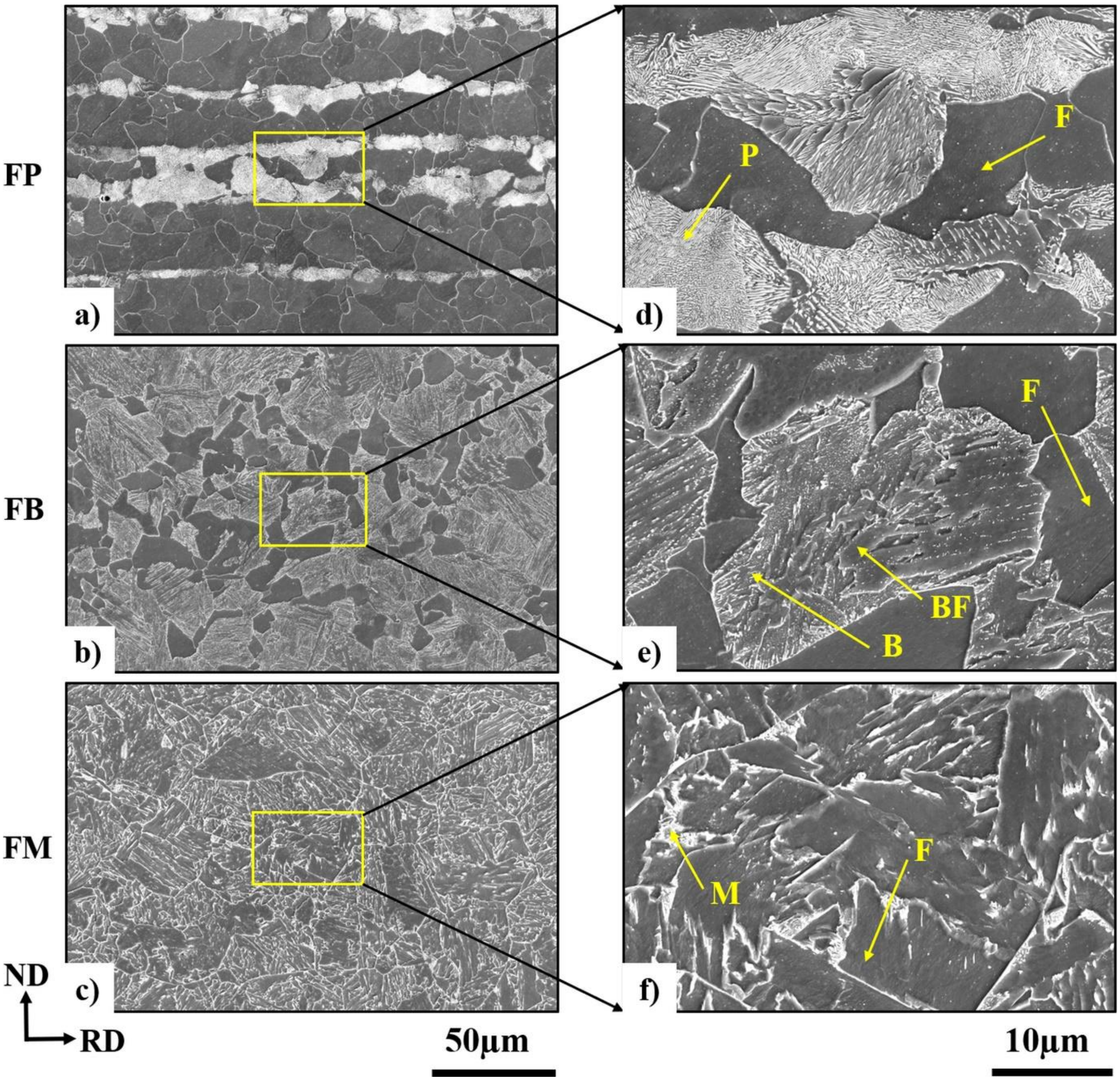

Figure 4-1: SEM micrographs after hot rolling and coiling at different temperatures (a, d) ferrite-pearlite (FP), (b, e) ferrite-bainite (FB) and (c, f) ferrite-martensite (FM).

4.3.2 Microstructural observation from EBSD (KAM analysis)

We also carried out Electron Backscatter Diffraction (EBSD) examinations to better understand how local misorientations during processing, in addition to the microstructural analysis mentioned in the prior subsection. The kernel average misorientation (KAM) maps for the three distinct microstructures are shown in Fig. 4-2. The misorientations on these maps are represented by a colour spectrum from blue to red that spans a 3-degree range. In the case of FP, bulk ferrite regions (blue-colored regions) show lower misorientation, while the pearlite regions show higher misorientation. Similarly, in the case of FB, bulk ferrite regions (blue-colored regions) show lower misorientation, whereas the regions where ferrite is intermixed with bainite or in the vicinity of bainite, show relatively higher misorientations. On the contrary, in the case of FM, the ferrite regions show much higher misorientation as evidenced by the lack of blue colored regions, while they are still lower than the martensitic regions. The variations in misorientation can be attributed to the strain that accumulates during the formation of the phases/constituents at different cooling rates and coiling temperatures.

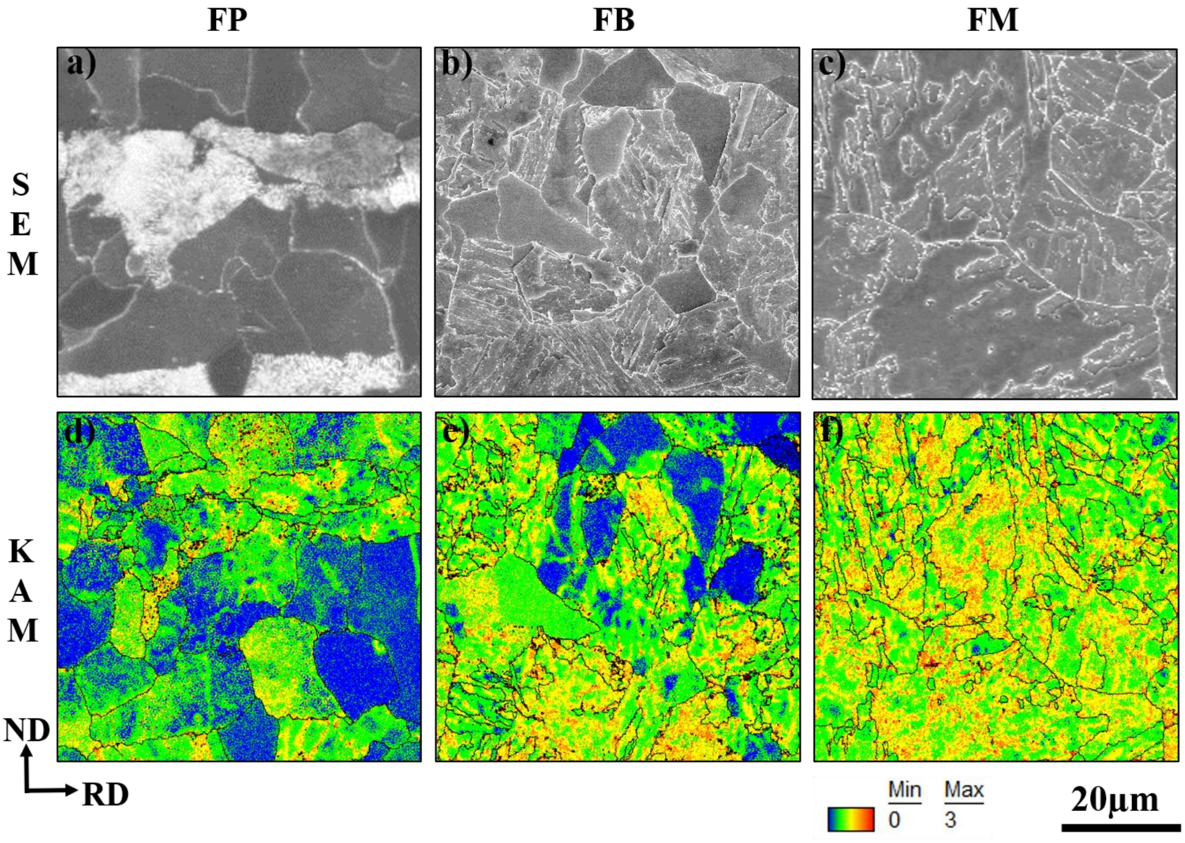

Figure 4-2: SEM micrographs and kernel average misorientation maps of FP, FB and FM.

4.3.3 KAM distribution of ferrite and secondary constituents:

To quantify the information derived from the KAM maps shown in Fig. 4-2, we present histograms illustrating the distribution of KAM values. Specifically, Fig. 4-3(a) pertains to bulk ferrite, while Fig. 4-3(b) corresponds to the secondary phase or constituent and the petitioning was carried out as described in chapter 3 based on the work of Janakiram et. al.[21]. For bulk ferrite, as indicated in Fig. 4-3(a), the FP and FB samples exhibit lower misorientations in comparison to FM. This can be attributed to several factors, including the relatively lower defect density in FP due to its slower cooling rates, as well as the finely distributed martensite in FM, which contributes to localized increases in the defect density within the ferrite phase. In the case of the secondary phase / constituents shown in Fig. 4-

3(b), the pearlite peak shows the lowest misorientation, while bainite and martensite show a slightly higher value. It may be noted that the secondary constituents are pearlite in the case of FP, mixture of ferrite and bainite/carbide in the case of FB and martensite in the case of FM.

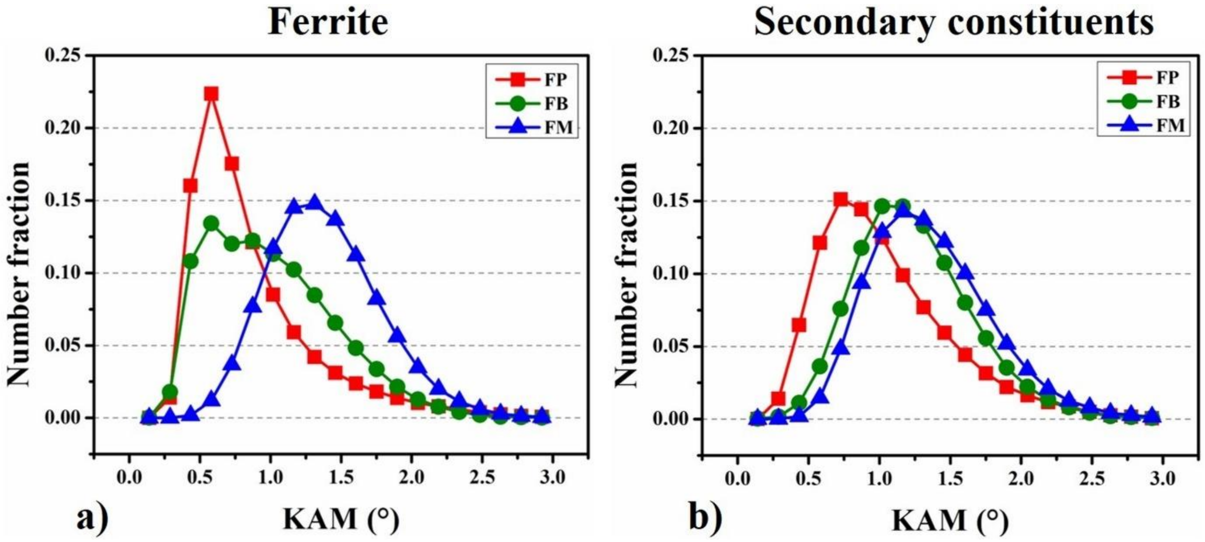

Figure 4-3: Kernel average misorientation (KAM) distribution in (a) bulk ferrite and (b) secondary phase / constituents.

4.3.4 Micro vickers hardness evolution

Fig. 4-4 illustrates the microhardness data acquired through Vickers indentation subsequent to the hot rolling and coiling processes for all three samples. Notably, the microhardness exhibits an increasing trend, starting with FP and followed by FB and FM. This trend can be rationalized by considering that martensite, formed through rapid cooling, has the potential to refine the ferrite microstructure and enhance local matrix strength due to an increased dislocation density. However, it’s important to note that detailed microstructural information at smaller length scales is not accessible due to the relatively larger size of the hardness impressions in comparison to the microstructural length scale. To delve deeper into deformation at smaller scales, we have conducted nanoindentation testing.

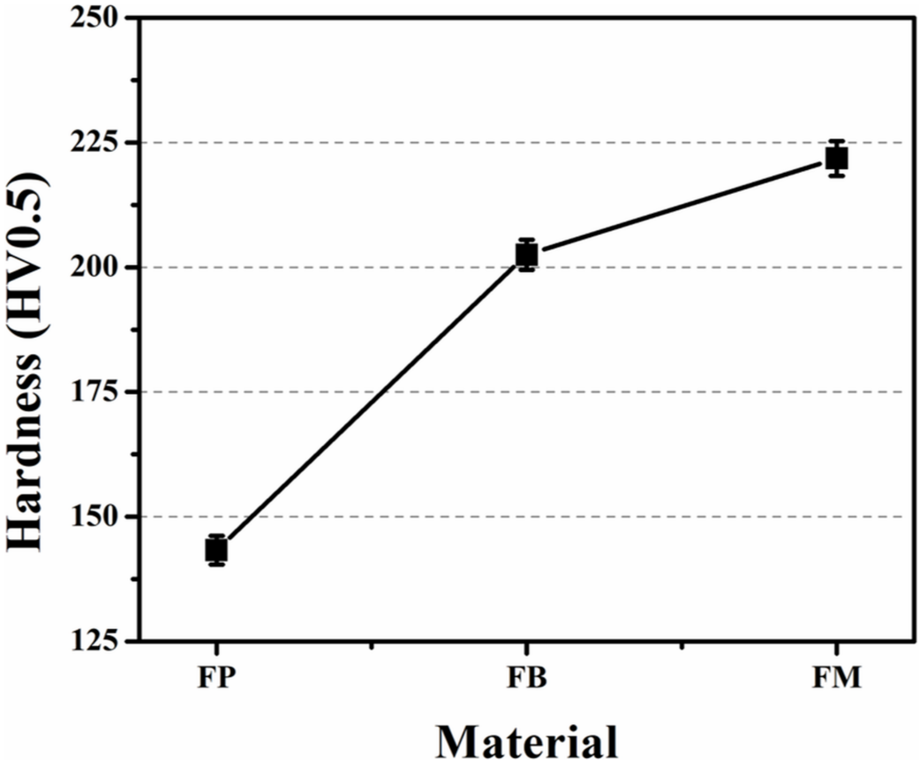

Figure 4-4: Vickers microhardness of hot rolled and coiled samples of FP, FB and FM.

4.3.5 Nanoindentation hardness mapping after hot rolling and coiling

In Fig. 4-5, we present representative high-speed nanoindentation maps alongside their respective histograms for all three samples. In the hardness map of FP (Fig. 4-5(a)), the banded nature of the microstructure is distinctly evident, with bulk ferrite exhibiting lower hardness compared to pearlite. For FB (Fig. 4-5(b)), similar observations hold true, with bulk ferrite regions displaying lower hardness, and areas featuring ferrite intermixed with bainite or carbides showing higher hardness and increased heterogeneity. Moving to FM (Fig. 4-5(c)), the ferrite regions are relatively harder when compared to FB, and we observe localized regions of high hardness corresponding to martensite. It is worth noting that despite the identical nominal composition in all three cases, the hardness maps exhibit significant variations, mirroring the trends observed in the KAM maps depicted in Fig. 4-3. It is important to highlight that in the case of FP, the clear differentiation between bulk ferrite and pearlite is due to the coarser length scale of the microstructure. However, in the cases of FB and particularly FM, distinguishing between bulk ferrite and the secondary constituent becomes less clear due to the significantly finer length scale. Consequently, quantifying the hardness of this finer constituent presents a notable challenge. While we will delve into a comprehensive examination of microstructure-property relationships at the micrometer length scale in the forthcoming section, we provide a comparison of the overall hardness histograms across the samples in Fig. 4-5(d). Notably, FP and FB samples display two distinct peaks in their histograms, with the first peak corresponding to bulk ferrite and the second peak to the associated secondary constituent. In contrast, the finer length scale of martensite, combined with its widespread distribution throughout the sample, results in a single broad peak in the case of FM. These histograms, as displayed in the plot, encompass the entirety of the map data. To gain further insights into the evolution of each constituent with processing, it is imperative to undertake a deconvolution of the hardness maps, which will be discussed in detail in the next section.

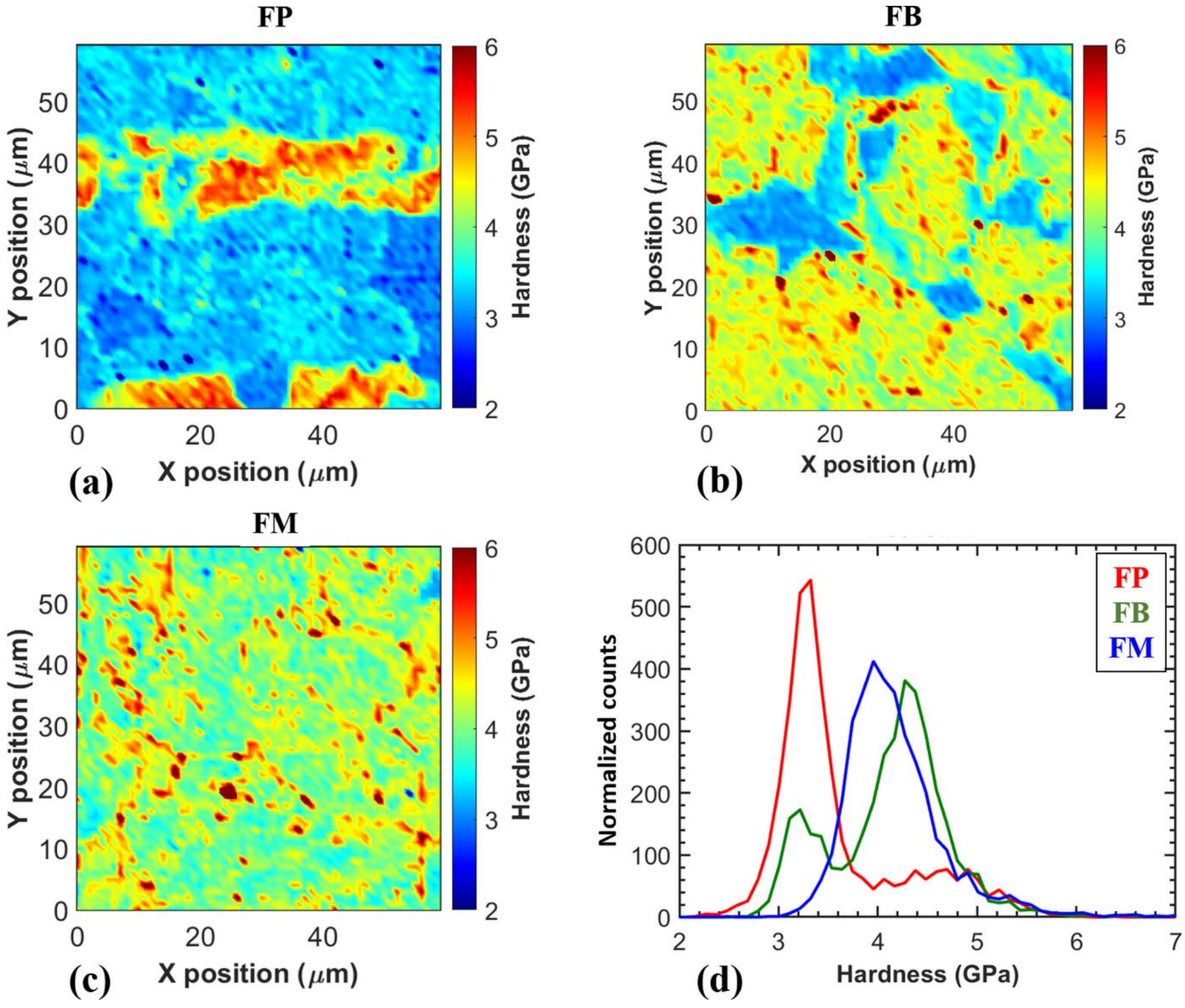

Figure 4-5: Nanoindentation hardness maps for hot rolled and coiled samples of (a) FP, (b) FB, and (c) FM, along with (d) hardness histograms.

4.4 Discussion

4.4.1. Assessment of microstructure and mechanical property correlation at the micrometer length scale

The preceding section has demonstrated notable localized variations in microstructure and mechanical properties due to differences in processing conditions. It is imperative to note that the critical start temperature and the cooling rate during the transformation from the austenite phase to pearlite, bainite, and martensite have substantial impact on the formation, morphology, distribution, and resulting mechanical characteristics of these constituents. The differences in carbon distribution during these transformation processes play a pivotal role in shaping their distinct microstructural features and, consequently, the mechanical properties they exhibit. As a brief recap, following hot rolling at 876ºC, the specimens were subjected to cooling to 725ºC to facilitate ferrite formation. Subsequent cooling at varying rates was then employed to reach the respective coiling temperatures, resulting in the formation of different secondary phases or constituents.

In the case of FP, a slow cooling rate of 5ºC/s was utilized to reach the coiling temperature, which corresponds to the pearlite start temperature (Ps) at 600ºC. This slow cooling rate predominantly triggers diffusion-controlled transformation, driving the formation of pearlite. During this process, carbon atoms diffuse from the austenite phase and redistribute into the ferrite and cementite phases. The resulting microstructure exhibits a banded morphology of pearlite, a characteristic feature clearly evident in Fig. 4-6(a) for FP, where pearlite bands are surrounded by bulk ferrite. It's worth noting that prior research has demonstrated that the major alloying element, Mn, tends to segregate significantly at both micro and macro scales, typically falling within the range of 1.5 to 3 wt. pct, contributing to the banded structure observed in pearlite. Consequently, ferrite formation results in a higher carbon content in the surrounding austenite, which is rich in Mn, effectively lowering the local A3 temperature. Subsequent cooling leads to the continued decomposition of austenite, resulting in the formation of pearlite in a banded pattern, a characteristic prominently observed in the microstructure of FP as depicted in Fig. 4-6(a), where pearlite bands are enveloped by bulk ferrite.

To establish a meaningful correlation between microstructure and mechanical properties, a comparison was made between the hardness maps and etched micrographs from a representative region. Fig. 4-6(b) presents the hardness map corresponding to the microstructure showcased in Fig. 4-6(a), revealing that pearlite bands exhibit higher hardness compared to the surrounding bulk ferrite. Employing a k-means clustering algorithm[21–23], the hardness map can be algorithmically deconvoluted, resulting in the creation of a deconvoluted map or mechanical phase map as depicted in Fig. 4-6(c). In this mechanical phase map, the blue region predominantly represents bulk ferrite, while the red region corresponds predominantly to pearlite. Upon careful examination of Fig. 4-6, it becomes evident that the clear contrast distinctions between ferrite and pearlite observed in the microstructure are accurately captured within the hardness map. This agreement is further corroborated by the zoomed-in view of a small region in the micrograph (Fig. 4-6(d)) and the corresponding hardness map (Fig. 4-6(e)), emphasizing the excellent agreement between the microstructure and hardness map at the micrometer length scale. As previously discussed, the hardness map of FP successfully replicates the banded morphology evident in the microstructure. In this case, the pearlite region comprises a mixture of cementite and ferrite, rendering it harder than the surrounding bulk ferrite. Similar to the case of microstructure and hardness map, a comparison between the mechanical phase map presented in Fig. 4-6(c) and the microstructure in Fig. 4-6(a) demonstrates a high degree of agreement, thus validating the effectiveness of the deconvolution algorithm. The hardness histograms of individual constituents obtained post-deconvolution are displayed in Fig. 4-6(f). The counts have been normalized to reflect the relative area fractions, aligning well with the microstructural observations. As anticipated, the ferrite peak exhibits a lower hardness of 3.5 GPa, in contrast to the pearlite peak at 4.6 GPa, which can be regarded as the average hardness values for the respective regions.

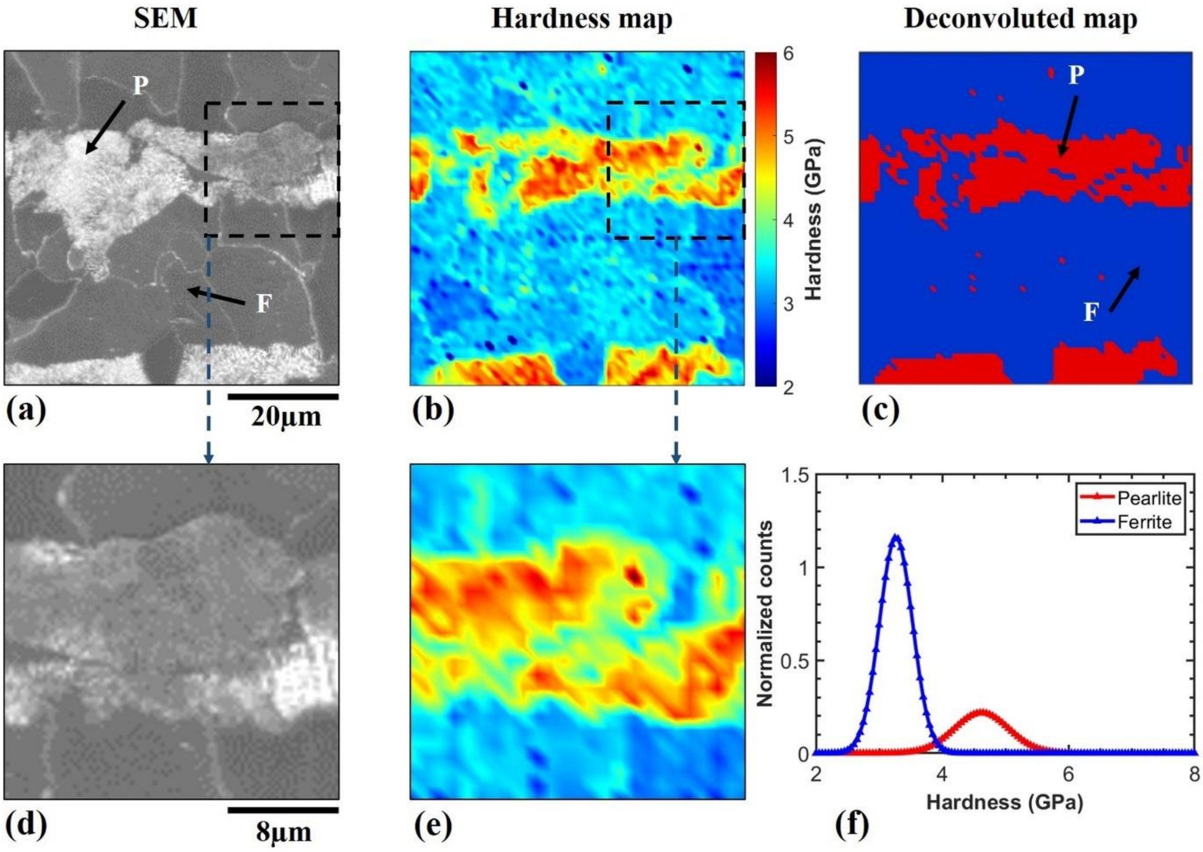

Figure 4-6: (a-d) SEM micrograph, the corresponding (b-e) hardness map, (c) mechanical phase map and (f) deconvoluted hardness distribution of FP.

In the case of FB, a relatively higher cooling rate of 20ºC/s was applied up to the coiling temperature of 450ºC, which corresponds to the bainite start temperature (Bs). This accelerated cooling process facilitated the transformation of austenite into bainite, resulting in a fine lath-like morphology in the bainitic region, accompanied by the distribution of fine carbides as depicted in Fig.-4-7(a) and 4-7(e). Fig. 4-7(b) presents the corresponding hardness map, revealing two distinct regions. One region corresponds to bulk ferrite, characterized by lower hardness, while the other corresponds to a region with a ferrite-bainite mixture, exhibiting higher hardness. For a closer examination, a zoomed-in view of the marked region in the micrograph (Fig. 4-7(d)) and the corresponding hardness map (Fig. 4-7(e)) are provided. Similar to the case of FP, an exceptionally good correlation between the microstructure and hardness at the micrometer length scale is evident. The hardness map effectively captures not only the bulk ferrite regions but also the local variations in hardness within the finer-length-scale ferrite-bainite intermixed region.

The mechanical phase map, derived from the deconvolution of the hardness data into two distinct regions, is presented in Fig. 4-7(c). In this map, the blue regions correspond to bulk ferrite, while the red regions represent a mixture of ferrite and bainite/carbides. It's noteworthy that assessing the hardness of the carbides/bainite, isolated from the surrounding ferrite poses challenges due to their fine length scale. Fig. 4-7(f) displays the hardness histograms obtained from the deconvoluted data. In these histograms, the ferrite peak is at 3.5 GPa, while the peak for the ferrite-bainite mixed region is observed at 4.5 GPa. An interesting observation is that, unlike FP where the bulk ferrite fraction is approximately 70%, in this case, the bulk ferrite area fraction is notably lower at 36%, with the majority, 64%, constituting the ferrite-bainite mixed region. Furthermore, the width of the peak corresponding to the ferrite-bainite mixture is broader, indicating an increased level of heterogeneity within this mixed region.

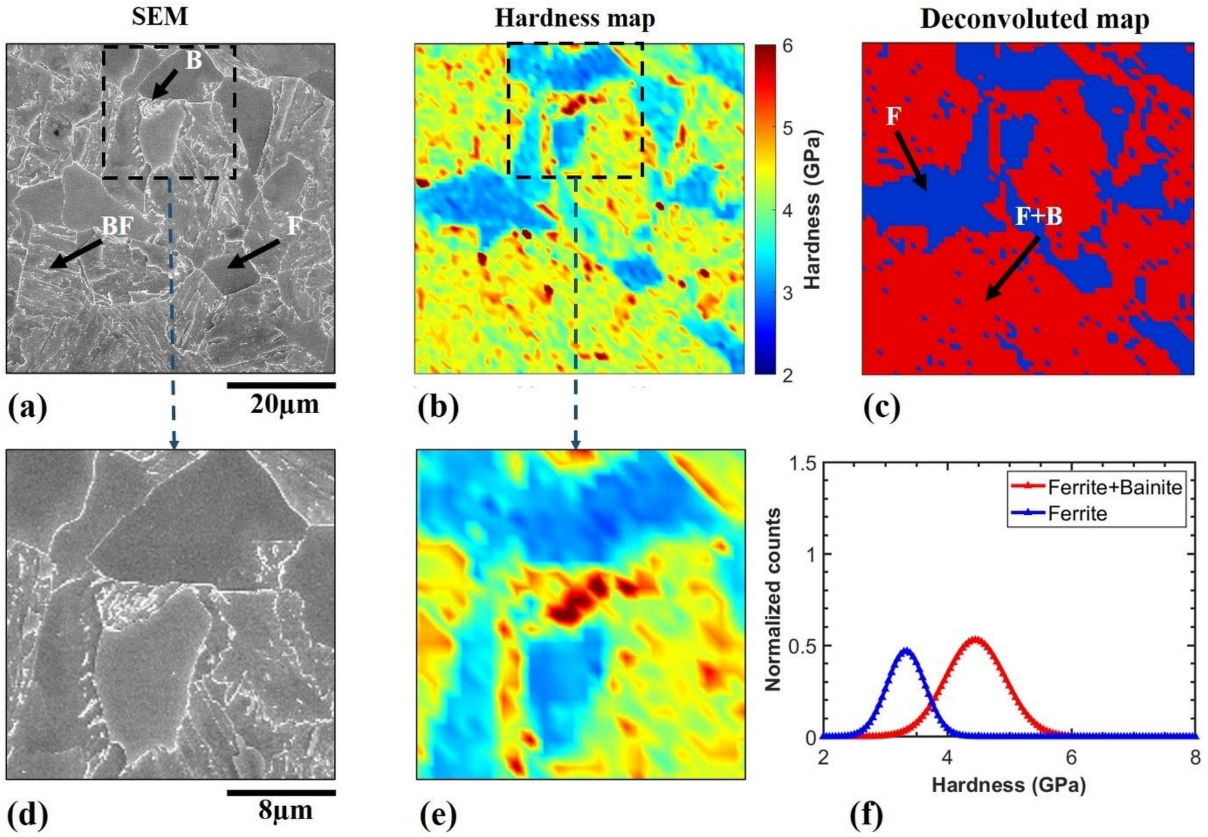

Figure 4-7: (a-d) SEM micrograph, the corresponding (b-e) hardness map, (c) mechanical phase map and (f) deconvoluted hardness distribution of FB.

For FM, a rapid cooling rate of 80ºC/s was employed up to the coiling temperature, which is the martensite start temperature (Ms), facilitating the transformation of austenite into martensite. As evidenced in Fig. 4-8(a), the SEM micrograph exhibits a very fine distribution of martensite dispersed throughout the ferrite region. The corresponding hardness map is displayed in Fig. 4-8(b). Further insight is provided through the zoomed-in view of the region highlighted in the micrograph (Fig. 4-8(d)) alongside its corresponding hardness map (Fig. 4-8(e)). Remarkably, despite the finer microstructure achieved in FM, a commendable agreement between microstructure and hardness is observed at the micrometer length scale. For instance, the martensite situated along boundaries, identifiable as bright regions in the micrograph (Fig. 4-8(d)), exhibits a corresponding high hardness in the hardness map (Fig. 4-8(e)). Additionally, grain interiors also display elevated hardness levels, corresponding to an intermediate shade of grey. It is noteworthy that in this case, the ferrite exhibits higher hardness in comparison to FP and FB, highlighting distinctive mechanical properties within this specific microstructure. These findings can be rationalized by differences in the cooling rate. Higher cooling rates effectively impede the growth of ferrite, creating more nucleation sites conducive to the formation of martensite. This results in a uniform distribution of martensite along the boundaries and within the matrix. The deconvoluted hardness map or mechanical phase map is illustrated in Fig. 4-8(c), with the blue regions corresponding to ferrite and the red regions to martensite. Remarkably, this map exhibits a good agreement with the microstructure depicted in Fig. 4-8(a), thereby validating the efficacy of the deconvolution procedure, even when dealing with a finer length scale microstructure. The histograms derived from the deconvoluted data are presented in Fig. 4-8(e), where the ferrite peak is around 4 GPa, while the martensite peak is at approximately 5 GPa. It is important to note that despite the favourable alignment between microstructure and hardness maps, the smaller length scale of martensite, which closely approaches the indent spacing of 1 µm, can introduce an element of mutual influence from neighbouring phase in the measurement of hardness. Consequently, this interaction may lead to an underestimation of martensite hardness and an overestimation of ferrite hardness.

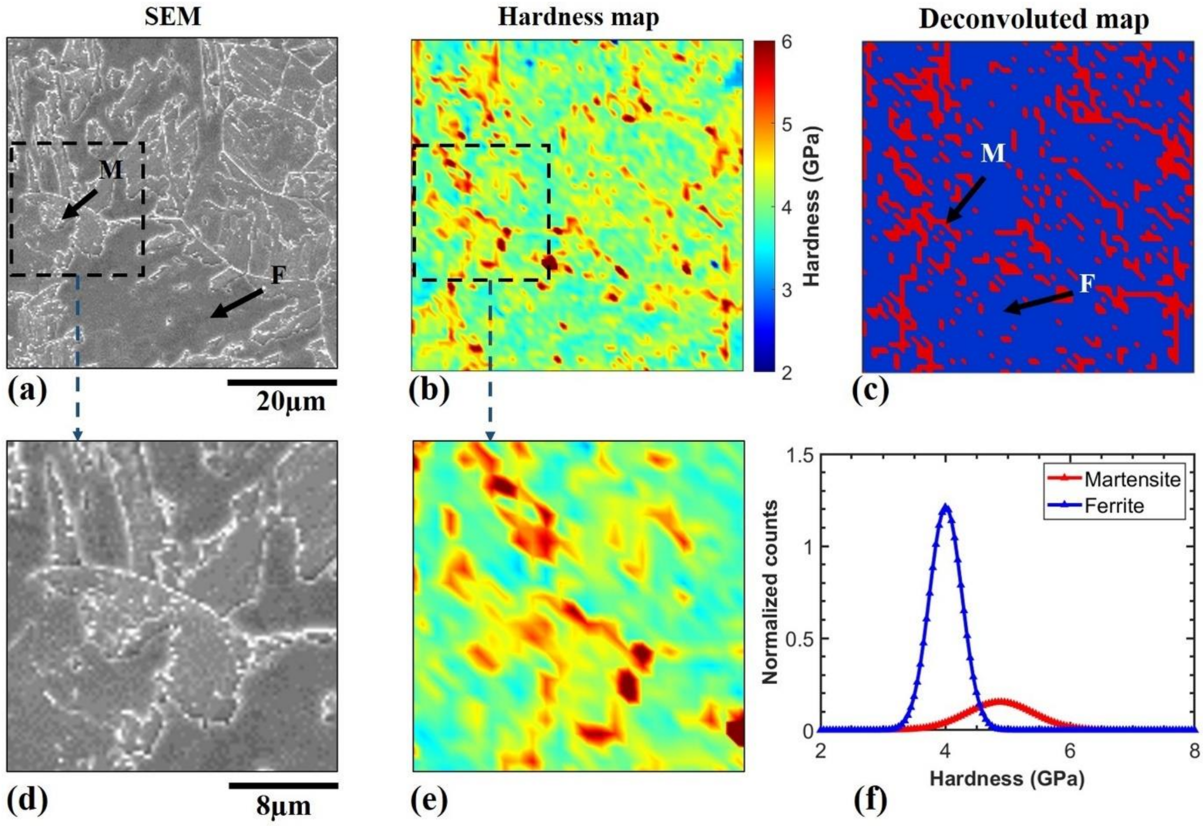

Figure 4-8: (a-d) SEM micrograph, the corresponding (b-e) hardness map, (c) mechanical phase map and (f) deconvoluted hardness distribution of FM.

4.4.2. Effect of coiling temperature on the microstructure and local mechanical properties

Considering the good agreement observed between microstructure and hardness at the micrometer length scale, and taking into account the validation of the deconvolution algorithm detailed in the preceding subsection, it is instructive to compare the hardness of individual constituents in response to varying processing conditions.

In Fig. 4-9, we present histograms showing the deconvoluted hardness data for bulk ferrite and the secondary phase/constituent. In the case of bulk ferrite (Fig. 4-9(a)), it is evident that FP and FB samples exhibit lower hardness values, measuring 3.3 GPa and 3.4 GPa, respectively, in contrast to FM, which demonstrates a notably higher hardness of 4 GPa. This difference in hardness can be attributed to a combination of factors, including the presence of finely distributed martensite, which can influence the hardness measurements, and the higher defect density generated during rapid cooling for martensite formation. To gain a deeper understanding of this phenomenon, it is valuable to consider prior research that has explored the impact of martensite on the surrounding soft ferrite matrix. Bourell and Rizk [29] have elucidated that the formation of martensite introduces localized strain in the adjacent ferrite, consequently diminishing the overall ductility of the composite material. In the context of dual phase steels, the cooling process from the austenitic phase to form bainite or martensite triggers a volumetric expansion. This expansion imposes strain on the newly formed ferrite, resulting in an enhancement of strength. This phenomenon has been quantitatively correlated with the volume fraction and size of martensite[29]. Applying the model proposed by Bourell and Rizk to our current study, we estimate that the additional strain induced on ferrite due to martensite formation is approximately 1%. However, this estimation alone cannot fully account for the measured difference in hardness, which amounts to nearly 0.7 GPa, between the ferrite in FP and FM samples. This observation suggests that the higher measured hardness in the ferrite of the FM sample could also be influenced by the fine and uniform distribution of martensite throughout the sample, impacting the hardness measurements itself, considering the measurement resolution of 1 µm. This rationale can be extended to the case of FB within the intermixed region, where the hardness of ferrite is elevated in proximity to bainite/carbides. It is important to note that this does not apply to FP, where a banded morphology is observed, and any increase in hardness due to the presence of the hard phase, if any, is confined to the bulk ferrite-pearlite boundary. Further insights into this aspect have been reported in a prior research work [22].

Another noteworthy aspect of this study is the difference in the distribution of ferrite. The area encompassed beneath the histograms, as illustrated in Fig. 4-9(a), serves as a relative measure of the area fraction occupied by bulk ferrite. This measurement aligns closely with the observations derived from the microstructure, particularly in the cases of FP and FM. However, it exhibits a significantly lower fraction for FB. This discrepancy arises from the fact that in the FB sample, a more substantial portion of ferrite is observed within the region intermixed with bainite.

In the context of the secondary phase/constituents, as depicted in Fig. 4-9(b), the ferrite-bainite mixture peak records the lowest value, at 4.4 GPa, followed by pearlite at 4.7 GPa, and martensite at 5 GPa. This variation can be rationalized by the distinct distributions of ferrite in the three cases. In the case of FB, the higher area fraction of the ferrite-bainite intermixed region results in a softer ferrite constituent affecting the measurement, consequently lowering the average hardness of the intermixed region. In contrast, the other two cases exhibit higher hardness, either due to the elevated carbon content in the form of cementite in FP or the presence of supersaturated carbon and increased defect density in FM.

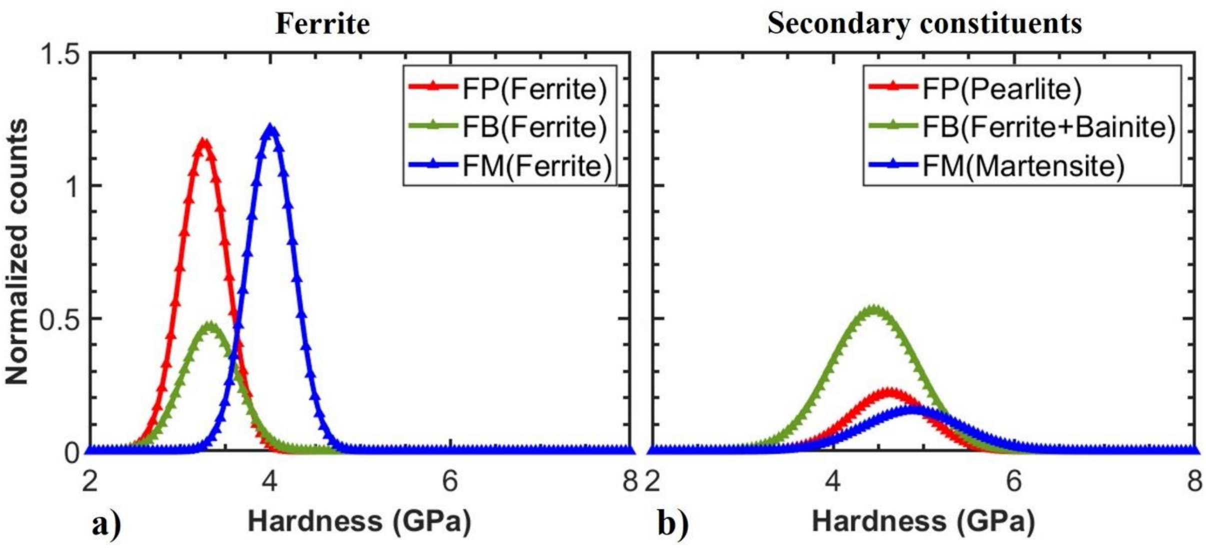

Figure 4-9: Comparison of hardness distribution of (a) ferrite and (b) secondary phase / constituents in FP, FB and FM.

4.5 Summary and conclusions

This chapter presents the effect of hot rolling followed by coiling on carbon distribution and thereby the local mechanical properties at micrometer length scale in a dual phase steel with composition close to DP600 steel and lays a foundation for correlative characterization of AHSS and other complex multiphase steels.

1. DP steels with three different microstructures (ferrite-pearlite, ferrite-bainite and ferrite-martensite) at a fixed carbon content were obtained by hot rolling followed by coiling at different temperatures.
2. As the cooling rate increases, and coiling temperature decreases, there is an observable diminution in microstructural attributes, such as nature of secondary phase/constituent (pearlite, bainite and martensite), grain size of ferrite, alongside a refinement of second-phase constituents. Electron Backscatter Diffraction (EBSD) analysis reveals a greater degree of misorientation in the ferritic matrix of ferrite-

martensite (FM) compared to both the ferrite-bainite (FB) and ferrite-pearlite (FP) as the coiling temperature decreases.

3. High speed nanoindentation mapping was used to measure the local variations in the hardness. Excellent correlation between the microstructure and the mechanical properties at the micrometer length scale was observed for all the samples.
4. The properties of the individual phases/constituents were obtained by deconvolution of the hardness maps and the effect of processing conditions on the distribution and properties of individual phases has been discussed. The area fractions of bulk ferrite are different in the three cases, whereas the hardness of bulk ferrite is similar in the case of FP and FB and higher in the case of FM. This is attributed to the fine distribution of martensite and the localized strain induced during martensite formation. In the case of the secondary phase/constituents, the ferrite-bainite mixture shows the lowest hardness compared to pearlite and martensite.
5. These results demonstrate the ability of nanoindentation mapping to capture the local variations in hardness at the length scale encountered in DP steels and opens the doors for correlative characterization and development of next generation AHSS and multiphase steels.

4.6 References

[1] S. Oktay, P.E. Di Nunzio, M.C. Cesile, K. Davut, M.K. Şeşen, Effect of Coiling Temperature on the Structure and Properties of Thermo-Mechanically Rolled S700Mc Steel, J. Min. Metall. Sect. B Metall. 58 (2022) 475–489. https://doi.org/10.2298/JMMB220304028O.

[2] J. Xue, Z. Zhao, C. Bin, X. Liu, H. Wu, H. Li, W. Xiong, Effects of rolling and coiling temperature on the microstructure and mechanical properties of hot-rolled high strength complex phase steel, Mater. Res. Express. 6 (2019). https://doi.org/10.1088/2053-1591/ab1404.

[3] S.J. Kim, C.G. Lee, T.H. Lee, S. Lee, Effects of coiling temperature on microstructure and mechanical properties of high-strength hot-rolled steel plates containing Cu, Cr and Ni, ISIJ Int. 40 (2000) 692–698. https://doi.org/10.2355/isijinternational.40.692.

[4] G.L. Wu, X.B. Liu, C.Y. Zhou, Effects of rolling and cooling process on mechanical properties and microstructure of 600 MPa microalloyed dual-phase steel produced by compact strip production, J. South. African Inst. Min. Metall. 116 (2016) 49–53. https://doi.org/10.17159/2411-9717/2016/v116n1a8.

[5] F. Peng, X. Gu, Y. Wang, Y. Xu, Y. Yu, Influence of coiling temperature on mechanical properties in hot rolling C-Mn-Si-Al steel, Procedia Manuf. 15 (2018) 52–58. https://doi.org/10.1016/j.promfg.2018.07.169.

[6] V.S.A. Challa, R.D.K. Misra, R. O’Malley, S.G. Jansto, The effect of coiling temperature on the mechanical properties of ultrahigh-strength 700 MPa grade processed via thin-slab casting, AISTech - Iron Steel Technol. Conf. Proc. 3 (2014) 2987–2997.

[7] Y. Zhao, X. Huang, B. Yu, X. Yuan, X. Liu, Effect of coiling temperature on microstructure, properties and resistance to fish-scaling of hot rolled enamel steel, Materials (Basel). 10 (2017). https://doi.org/10.3390/ma10091012.

[8] M.S. Rashid, Dual-phase steels, Automot. Steels Des. Metall. Process. Appl. (1981) 169–216. https://doi.org/10.1016/B978-0-08-100638-2.00007-9.

[9] R.A. Grange, Effect of microstructural banding in steel, Metall. Trans. 2 (1971) 417–426. https://doi.org/10.1007/BF02663328.

[10] C. Slater, B. Bandi, P. Dastur, C. Davis, Segregation Neutralised Steels: Microstructural Banding Elimination from Dual-Phase Steel Through Alloy Design Accounting for Inherent Segregation, Metall. Mater. Trans. A Phys. Metall. Mater. Sci. 53 (2022) 2286–2299. https://doi.org/10.1007/s11661-022-06674-6.

[11] F.G. Caballero, A. García-Junceda, C. Capdevila, C.G. De Andrés, Evolution of microstructural banding during the manufacturing process of dual phase steels, Mater. Trans. 47 (2006) 2269–2276. https://doi.org/10.2320/matertrans.47.2269.

[12] W. Thompson, P.R. Howell, Origin of Large Pearlite Nodules in a Hypoeutectoid Plate Steel, Mater. Sci. Technol. 8 (1992) 777–784.

[13] L.I. Zhuang, L. Wei, Study of microstructure and mechanical properties of hot-rolled ultra-high strength ferrite-bainite dual phase steel, Mater. Sci. Forum. 921 MSF (2018) 208–213. https://doi.org/10.4028/www.scientific.net/MSF.921.208.

[14] Y. Deng, H. Di, R.D.K. Misra, Microstructure–mechanical property relationship in hot-rolled high-Al-low-Si dual-phase steel, Ironmak. Steelmak. 46 (2019) 169–175. https://doi.org/10.1080/03019233.2017.1364034.

[15] P. Singh, S. Singh, S. Mewar, Processing and characterization of high strength dual-phase steel by two-step intercritical heat treatment process, Proc. Inst. Mech. Eng. Part E J. Process Mech. Eng. 233 (2019) 581–588. https://doi.org/10.1177/0954408918778645.

[16] C.H. Li, C.Y. Chen, S.P. Tsai, J.R. Yang, Microstructure characterization and strengthening behavior of dual precipitation particles in Cu–Ti microalloyed dual-phase steels, Elsevier Ltd, 2019. https://doi.org/10.1016/j.matdes.2019.107613.

[17] G. Béres, Z. Weltsch, Estimation of strength properties from microhardness results in dual phase steels with different martensite volume fraction, Period. Polytech. Transp. Eng. 47 (2019) 206–212. https://doi.org/10.3311/PPtr.12113.

[18] A.B. Cota, F.L.G. e Oliveira, A.L. da R. e Barbosa, C.A.M. Lacerda, F.G. da S. Araújo, Microstructure and mechanical properties of a microalloyed steel after thermal treatments, Mater. Res. 6 (2003) 117–121. https://doi.org/10.1590/s1516-14392003000200002.

[19] S. Sodjit, V. Uthaisangsuk, A micromechanical flow curve model for dual phase steels, J. Met. Mater. Miner. 22 (2012) 87–97. http://ojs.materialsconnex.com/index.php/jmmm/article/view/27.

[20] C. Dulucheanu, T.L. Severin, D.A. Cerlinca, L. Irimescu, Structures and Mechanical Properties of Some Dual-Phase Steels with Low Manganese Content, Metals (Basel). 12 (2022). https://doi.org/10.3390/met12020189.

[21] S. Janakiram, P.S. Phani, G. Ummethala, H.V. Jagdeesh, S.K. Malladi, J. Gautam, L.A.I. Kestens, Insights on early recovery kinetics in ferrite - pearlite cold rolled high strength sheet steels, Mater. Charact. 193 (2022). https://doi.org/10.1016/j.matchar.2022.112332.

[22] S. Janakiram, P.S. Phani, G. Ummethala, S.K. Malladi, J. Gautam, L.A.I. Kestens, New insights on recovery and early recrystallization of ferrite-pearlite banded cold rolled high strength steels by high speed nanoindentation mapping, Scr. Mater. 194 (2021) 113676. https://doi.org/10.1016/j.scriptamat.2020.113676.

[23] B. Vignesh, W.C. Oliver, G.S. Kumar, P.S. Phani, Critical assessment of high speed nanoindentation mapping technique and data deconvolution on thermal barrier coatings, Mater. Des. 181 (2019) 108084. https://doi.org/10.1016/j.matdes.2019.108084.

[24] J. Gautam, A. Miroux, J. Moerman, L. Kestens, TNR dependent hot rolling microstructure and texture development in c-Mn dual phase and HSLA steels, Defect Diffus. Forum. 391 (2019) 120–127. https://doi.org/10.4028/www.scientific.net/DDF.391.120.

[25] S. Janakiram, J.P. Gautam, A. Miroux, J. Moerman, L. Kestens, Microstructure and Texture Control in Cold Rolled High Strength Steels, Diffus. Found. 22 (2019) 84–93. https://doi.org/10.4028/www.scientific.net/df.22.84.

[26] W.C. Oliver, Measurement of hardness and elastic modulus by instrumented indentation: Advances in understanding and refinements to methodology, J. Mater. Res. Soc. 19 (2004) 20. https://doi.org/https://doi.org/10.1557/jmr.2004.19.1.3.

[27] W.C. Oliver, G.M. Pharr, An improved technique for determining hardness and elastic modulus using load and displacement sensing indentation experiments, J. Mater. Res. Soc. 7 (1992) 19. https://doi.org/http://dx.doi.org/10.1557/JMR.1992.1564.

[28] P. Sudharshan Phani, W.C. Oliver, A critical assessment of the effect of indentation spacing on the measurement of hardness and modulus using instrumented indentation testing, Mater. Des. 164 (2019) 107563. https://doi.org/10.1016/j.matdes.2018.107563.

[29] D.L. Bourell, A. Rizk, Influence of martensite transformation strain on the ductility of dual-phase steels, Acta Metall. 31 (1983) 609–617. https://doi.org/10.1016/0001-6160(83)90051-2.

Chapter 5 Effect of cold rolling on microstructure and mechanical properties of C-Mn Advanced High Strength Sheet steel

Advanced high-strength steels (AHSS) have wide variety of applications in various parts of car body due to their combination of good strength and ductility. In recent years significant efforts have been made to further enhance the mechanical properties of these steels by altering the thermomechanical processing (TMP). While a dual phase ferrite-martensite microstructure obtained after inter-critical annealing is the typical end result, several prior processing steps including hot rolling, coiling, cold rolling, etc have significant effect on the final microstructure. In this regard, we generate different dual phase microstructures with ferrite matrix along with pearlite, bainite and martensite for a DP600 grade sheet steel. The different microstructures are obtained by coiling at different temperatures subsequent to hot rolling which was discussed in the previous chapter. In this chapter, we focus on cold rolling after coiling. The microstructure and mechanical properties of these specimens were characterized by various tools such as optical, SEM, EBSD, Vickers hardness and high speed nanoindentation mapping. An assessment of the microstructure-property correlation at the micrometer length scale will be presented along with quantification of the local hardness of the matrix and second phase for different levels of cold rolling. The texture evolution during the cold rolling is also discussed. A discussion on the effect of second phase on the microstructure and hardness evolution will also be presented.

5.1 Introduction:

High strength and advanced high strength steel (AHSS) grades such as dual phase, complex phase transformation induced plasticity [1], and bainitic-martenistic steels [2] have been developed in response to the need to increase fuel efficiency by reducing the weight of vehicles and to reduce greenhouse gas emissions[3–5]. The primary requirements of AHSS are good ductility and formability in addition to high strength [1] with yield strength preferably greater than 750 MPa[6]. The aforementioned steel grades, however, comprise two or more microstructural components with varying degrees of strength. Such a microstructure causes localised strain and defect development along interphase boundaries or within any constituent, which affects the formability[7,8]. A single-phase ferrite microstructure is advantageous in this regard as it ensures homogeneous deformation during forming, ensuring good hole-expansion and stretch-formability characteristics[1]. However, it has limited strength It is well known that DP and TRIP steels provide a superb balance of mechanical qualities, including high strength and ductility which are significantly influenced by the second phase morphology, distribution, and area percentage of martensite [9–11]. Cold rolling increases the strength at the cost of ductility, which again depends on the nature of the second phase/constituent. The effect of initial microstructure with different second phase constituents like pearlite, bainite and martensite along with the ferrite matrix for a fixed carbon content has not been comprehensively investigated.

The microstructural and textural evolution of low carbon steels with a single ferrite phase following various cold reductions has been extensively studied[12–15]. The degree of deformation and defect density of the material increase with higher cold rolling reduction. In IF steels, homogeneous deformation enhances the development of texture[12,15,16]. Kernel Average Misorientation (KAM) derived from Electron Backscatter Diffraction (EBSD) is employed for the assessment of heterogeneity by examining strain localization [17,18]. The effect of misorientation on hardness in nickel-based superalloys was qualitatively studied by Shen et al. [19] using nanoindentation. However, the same relationship in different grades of high strength steels, such as DP steels, which have a composite ferrite microstructure with various secondary phase constituents (pearlite/bainite/martensite) after cold rolling, has not been well explored. The heterogeneous microstructure makes it difficult to understand how cold rolling affects the deformation mechanisms, microstructural and texture evolution, and mechanical properties of each phase. As we have shown in the previous chapter, the local mechanical property at the micrometer length scale can be measured by nanoindentation. This chapter investigates how the microstructure and the mechanical properties at this scale are related after cold rolling, using electron microscopy and nanoindentation[20].

5.2 Experimental procedure:

5.2.1 Material composition and phase fraction:

Dual phase steel with a composition close to DP600 is hot rolled and coiled as described earlier. The chemical composition and processing of hot rolled and coiled microstructures are discussed in chapter 4. Subsequently, aforementioned three different hot rolled specimens were cold rolled up to 2.4 mm and 1.2 mm thickness through 60% and 80% cold reduction. Mechanical polishing was carried out using SiC papers, followed by coarse alumina polishing and vibratory polishing with fine colloidal silica of 40 nm for 10 hr[21] for further characterization.

5.2.2 Microstructural and mechanical characterization

Microstructural characterization was carried out using optical microscope and scanning electron microscope (SEM). For the microstructural characterization the specimens were prepared by mechanical polishing and then etched with 2% Nital solution which contains 2% nitric acid and 98 ml of ethanol to reveal the microstructure. Additionally, EBSD analysis of these samples were carried out as described earlier.

On these well-polished samples, microhardness and nanoindentation measurements were performed[22], as per the procedure detailed in chapter 3. In order to obtain a deconvoluted map or mechanical phase map, the large hardness data set containing 3600 data points each obtained from mapping were deconvoluted using the k-means clustering algorithm, as described elsewhere[23,24].

In order to analyse the qualitative and quantitative correlations between microstructure and properties, as was mentioned in chapter 3, each phase's characteristics were deconvoluted. Nanoindentation maps and the corresponding SEM micrographs were used to assess the correlations. Ferrite and second phases from EBSD data were distinguished using IQ maps as mentioned in chapter 3. The KAM values of the ferrite and second phases were extracted and the corresponding distribution are used for further analysis.

5.3 Results:

5.3.1 Microstructure after hot rolling and cold rolling:

The microstructural evolution of hot rolled and coiled samples presented in chapter 4 are shown in Fig. 5-1(a), along with the cold rolled microstructures after 60% and 80% reduction, in Fig. 5-1(b) and 5-1(c), respectively. The microstructures show two constituents - ferrite (Dark Gray) and secondary constituents which are shown by the lighter shade. Fig 5-1(a) shows the hot rolled microstructures for FP, FB and FM, where the FP shows the banded type morphology and FB and FM show no banding and fine distribution of second phase. Fig. 5-1(b) shows the cold rolled microstructures after 60% of cold reduction. In FP case the ferrite and pearlite bands are elongated along the rolling direction with decrease in the band width. In FB and FM, the second phase constituents are fragmented and the grains are elongated. Fig. 5-1(c) shows the cold rolled microstructures after 80% reduction, leading to pronounced distortion and alignment of the ferrite phase in the direction of deformation. The pearlite bands also show elongation along the rolling direction, accompanied by finely fragmented cementite. Bainite undergoes substantial fragmentation and dispersion within the ferrite matrix. In the case of FP, the resulting microstructure is refined with elongated ferrite grains along the deformation direction, along with more fragmented and uniformly distributed martensite particles in the ferrite matrix.

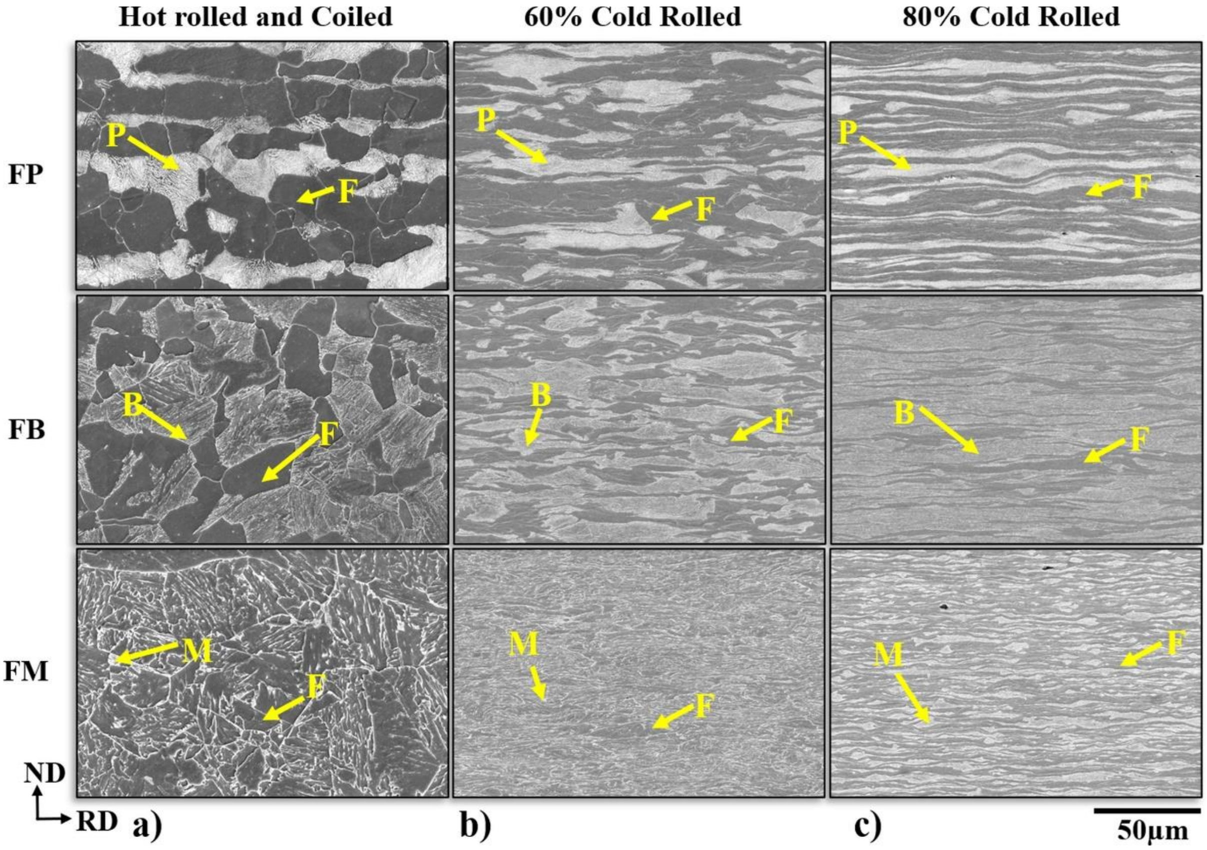

Figure 5-1: Etched SEM micrographs of FP, FB and FM after (a) hot rolling and coiling, (b), 60% cold rolling and (c) 80% cold rolling.

5.3.2 EBSD-KAM analysis of cold rolled samples:

The Kernel Average Misorientation (KAM) has been employed to analyse the dynamic evolution of misorientation and strain localization within ferrite and secondary constituents, including pearlite, bainite, and martensite, with varying degrees of deformation (i.e., 60% and 80% reduction). As shown in Fig. 5-2, the KAM map is utilized to quantify the average misorientation of data points in relation to their fifth nearest neighbours, with a threshold set at a maximum misorientation of 5°. The color-coded representation denotes varying degrees of misorientation in the microstructure, where the color blue mostly signifies a strain-free region with misorientations less than 1°, green ranges from 1-2°, yellow 2-3°, orange 3-4°, and red ranges from 4-5°. It is noteworthy that higher KAM values correspond to microstructures exhibiting elevated levels of defects and lattice distortion [25]. In the KAM map for FP, ferrite shows lower misorientation whereas the second phase constituents show higher misorientations in hot rolled as well as in cold rolled state (60% and 80%). Also, the misorientation increases with increasing extent of cold rolling for all the samples. Furthermore, the disorientations are higher in the case of FM compared to the other samples.

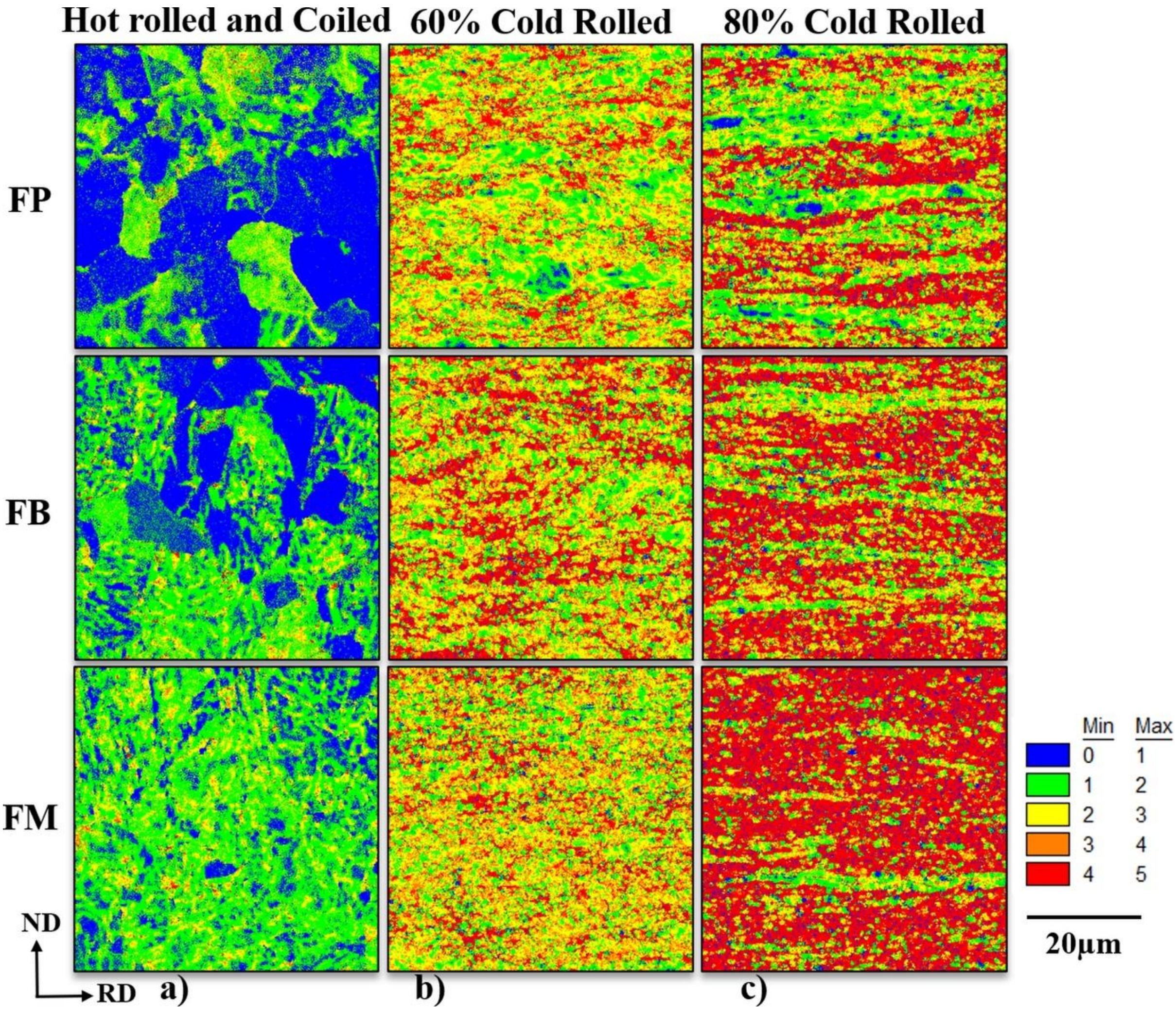

Figure 5-2: KAM maps of FP, FB and FM after (a) hot rolling and coiling, (b), 60% cold rolling and (c) 80s% cold rolling.

5.3.3 KAM distribution of ferrite and second phases:

The partitioning of ferrite and secondary phase constituents was carried out using Electron Backscatter Diffraction (EBSD) IQ maps, with subsequent extraction of Kernel Average Misorientation (KAM) values for each constituent. In this section we present the changes in misorientation across samples for the individual constituents. The partitioning of individual phases/constituents from EBSD (IQ based) has been discussed in chapter 3.

The KAM histograms after partitioning for all the samples, including hot-rolled and coiled samples (representing 0% cold rolling), as well as samples subsequently subjected to 60% and 80% cold rolling are shown in Fig. 5-3. In the case of ferrite in all the samples (FP, FB and FM), as illustrated in Fig. 5-3(a), the misorientation increases with cold rolling as expected. A slight increase in misorientation for 80% compared to 60% is also observed. These results indicate that 60 % cold rolling increases the defect density considerably whereas further cold rolling only has a marginal effect. Similar trend is observed in the case of the secondary constituents across all the samples as shown in Fig. 5-3(b).

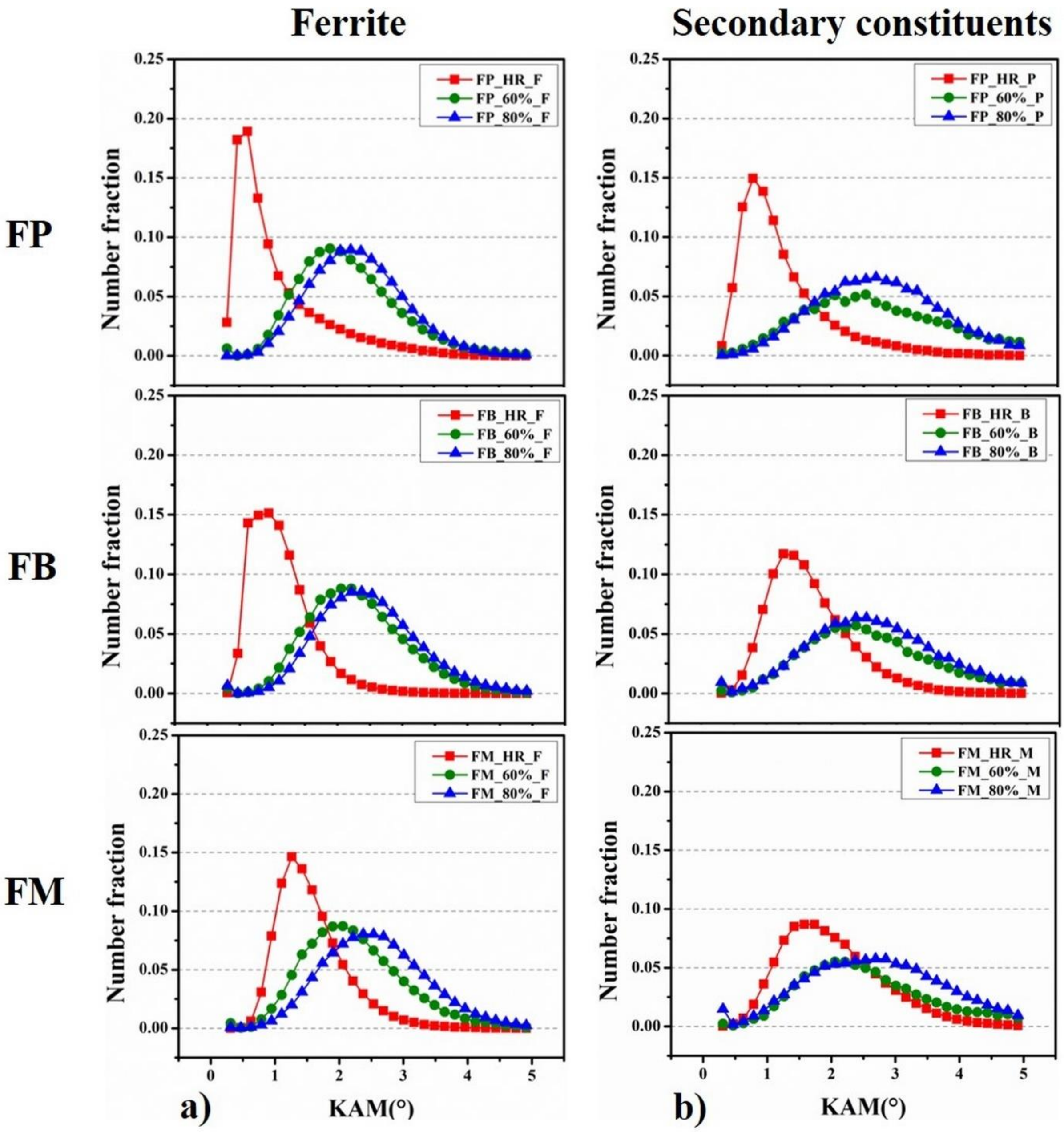

Figure 5-3: Kernel Average Misorientation (KAM) distribution for (a) ferrite and (b) secondary constituents following hot rolling and coiling (i.e., 0%), as well as after 60% and 80% cold rolling for FP, FB and FM.

5.3.4 Vickers microhardness:

In Fig. 5-4, the microhardness data, obtained through Vickers indentation, is presented for samples subjected to hot rolling and coiling (representing 0% cold rolling), and cold rolling reductions of 60% and 80%. The microhardness exhibits an increasing trend starting with FP (ferrite pearlite), followed by FB (ferrite bainite), and ultimately FM (ferrite martensite). This trend can be attributed to the higher hardness of the martensitic structure formed via rapid cooling, which can refine the ferrite microstructure and enhance local matrix strength due to the presence of a higher dislocation density. As the degree of cold rolling increases from 60% to 80%, the plastic strain imparted to the samples increases, leading to a greater accumulation of dislocations within the three samples. Consequently, the hardness values increase from FP to FM. It may be noted that due to the relatively larger size of the hardness impressions in comparison to the microstructural length scale, detailed information of the deformation at the microstructural level is limited. To gain deeper insights at smaller length scales, nanoindentation testing has been employed[22].

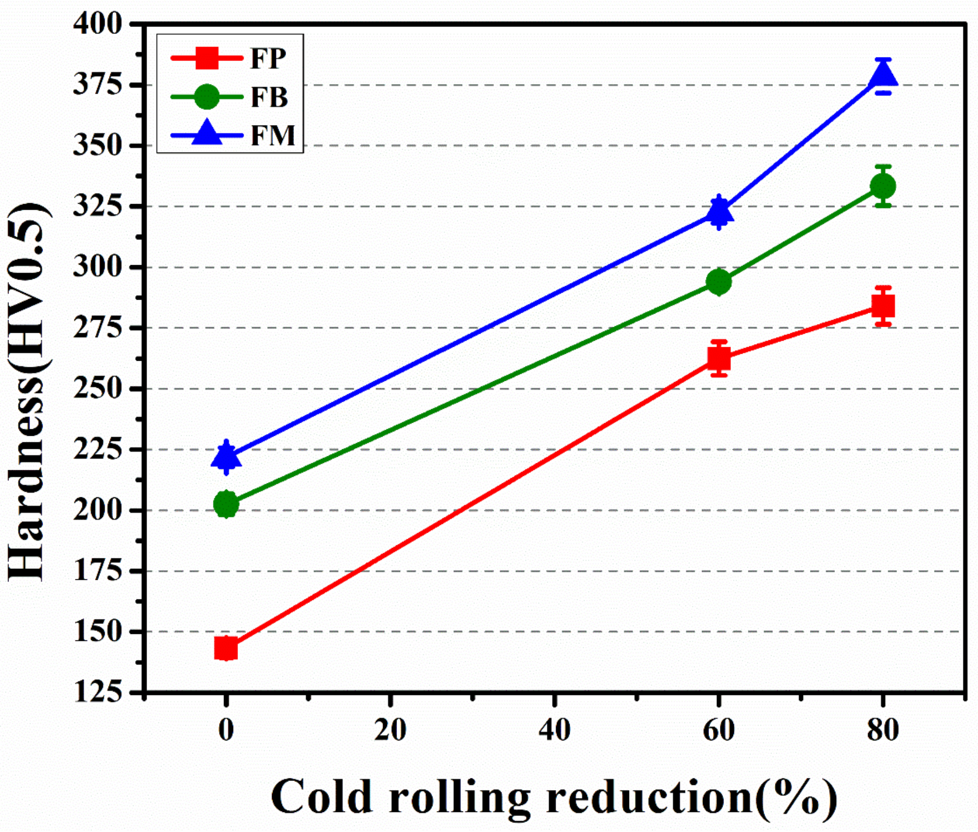

Figure 5-4: Micro Vickers hardness as a function of cold rolling reduction for FP, FB and FM.

5.3.5 Nanoindentation mapping:

Representative high speed nanoindentation maps are shown in Fig. 5-5 for all the three samples. The hardness map of FP in hot rolled and coiled condition clearly reflects the banded nature of the microstructure, with the bulk ferrite being softer than pearlite as discussed in the previous chapter. After cold rolling to 60 and 80% reduction, the hardness map shows elongated grains of ferrite and pearlite along the rolling direction. It also shows that the hardness increases in both the constituents. In the case of FB, the bulk ferrite regions are similarly lower in hardness compared to the regions with ferrite intermixed with bainite / carbides which show higher hardness and increased heterogeneity in the hot rolled state. With cold rolling, the ferrite and bainitic region grains are elongated along the rolling direction and the hardness increases in all the regions, especially after 80% cold rolling. Finally, in the case of hot rolled and coiled FM, the ferrite regions are relatively harder compared to FB and FP, and locally high hardness regions corresponding to martensite can be observed. This trend continues with cold rolling and results in a band-like morphology in hardness after 80% cold rolling. Also, higher hardness is observed in both ferrite and the martensite regions which further increases upon cold rolling. In spite of the nominal composition being identical in all the three cases, the hardness maps show significant variations which are similar to those observed in the KAM maps shown in Fig. 5-3. It may be noted that clear distinction between bulk ferrite and second phase constituents in hot rolled and coiled becomes less obvious after cold rolling.

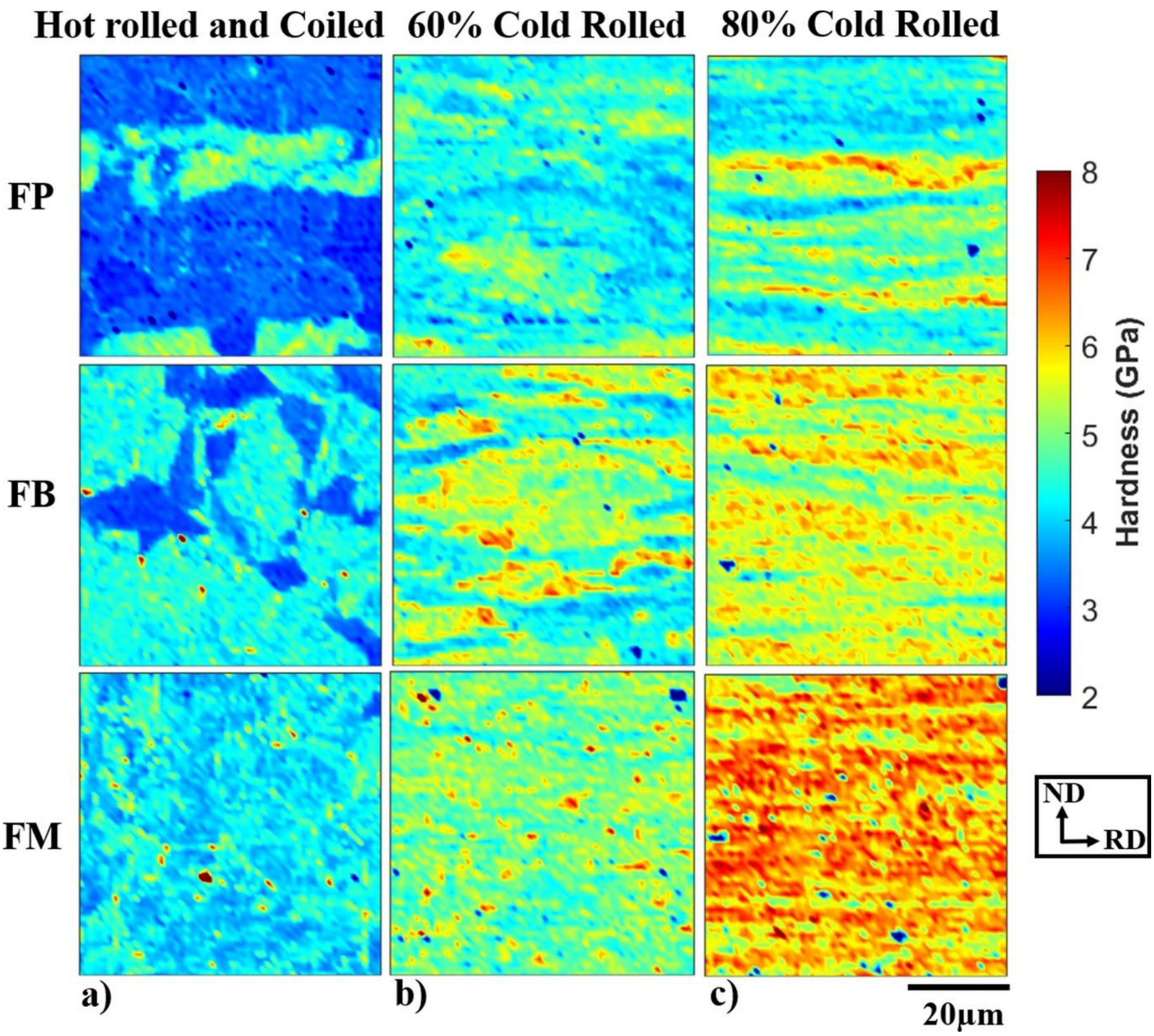

Figure 5-5: Nanoindentation hardness maps of FP, FB and FM after (a) hot rolling and coiling, (b), 60% cold rolling and (c) 80s% cold rolling.

5.3.6 Hardness distribution:

The quantification of hardness maps shown in the previous sub-section is presented here by way of histograms which enables easy comparison across samples. The histograms after hot rolling and coiling and subsequent cold rolling are shown in Fig. 5-6 for FP, FB and FM. In the case of the FP (Fig. 5-6a red color), it is notable that under hot-rolled and coiled conditions, a bimodal distribution is observed. These peaks correspond to the hardness values of the ferrite and pearlite phases. Ferrite has a lower hardness, while pearlite has a higher hardness. Upon cold rolling to 60% and 80% a single broad distribution is observed and its position shifts towards higher hardness values, indicating that the hardness of both ferrite and pearlite increases, as depicted by the olive green and blue-colored regions in Fig. 5-6(a). The observation of a single broad peak can be attributed to the greater extent of increase in hardness in ferrite compared to pearlite. In the case of FB shown in Fig. 5-6(b), the red peak, representing the hardness of the hot-rolled and coiled FB (ferrite bainite) sample, shows two distinct peaks. Similar to the case of FP, these peaks correspond to the hardness values of the ferrite (lower hardness) and the bainitic region, inclusive of ferrite and bainite/carbides (higher hardness). As the sample undergoes 60% and 80% cold reduction, the hardness peaks shift towards higher values, demonstrating an increase in hardness, as indicated by the olive green and blue-colored regions. After 80% cold rolling a single broad peak is observed much like FP. In the case of FM shown in Fig. 5-6(c) a single peak is observed in all cases. With the peak clearly shifting to higher hardness with increasing amount of cold rolling. It is worth noting that the presence of martensite, with a finer length scale and distributed throughout the sample, results in a single broad peak in the case of FM. The histograms shown in this plot for all the samples are for the entire mapped region that includes both the constituents. For a more comprehensive understanding of the evolution of hardness with processing, it is essential to investigate variations within each constituent separately. This can be achieved through the deconvolution of the hardness maps, which will be discussed in the next section.

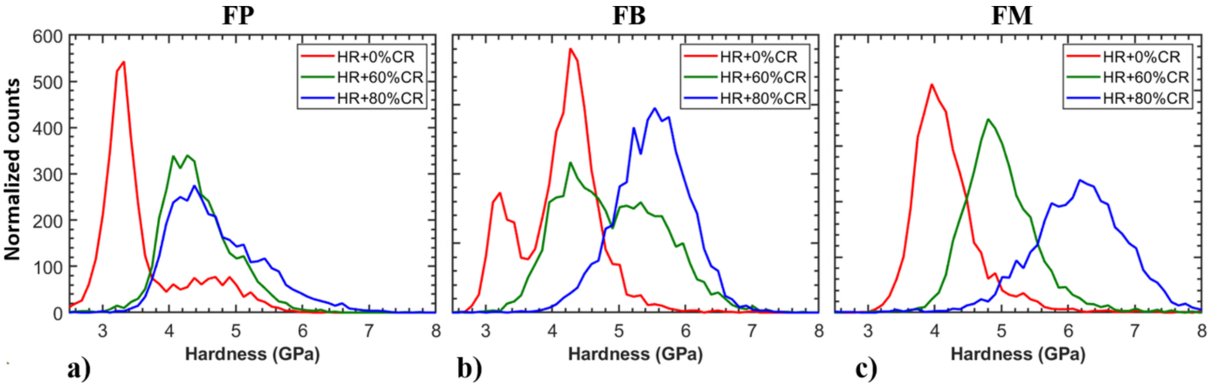

Figure 5-6: The effect of processing conditions such as hot rolling and coiling, cold rolling for different initial microstructures on hardness of (a) FP, (b) FB and (c) FM.

5.4. Discussion:

This section will cover two distinct topics: the analysis of microstructure and mechanical properties at the micrometer length scale[26], and a deeper exploration of how individual phases/constituents (ferrite, pearlite, bainite, and martensite) influence the relationship between structure and properties during cold rolling.

The preceding section has demonstrated noticeable localized variations in microstructure and mechanical properties, primarily stemming from disparities in processing conditions. These variations are intricately tied to the formation, morphology, distribution, and ensuing mechanical characteristics of constituent phases, and are significantly influenced by the critical initiation temperature and the cooling rate during the transformation from austenite to pearlite, bainite, and martensite. Distinct microstructural features and, consequently, mechanical properties[26] arise from differences in carbon distribution throughout these transformations. Following the hot rolling and coiling processes, samples undergo cold rolling deformation at levels of 60% and 80%, leading to plain strain deformation in the material, thereby impacting both microstructure and mechanical properties.

5.4.1 Assessment of microstructure and mechanical property correlation at the micrometer length scale in Ferrite-Pearlite (FP):

In Fig. 5-7, a comparison of microstructure and mechanical properties is shown in the case of FP, through scanning electron microscopy (SEM) and nanoindentation mapping. It is evident that during the initial stages, involving hot rolling and coiling (with 0% cold rolling), a banded morphology apparent in both the ferrite and pearlite. Subsequent cold rolling is found to result in grain elongation along the rolling direction, as shown in Fig. 5-7. This can be attributed to the accommodation of plastic strain within the material, which imparts a significant level of strain in both ferrite and pearlite, which, in turn, has an observable impact on the mechanical properties. This effect is evident in the Vickers hardness measurements presented earlier, where an increase in cold reduction leads to a corresponding increase in hardness. This increase in micro hardness reflects the composite hardness of both the constituents which can be deconvoluted from nanoindentation measurements. These nanoindentation hardness measurements shown in the figure can provide a clear differentiation in hardness between the ferrite and pearlite regions from the deconvoluted maps. This map shows the hardness data classified into two distinct bins, where the blue color signifies ferrite, and the red color represents pearlite. The deconvoluted map demonstrates a strong agreement with the SEM micrograph, clearly capturing the contrast differences between the two constituents. The hardness histogram obtained from the deconvoluted data enables a direct quantitative comparison of the hardness of the constituents. It may be observed that as cold reduction levels increase, the peaks associated with ferrite and pearlite undergo a rightward shift. This shift signifies that with greater degrees of rolling reduction, both ferrite and pearlite constituents exhibit increased hardness, which can be attributed to the accommodation of strain within the material. In summary, it can be concluded that a good correlation between microstructure, hardness map and the deconvolution map at the micrometer length scale is observed during cold rolling. A detailed analysis of the evolution of hardness of each constituent with cold rolling for all the samples will be presented in section 5.4.4.

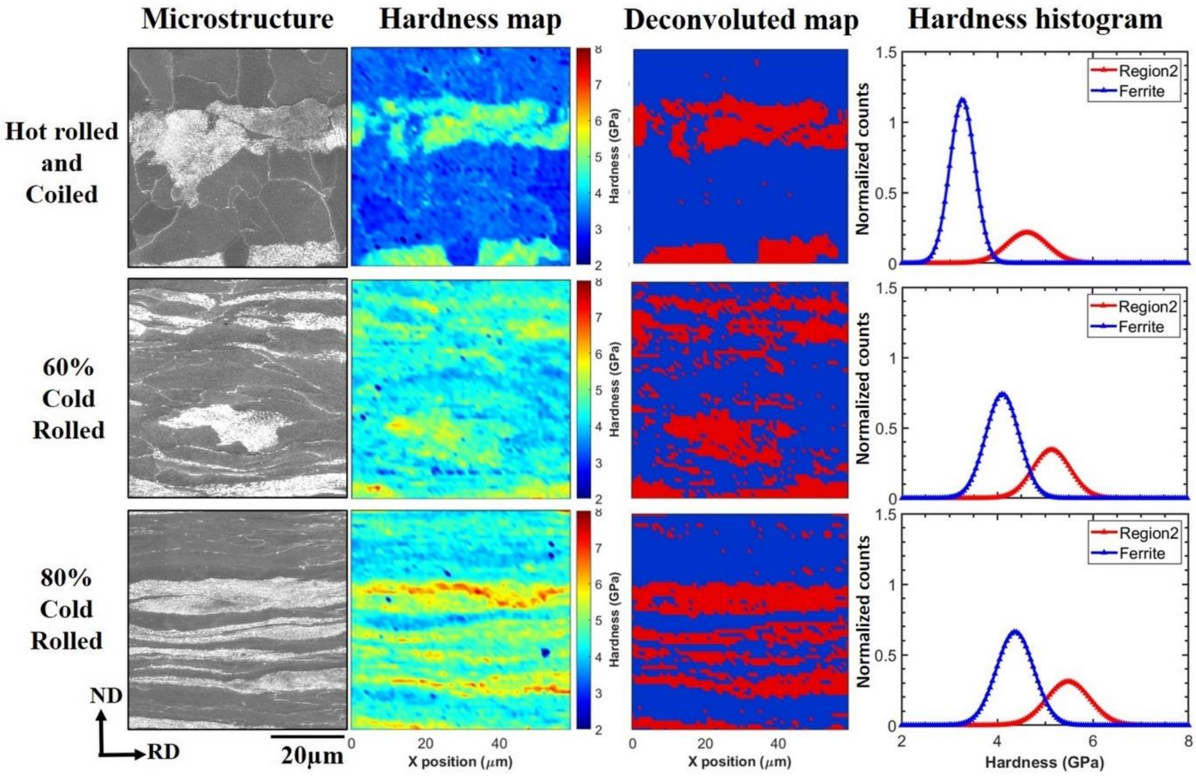

Figure 5-7: SEM micrograph along with corresponding hardness map and deconvoluted map with two bins and the hardness histogram of FP after hot rolling and coiling (0% cold rolled), and subsequent 60% and 80% cold rolling.

5.4.2 Assessment of microstructure and mechanical property correlation at the micrometer length scale in Ferrite-Bainite (FB):

In Fig. 5-8, microstructure of hot-rolled and coiled specimens, as well as cold-rolled specimens are shown along with the corresponding nanoindentation maps for the case of ferrite-bainite (FB). The microstructure after hot rolling and coiling shows bulk ferrite and bainitic regions. The bainitic region exhibits a mixture of bainitic ferrite and bainite, featuring finely dispersed carbides. Cold rolling induces elongation of grains along the rolling direction, leading to progressive refinement and fragmentation of equiaxed grains. With increasing rolling reduction, refinement in the microstructural length scale is observed. Examining the hardness maps in Fig. 5-8, hot-rolled and coiled specimens (representing 0% cold rolling) reveal bulk ferrite characterized by lower hardness, depicted in blue on the hardness map. Additionally, the bainitic region, featuring bainitic ferrite and bainite, exhibits a predominantly cyan color with localized regions with higher hardness, both of which are higher compared to bulk ferrite. The deconvoluted map, generated through a k-means clustering algorithm based on the hardness map, shows good agreement with the SEM micrograph. The hardness histogram obtained after deconvolution shows the corresponding distribution of ferrite and bainite, revealing lower hardness in bulk ferrite and higher hardness in the bainitic region. The rightward shift in the peaks of both the constituents with cold rolling can be observed as expected.

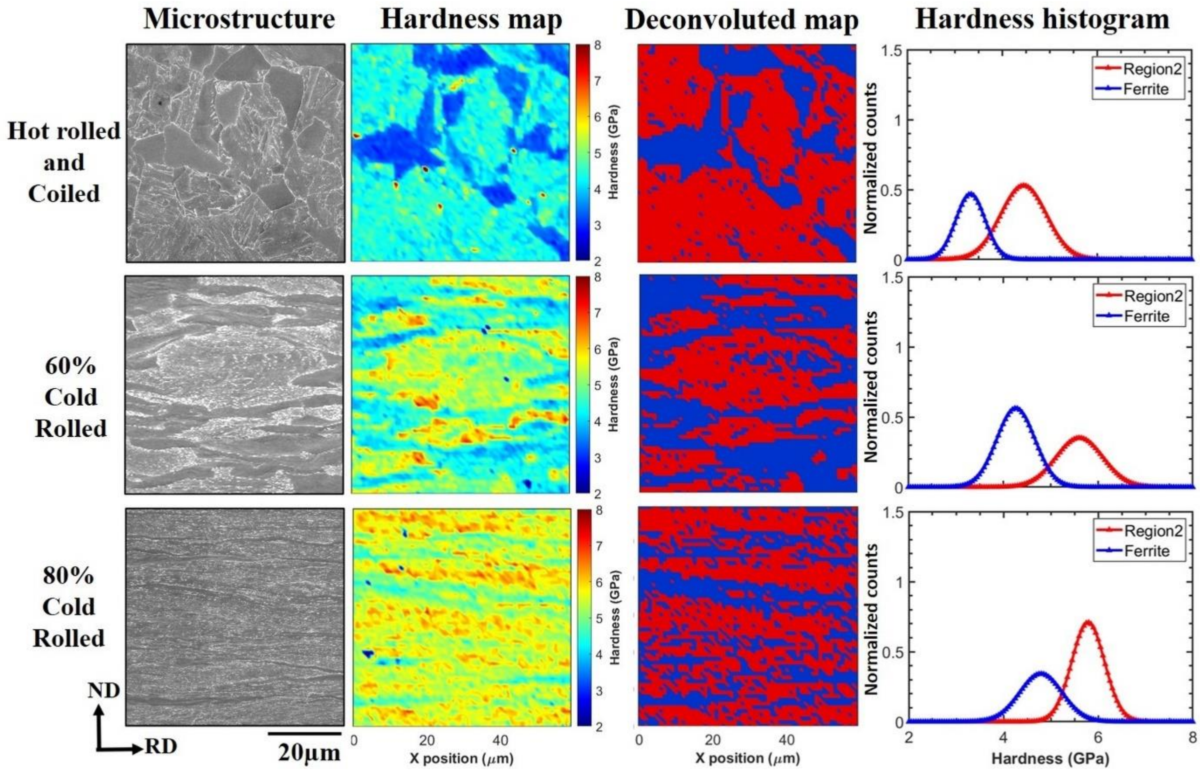

Figure 5-8: SEM micrograph along with corresponding hardness map and deconvoluted map with two bins and the hardness histogram of FB after hot rolling and coiling (0% cold rolled), and subsequent 60% and 80% cold rolling.

5.4.3 Assessment of microstructure and mechanical property correlation at the micrometer length scale in Ferrite-Martensite (FM):

In Fig. 5-9, microstructure of hot-rolled and coiled specimens, as well as cold-rolled specimens, are shown along with the corresponding nanoindentation maps for the case of ferrite-martensite (FM). The hot-rolled and coiled samples (0% cold rolling) reveal a finely dispersed distribution of martensite within the ferrite region and along grain boundaries. The hardness map distinctly captures the high hardness of martensite, denoted in red, and the cyan-colored ferrite, indicative of elevated hardness resulting from a rapid cooling rate and the fine distribution of martensite throughout the ferrite region. In the case of cold-rolled samples at 60% and 80%, the microstructure shows elongated grains along the rolling direction, attributed to deformation effects. The hardness map illustrates increased hardness in the 80% cold-rolled specimen, attributed to the higher dislocation density. The martensite structure itself results in higher hardness and the further cold rolling amplifies this effect, contributing to the observed higher hardness. The deconvoluted map shows the martensite in red and the ferrite in blue. The hardness histogram obtained from the deconvoluted data provides a quantitative estimate of the hardness of ferrite and martensite. The hardness histogram systematically depicts an increase in hardness for both ferrite and martensite phases with an increasing cold rolling reduction, underscoring the influence of deformation on the mechanical properties of the material. It may be noted that the given the fine length scale of martensite, its hardness may be influenced by the surrounding ferrite and with increase in cold rolling it can result in an apparent increase in hardness of martensite.

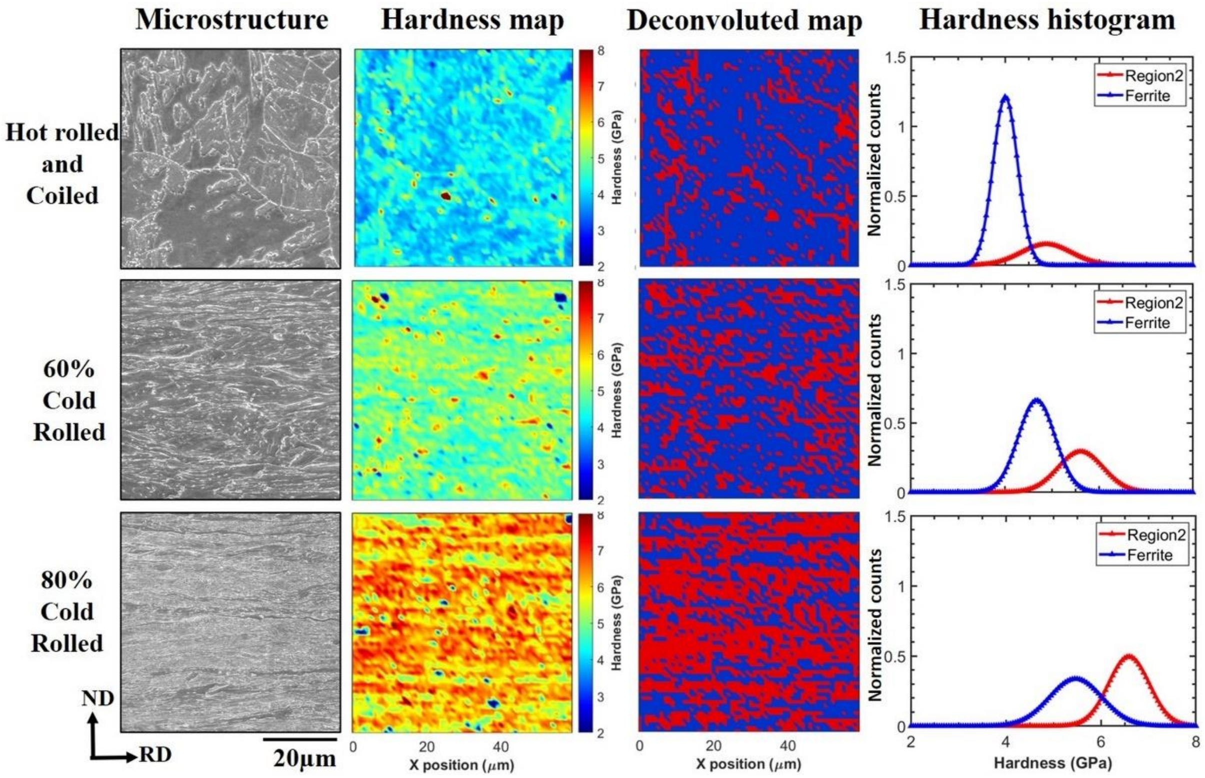

Figure 5-9: SEM micrograph along with corresponding hardness map and deconvoluted map with two bins and the hardness histogram of FM after hot rolling and coiling (0% cold rolled), and subsequent 60% and 80% cold rolling.

5.4.4 Comparison of properties of individual constituents

In this section, the hardness of the individual constituents presented in the previous section will be analysed as a function of the extent of cold rolling and compared to that of hot rolling as well. Fig. 5-10 shows the individual hardness histograms of ferrite and the secondary constituents of FP, FB and FM. In the color scheme, red represents hot-rolled and coiled samples, olive green represents 60% cold-rolled samples, and blue represents 80% cold-rolled samples. Fig. 5-10(a) shows hardness histograms of ferrite in FP, FB, and FM, while Fig. 5-10(b) shows hardness histograms of secondary constituents in FP, FB, and FM. In FP, the ferrite phase and second-phase constituents exhibit low hardness in the hot-rolled and coiled condition. A discernible increase in both phases is observed with cold rolling, indicative of deformation-induced hardness increases due to work hardening. Similar trends are observed in FB and FM, where both ferrite and second-phase constituents exhibit a rightward shift (higher hardness) in hardness peaks with increasing cold rolling reduction. Notably, FM exhibits a more pronounced peak shift compared to FB and FP. The increased hardness in FM is attributed to its formation at lower coiling temperatures, coupled with a higher cooling rate, resulting in a structure with increased defect density. Cold rolling further induces strain, leading to a higher dislocation density in the material. In FB, the bulk ferrite shows lower hardness, while the bainitic region, characterized by a mixture of ferrite, bainite, and fine carbides, shows higher hardness as expected. In FP, lower hardness is observed in the ferrite and pearlite region compared to FB and FM. This is attributed to the equiaxed grain structure and the eutectoid mixture of ferrite and cementite formed at higher coiling temperatures with a lower cooling rate.

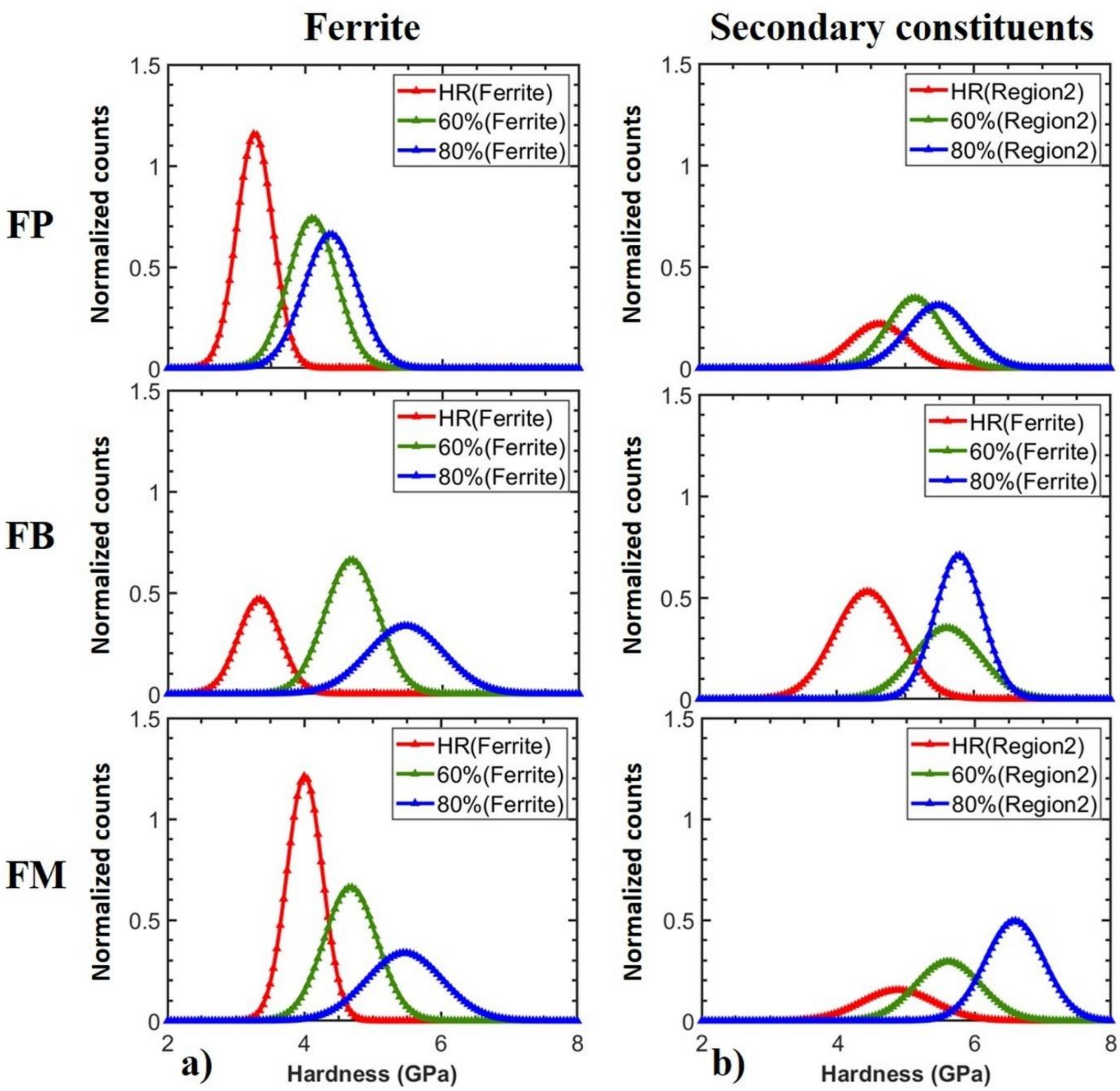

Figure 5-10: Deconvoluted hardness histograms of (a) ferrite and (b) secondary constituents of FP, FB and FM.

5.4.5 Texture analysis:

Fig. 5-11 illustrates the optimal positioning of the most significant BCC texture component within the ϕ2 = 45° section of Euler space. Crystallographic texture denotes the favoured alignment of crystalline grains in a polycrystalline material. An ideal body-cantered cubic (BCC) texture refers to a distinct arrangement of crystallographic orientations within a material of BCC structure. This texture is visually represented through a pole figure, a two-dimensional plot showcasing the distribution of crystallographic directions in the material. Essentially, a pole figure acts as a graphical representation of the preferred crystallographic orientations in a material, often depicted in a stereographic projection where each point corresponds to a specific crystallographic direction. For instance, in BCC metals like alpha iron, texture analysis frequently focuses on the (110) planes. The intensity of peaks in the pole figure indicates the prevalence of grains oriented in particular directions, with higher intensities reflecting a greater proportion of such grains.

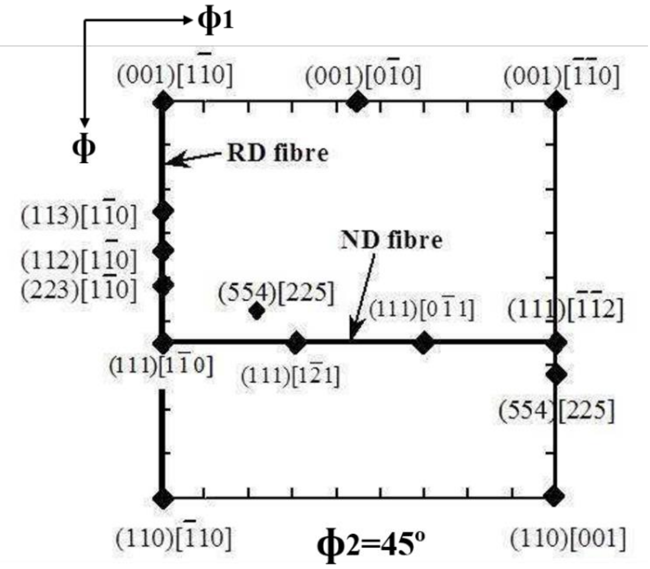

Figure 5-11: Ideal positions of the most important BCC texture components in the $\phi 2$ =45° section of Euler space[27].

Fig. 5-12 shows the ODFs of the samples with different initial microstructures (FP, FB, and FM) after hot rolling and cold rolling to 60% and 80% reduction. The initial microstructures after hot rolling show a random texture, as seen in Fig. 5-12(a). Cold rolling to 60% reduction induced both RD and ND fibre texture components in all the microstructures, as shown in Fig. 5-12(b). However, cold rolling to 80% reduction resulted in different texture behaviours for different microstructures. The FP microstructure maintained the RD-ND fibre texture components, while the FB/FM microstructures showed only the RD fibre texture components and lost the ND fibre texture components. These results indicate that the initial microstructure and the rolling reduction affect the texture evolution. The detailed changes in the texture components are discussed below.

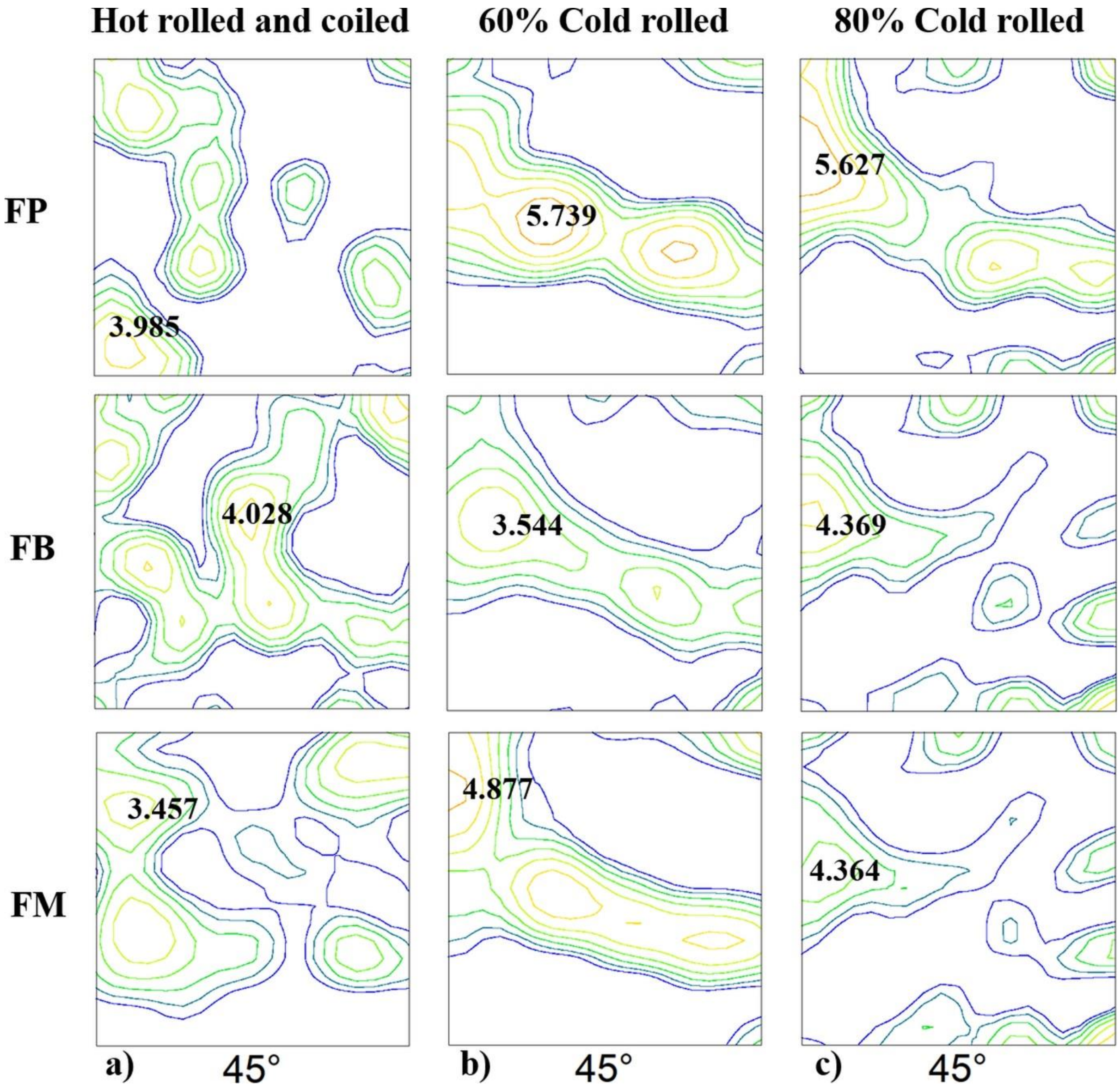

Figure 5-12: ODF plots after (a) hot rolling and coiling (0% cold rolled) (b) 60% cold rolling and (c) 80% cold rolling.

As shown in Fig. 5-13(a) the FP microstructure had a random texture after hot rolling, with the highest texture intensity on the RD fibre at the (115) [1-10] component (2.9x RI) and on the ND fibre at the (111) [1-21] component (2.9x RI). Some other components, such as rotated GOSS (3.7x RI) and rotated cube (2.8x RI), were also observed. Cold rolling to 60%

reduction enhanced both the RD and ND fibre texture components. On the RD fibre, the (115) [1-10] component rotated toward the stable (225) [1-10] component and increased its intensity to 4.5x RI. On the ND fibre, the (111) [1-21] and (111) [0-11] components strengthened with 4.6x RI. The rotated cube component remained at 2.8x RI after cold rolling to 60%. Further cold rolling to 80% reduction increased the intensity of the (225) [1-10] component to 5.6x RI on the RD fibre. The ND fibre texture weakened at the (111) [0-11] component (3.6x RI) and showed the presence of the (554) [-2-25] component (2.9x RI). The rotated cube component increased its intensity to 3.7x RI after cold rolling to 80%.

In the case of FB shown in Fig. 5-13(b), a random texture after hot rolling, with the highest texture intensity on the RD fibre at the (115) [1-10] component (2.9x RI) was observed. The ND fibre components deviated slightly from the ideal orientation. Other components, such as rotated GOSS (1.8x RI) and rotated cube (3.2x RI), were also observed. Cold rolling to 60% reduction induced both the RD and ND fibre texture components. On the RD fibre, the (115) [1-10] component rotated toward the stable (112) [1-10] component and increased its intensity to 2.5x RI. Some other orientations parallel to the RD fibre components were also detected with 3.5x RI. On the ND fibre, the (111) [0-11] component strengthened with 2.8x RI. The rotated cube component decreased its intensity to 1.8x RI after cold rolling to 60%. Further cold rolling to 80% reduction increased the intensity of the (112) [1-10] component to 3.7x RI on the RD fibre. The ND fibre texture weakened at the (111) [0-11] component (1.7x RI) and showed the presence of the (554) [-2-25] component (2.6x RI). The rotated cube component increased its intensity to 2.7x RI after cold rolling to 80%.

In the case of FM shown in Fig. 5-13(c), a random texture after hot rolling, with the highest texture intensity on the RD fibre at the (115) [1-10] component (2.7x RI) and on the ND fibre at the (111) [2-31] component (2.9x RI) was observed. Other components such as rotated cube (1.9x RI), were also observed. Cold rolling to 60% reduction induced both the RD and

ND fibre texture components. On the RD fibre, the (115) [1-10] component increased its intensity to 4.9x RI and the (445) [4-94] component parallel to the RD fibre appeared with 4.5x RI. On the ND fibre, the (111) [1-21] component strengthened with 3.2x RI. The rotated cube component increased its intensity to 3.8x RI after cold rolling to 60%. Further cold rolling to 80% reduction resulted in different texture behaviours on the RD and ND fibres. On the RD fibre, the (335) [1-10] component showed up with 2.3x RI. On the ND fibre, the (111) [0-11] component weakened with 1.4x RI and the (554) [-2-25] component was present with 2.2x RI. The rotated cube component decreased its intensity to 2.1x RI after cold rolling to 80%.

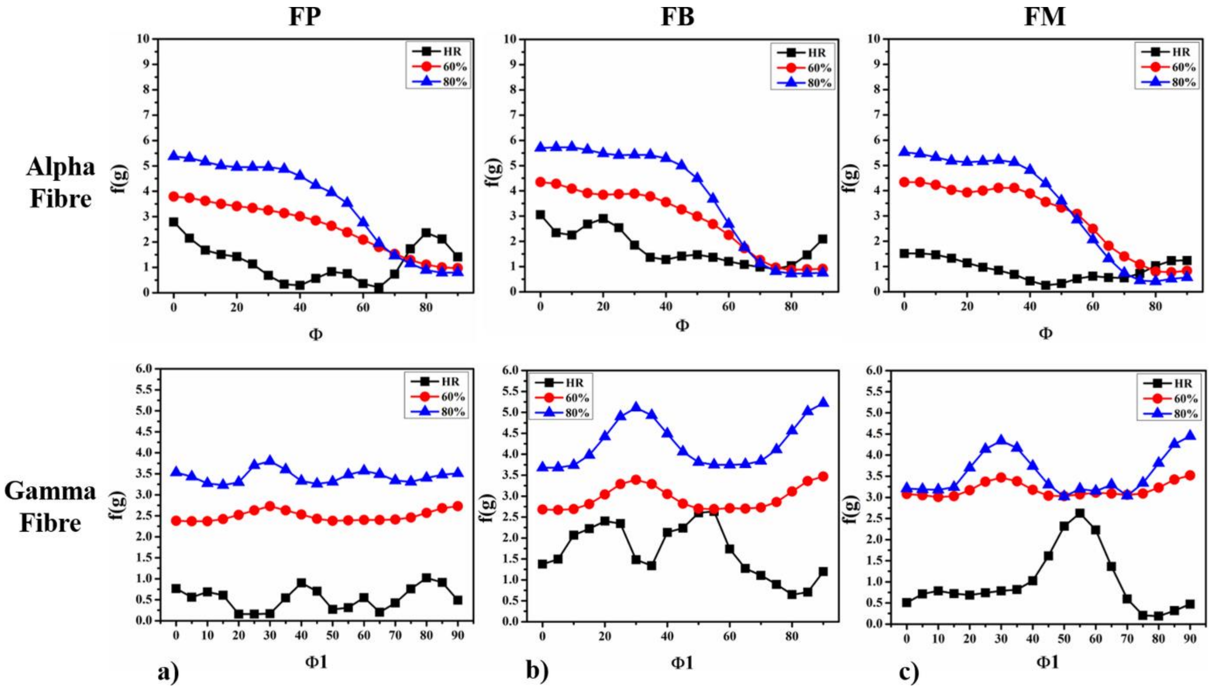

Figure 5-13: Alpha fibre and gamma fibre of hot rolled and coiled, 60% and 80% cold rolled samples of (a) FP, (b) FB and (c) FM.

5.5 Summary and conclusions:

In this chapter, the effect of cold rolling subsequent to hot rolling and coiling on the microstructure, texture and mechanical properties is presented. The findings establish a groundwork for correlative characterization methodologies applicable to Advanced High-Strength Steels (AHSS) and other intricate multiphase steel alloys.

1. Specimens with similar nominal carbon content but different microstructures, viz., ferrite-pearlite (FP), ferrite-bainite (FB) and ferrite-martensite (FM), obtained by hot rolling followed by coiling at different temperatures were subjected to different extents of cold rolling (60 % and 80 %).

2. High misorientation was observed in 80% cold rolled samples, followed by 60% cold rolled samples, and low misorientation is seen in hot rolled and coiled samples, based on the kernel average misorientation.

3. Similar trend was observed in Vickers micro hardness wherein higher hardness is observed in 80% cold rolled samples, followed by 60% cold rolled samples, and low hardness in hot rolled and coiled samples due to lower extent of work hardening.

4. Nanoindentation mapping was used to obtain the variation in the hardness of ferrite matrix and the corresponding second phase / constituent (pearlite/bainite/martensite) as a function of extent of cold rolling.

5. Excellent correlation between microstructure and mechanical properties was observed at the micrometer length scale for all the cases.

6. With increasing amount of cold work, the hardness of the ferrite matrix phase increased, and the hardness of ferrite after cold rolling shows a dependence on the second phase/constituent clearly indicating the role of the second phase in the deformation.

7. In the case of 60% cold rolling reduction, the strengthening of fibers aligned with the rolling direction (RD) and normal direction (ND) is observed for all the samples as

the transition is made from hot rolling to cold rolling. Further increasing the rolling reduction to 80%, similar trend is observed in the case of in FP. However, in the case of FB and FM, random orientation is observed.

5.6 References:

[1] J.-Y. Kang, D.-I. Kim, H.-C. Lee, Texture Development in Low Carbon Sheet Steels for Automotive Application, Microstruct. Texture Steels. (2009) 85–101. https://doi.org/10.1007/978-1-84882-454-6_5.

[2] D. Raabe, B. Sun, A. Kwiatkowski Da Silva, B. Gault, H.W. Yen, K. Sedighiani, P. Thoudden Sukumar, I.R. Souza Filho, S. Katnagallu, E. Jägle, P. Kürnsteiner, N. Kusampudi, L. Stephenson, M. Herbig, C.H. Liebscher, H. Springer, S. Zaefferer, V. Shah, S.L. Wong, C. Baron, M. Diehl, F. Roters, D. Ponge, Current Challenges and Opportunities in Microstructure-Related Properties of Advanced High-Strength Steels, Metall. Mater. Trans. A Phys. Metall. Mater. Sci. 51 (2020) 5517–5586. https://doi.org/10.1007/s11661-020-05947-2.

[3] T. Gladman, Precipitation-hardening of metals., Mater. Sci. Technol. 15 (1999) 205–211. https://doi.org/https://doi.org/10.1179/026708399773002782.

[4] O. Grässel, L. Krüger, G. Frommeyer, L.W. Meyer, High strength Fe-Mn-(Al, Si) TRIP/TWIP steels development - properties - application, Int. J. Plast. 16 (2000) 1391–1409. https://doi.org/10.1016/S0749-6419(00)00015-2.

[5] M.S. Rashid, Dual-phase steels, Automot. Steels Des. Metall. Process. Appl. (1981) 169–216. https://doi.org/10.1016/B978-0-08-100638-2.00007-9.

[6] S. Janakiram, J.P. Gautam, A. Miroux, J. Moerman, L. Kestens, Microstructure and Texture Control in Cold Rolled High Strength Steels, Diffus. Found. 22 (2019) 84–93. https://doi.org/10.4028/www.scientific.net/df.22.84.

[7] R. Kuziak, R. Kawalla, S. Waengler, Advanced high strength steels for automotive industry: A review, Arch. Civ. Mech. Eng. 8 (2008) 103–117. https://doi.org/10.1016/s1644-9665(12)60197-6.

[8] J. Gautam, A. Miroux, J. Moerman, L. Kestens, TNR dependent hot rolling microstructure and texture development in c-Mn dual phase and HSLA steels, Defect Diffus. Forum. 391 (2019) 120–127. https://doi.org/10.4028/www.scientific.net/DDF.391.120.

[9] M. Takahashi, Development of high strength steels for automobiles, Nippon Steel Tech. Rep. (2003) 2–7. https://doi.org/10.2320/materia.36.502.

[10] C.C. Tasan, M. Diehl, D. Yan, M. Bechtold, F. Roters, L. Schemmann, C. Zheng, N. Peranio, D. Ponge, M. Koyama, K. Tsuzaki, D. Raabe, An Overview of Dual-Phase Steels: Advances in Microstructure-Oriented Processing and Micromechanically Guided Design, Annu. Rev. Mater. Res. 45 (2015) 391–431. https://doi.org/10.1146/annurev-matsci-070214-021103.

[11] J. Galán, L. Samek, P. Verleysen, K. Verbeken, Y. Houbaert, Advanced high strength steels for automotive industry, Rev. Metal. 48 (2012) 118–131. https://doi.org/10.3989/revmetalm.1158.

[12] P.S. Bate, J. Quinta da Fonseca, Texture development in the cold rolling of IF steel, Mater. Sci. Eng. A. 380 (2004) 365–377. https://doi.org/10.1016/j.msea.2004.04.007.

[13] L.A.I. Kestens, H. Pirgazi, Texture formation in metal alloys with cubic crystal structures, Mater. Sci. Technol. (United Kingdom). 32 (2016) 1303–1315. https://doi.org/10.1080/02670836.2016.1231746.

[14] H. Inagaki, Fundamental Aspect of Texture Formation in Low Carbon Steel, ISIJ Int.

34 (1994) 313–321. https://doi.org/10.2355/isijinternational.34.313.

[15] R.K. Ray, J.J. Jonas, R.E. Hook, Cold rolling and annealing textures in low carbon and extra low carbon steels, 1994. https://doi.org/10.1179/imr.1994.39.4.129.

[16] D.K. Matlock, J.G. Speer, Third Generation of AHSS: Microstructure Design Concepts, Microstruct. Texture Steels. (2009) 185–205. https://doi.org/10.1007/978-1-84882-454-6_11.

[17] M. Calcagnotto, D. Ponge, E. Demir, D. Raabe, Orientation gradients and geometrically necessary dislocations in ultrafine grained dual-phase steels studied by 2D and 3D EBSD, Mater. Sci. Eng. A. 527 (2010) 2738–2746. https://doi.org/10.1016/j.msea.2010.01.004.

[18] J. Kadkhodapour, S. Schmauder, D. Raabe, S. Ziaei-Rad, U. Weber, M. Calcagnotto, Experimental and numerical study on geometrically necessary dislocations and non-homogeneous mechanical properties of the ferrite phase in dual phase steels, Acta Mater. 59 (2011) 4387–4394. https://doi.org/10.1016/j.actamat.2011.03.062.

[19] R.R. Shen, V. Ström, P. Efsing, Spatial correlation between local misorientations and nanoindentation hardness in nickel-base alloy 690, Mater. Sci. Eng. A. 674 (2016) 171–177. https://doi.org/10.1016/j.msea.2016.07.123.

[20] J.J. Roa, P. Sudharshan Phani, W.C. Oliver, L. Llanes, Mapping of mechanical properties at microstructural length scale in WC-Co cemented carbides: Assessment of hardness and elastic modulus by means of high speed massive nanoindentation and statistical analysis, Int. J. Refract. Met. Hard Mater. 75 (2018) 211–217. https://doi.org/10.1016/j.ijrmhm.2018.04.019.

[21] S. Janakiram, P.S. Phani, G. Ummethala, S.K. Malladi, J. Gautam, L.A.I. Kestens,

New insights on recovery and early recrystallization of ferrite-pearlite banded cold rolled high strength steels by high speed nanoindentation mapping, Scr. Mater. 194 (2021) 113676. https://doi.org/10.1016/j.scriptamat.2020.113676.

[22] S. Janakiram, P.S. Phani, G. Ummethala, H.V. Jagdeesh, S.K. Malladi, J. Gautam, L.A.I. Kestens, Insights on early recovery kinetics in ferrite - pearlite cold rolled high strength sheet steels, Mater. Charact. 193 (2022). https://doi.org/10.1016/j.matchar.2022.112332.

[23] B. Vignesh, W.C. Oliver, G.S. Kumar, P.S. Phani, Critical assessment of high speed nanoindentation mapping technique and data deconvolution on thermal barrier coatings, Mater. Des. 181 (2019) 108084. https://doi.org/10.1016/j.matdes.2019.108084.

[24] M.A.W. J. A. Hartigan, Algorithm AS 136 A K-Means Clustering Algorithm, J. R. Stat. Soc. Ser. B Methodol. 28 (2012) 100–108. https://doi.org/http://www.jstor.org/page/info/about/policies/terms.jsp .

[25] E.A. Ariza-Echeverri, M. Masoumi, A.S. Nishikawa, D.H. Mesa, A.E. Marquez-Rossy, A.P. Tschiptschin, Development of a new generation of quench and partitioning steels: Influence of processing parameters on texture, nanoindentation, and mechanical properties, Mater. Des. 186 (2020) 108329. https://doi.org/10.1016/j.matdes.2019.108329.

[26] C.A. Naik, B.K.S. Kumar, S. Harita, S. Roshan, S. Janakiram, P.S. Phani, J.P. Gautam, Assessment of structure-property relationships at the micrometer length scale in dual phase steels by electron microscopy and nanoindentation, Mater. Today Commun. 38 (2024) 107696. https://doi.org/10.1016/j.mtcomm.2023.107696.

[27] F.M.C. Cerda, Third Generation Advanced High Strength Steels via Ultrafast Heating,

2017.

Chapter 6 Effect of initial microstructure on recrystallization and local mechanical properties in dual phase steels

A systematic experimental investigation was undertaken to provide insights on the role of secondary constituents on the recrystallization of dual-phase steels at the micrometer length scale. Three distinct combinations of dual phase microstructures, with ferrite as the matrix, were selected and subjected to cold rolling, followed by recrystallization at 725°C for varying holding intervals. The microstructural observed at each stage exhibited several distinct features, including strain accumulation, hardening, subsequent recrystallization and precipitation. Electron microscopy and nanoindentation were employed to capture the microstructure and local mechanical properties at each stage at the micrometer length scale. A comprehensive understanding of role of ferrite and second phase / constituent at each stage, both structurally and mechanically, was facilitated through direct correlations between microstructure, misorientation, and deconvoluted hardness or mechanical phase maps. The driving force and competition between various processes during recrystallization are also discussed.

6.1 Introduction:

The widely used category of high-strength automotive sheet steels, such as dual-phase (DP) steels, exhibit a commendable combination of ductility and strength [2] These steels are and will continue to be the most often utilised in current and future cars [3] due to high strength to weight ratio which improves fuel efficiency [2,4] . The ability to balance ductility without compromising strength is determined by how well one can regulate the thermomechanical cycle to influence the type, size, shape, and distribution of the hard constituents in the soft matrix [5,6] of the DP steels. Ferrite-martensite is the proved potential candidate providing excellent combination of strength and formability due to its load partitioning, initial strain hardening and toughness. The ability to tailor the martensite size, fraction and distribution in the ferrite matrix is majorly driven by the initial microstructure, prior deformation and annealing temperature that eventually influences the ferrite recrystallization and austenite formation[7] [8]. It was also reported that using martensite as the initial microstructure with high heating rate causes enhanced recrystallization resulting in finer microstructure, which offers better prperties [9,10]. However, the microstructures which includes other constituents such as ferrite-bainite-pearlite, and ferrite-pearlite with 50% cold deformation resulted in slower kinetics for recrystallization which also affects the subsequent austenite formation at higher temperatures [11]. The energy stored within the material in the form of strain due to prior deformation or due to the intrinsic attributes will determine the actual driving force for recrystallization and phase transformation [12–14]. During deformation of samples with dual phases microstructure, the softer component will have a greater tendency to accommodate deformation and subsequently it undergoes faster recrystallization. The amount of strain accumulation depends on various factors like extent of deformation, size and distribution of hard phase, etc. Rana et.al. [15] showed deformation concentration in soft matrix (ferrite) when it deforms along with hard phases (martensite) [16] with digital image correlation (DIC). The grain size and volume percentage of the martensite had a substantial impact on load partitioning. Partitioning occurs when grain size decreases and volume fraction increases due to the development of higher stress triaxiality by creating more opportunities to resist deformation [15,17]. Along with the initial microstructure and stored energy in terms of induced strain, annealing process parameters like temperature, heating rate, and holding intervals have a substantial influence on the kinetics of ferrite recrystallization. During annealing, several processes such as recovery, recrystallization, grain growth and phase transformation, may suppress, dominate, or overlap with each another[7]. For example, a strong competition between recrystallization and austenite formation [7]was observed in dual phase steels with increasing heating rate [9]. Li et al. showed that the fraction of recrystallized grains decreased and delay in spheroidization of cementite in the lamellae of pearlite was observed with increasing heating rate [18]. Defect rearrangement, grain boundary mobility and carbon diffusion are temperature and time-controlled phenomena which can be significantly affected by the heating rate. Interestingly, during the early phase of recovery/recrystallization in dual phase [7] deformed steels, an increase in hardness has been reported, which has been attributed to the formation of Cottrell atmosphere which leads localized bake hardening [19,20].

While recrystallization in dual phase steels has been widely studied at the macroscale, similar studies at the micrometer length scale or at the length scale of the constituent phases, are limited. Given that multiple physical mechanisms can operate during recrystallization which in many cases compete, it is important to be able to track the local mechanical properties of the constituents at micrometer scales and accordingly relate that to the microstructural evolution to enable a comprehensive understanding of recrystallization in dual phase steels. Hence, in this chapter, a systematic attempt is made to understand some of these concurrent events during recrystallization at the scale of the microstructure. Three different dual phase microstructures, ferrite-pearlite (FP), ferrite-bainite (FB), ferrite-martensite (FM) were produced from a steel with nominal composition of DP600 after hot rolling and coiling, followed by cold rolling. These three microstructures are subjected to high temperature annealing at 725ºC to understand the events during recrystallization by utilizing electron microscopy and nanoindentation.

6.2 Experimental procedure:

6.2.1 Material composition and phase fraction:

The microstructure of the hot-rolled and coiled sheet close to DP600 composition, was extensively discussed in Chapter 4. These samples were subjected to cold deformation of 80%, as detailed in Chapter 5. Subsequently, the sheets underwent annealing in a salt bath furnace at a temperature of 725°C, intentionally maintained below the critical temperature (AC1). The heating rate employed in the salt bath furnace was 185°C/s, followed by specific soaking durations of 10s, 30s, 60s, 180s, 300s, 600s, and 900s. The annealed sheets were then subjected to rapid water quenching to preserve the microstructure.

6.2.2 Microstructural and mechanical characterization:

The specimens underwent standard polishing procedures for scanning electron microscopy (SEM), and electron backscatter diffraction (EBSD), as extensively discussed in Chapter 3. The EDAX OIM software was subsequently employed for analysis. Electron backscatter diffraction kernel average misorientation (EBSD-KAM) maps were generated with a 5th nearest neighbour criterion and a misorientation threshold set at 3°. The bulk hardness of the specimens was determined using the Tinius Olsen FH-006 series of Vickers hardness tester. Local mechanical properties were measured using the high-speed nanoindentation technique, NanoBlitz 3D+. The mapping was conducted with a commercially available nanoindenter, iMicro®, featuring an InForce50 actuator from Nanomechanics Inc. (now KLA, Oak Ridge, USA) [20]. For each map, a total of 3600 indents were placed in a grid pattern of 60X60 indents, with a spacing of 1 µm and a maximum indentation depth of 100 µm [21].

6.3 Results:

6.3.1 Microstructure after cold rolling:

The microstructure after 80% cold rolling (prior to annealing) is shown in Fig. 6-1 for FP, FB and FM. Fig. 6-1(a) shows the 80% cold rolled ferrite-pearlite (FP) microstructure which consists of the banded type structure with elongated grains along the rolling direction of ferrite and pearlite, accompanied by finely fragmented cementite, as seen from the higher magnification image of Fig. 6-1(a). In the case of FB shown in Fig. 6-1(b), the cold deformation process resulted in severe distortion and alignment of the ferrite phase along the deformation direction, while the bainite underwent significant fragmentation and dispersion throughout the ferrite matrix. Unlike the pearlite, which formed clear bands, the bainite had a more uniform distribution in the microstructure. The deformation effects on the ferrite and martensite phases in the FM microstructure are shown in Fig. 6-1(c). Compared to the FB microstructure, the FM microstructure exhibited more refined and elongated ferrite grains along the deformation direction, as well as more fragmented and uniformly distributed martensite particles in the ferrite matrix. This could be attributed to the enhanced load partitioning that occurred between the hard martensite phase and the soft ferrite phase.

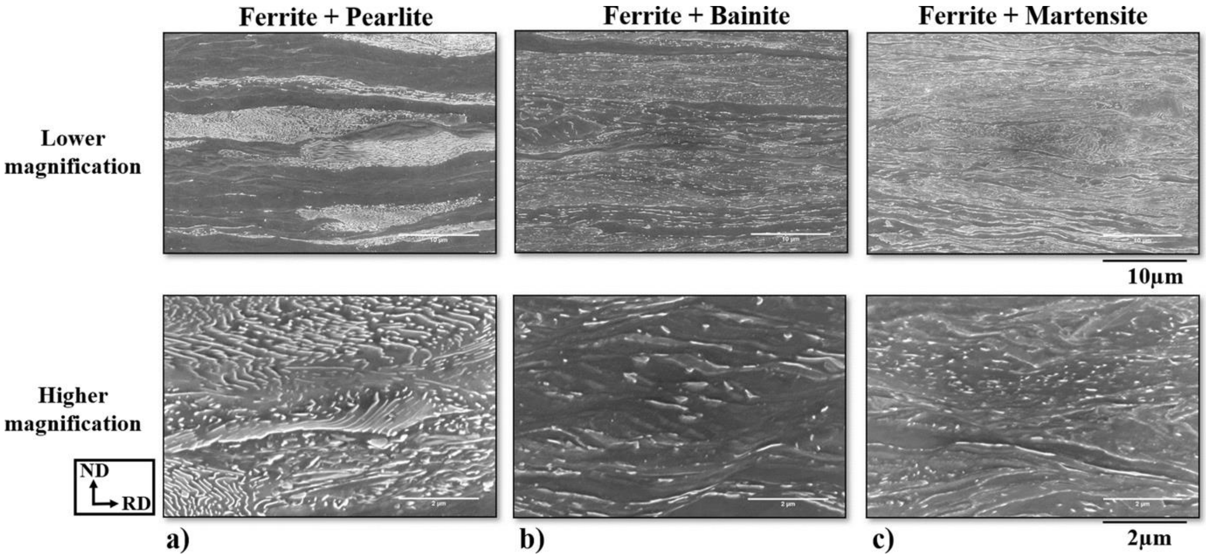

Figure 6-1: SEM micrographs after 80% cold rolling, along with their higher magnification images for (a) FP, (b) FB, and (c) FM.

6.3.2 Microstructural evolution during annealing at 725ºC:

The samples that underwent 80% cold rolling were annealed at 725ºC with a high heating rate of 185ºC/s in salt bath furnace and immediately quenching in water. The SEM micrographs of the annealed FP, FB and FM samples with different soaking times are shown in Fig. 6-2. The FP microstructures retained the evidence of the prior deformation even after soaking for 10s, as seen in Fig. 6-2(a). However, after soaking for 60s, the ferrite grains became more heterogeneous in size, ranging from < 1µm to 5-6 µm. This could be explained by the occurrence of recovery and partial recrystallization processes that depends on the heating rate and soaking time, which will be discussed in more detail in the following sections. At this soaking time, fine high-contrast features appeared in the microstructure, which could be attributed to the formation and distribution of carbides or clusters. These features became more distinct and frequent at longer soaking times. With soaking the ferrite grains also increased, reaching 8.0 ± 1.2 µm for 300s and 9.1 ± 0.7µm for 900s, and the grain size heterogeneity decreased with increasing soaking time. The banded structure was completely eliminated at longer soaking times.

The FB microstructure showed residual deformation features after 10s of soaking at 725ºC, as seen in Fig. 6-2(a). However, the microstructure changed significantly after 60s of soaking, exhibiting distinct characteristics, as shown in Fig. 6-2(b). The ferrite grains, which were fine and elongated after 10s of soaking, grew considerably to 6.2 ± 1.7 µm, 9.7 ± 1.2 µm and 11 ± 1.3 µm after 60s, 300s and 900s of soaking, respectively. Similar to the FP microstructure, fine high-contrast features, which could be carbides or clusters, were observed in the ferrite matrix after 60s of soaking. These features decreased in density and segregated to the grain boundaries and triple junctions of the ferrite grains with increasing soaking time, as show in Fig. 6-2(c-d).

The FM microstructure showed distinct and uniform changes after 10s of soaking, as shown in Fig. 6-2(a). The ferrite phase maintained the deformation features until 10s, but not after 60s. The ferrite grain size also increased gradually, reaching 6.5 ± 1.3 µm, 9.8 ± 1.2 µm and 11 ± 1.9 µm after 60s, 300s and 900s of soaking, respectively. The carbides or clusters segregated to the grain boundaries, as evident from the micrographs of 300s and 900s in Fig. 6-2(c-d).

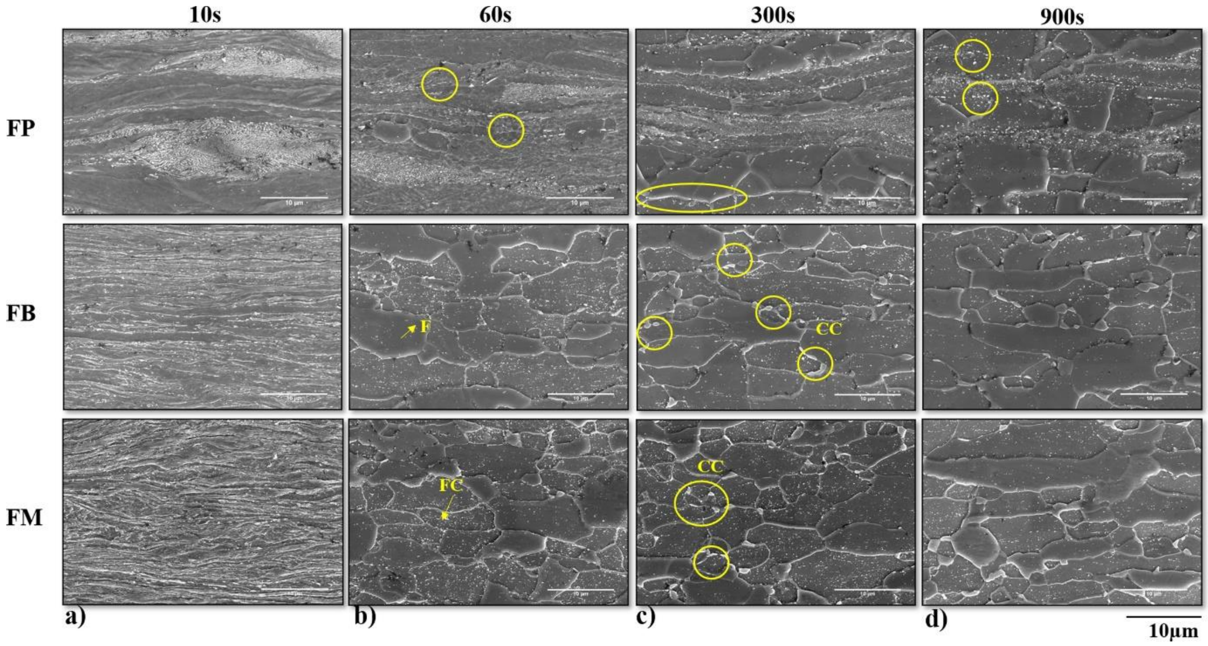

Figure 6-2: SEM micrographs of FP, FB, and FM after annealing at 725ºC after soaking time of (a) 10s, (b) 60s, (c) 300s, and (d) 900s.

6.3.3 Microstructural evolution observed using EBSD KAM maps:

Kernel Average Misorientation (KAM) can be used to study various aspects of recrystallization, such as strain localization, defect distribution, grain boundary characterization, etc. KAM is therefore a useful instrument for assessing the recrystallization process and its consequences on the microstructure. Fig. 6-3 shows the spatial distribution of KAM (5th neighbour, < 3° threshold) for the annealed samples with different soaking times. KAM analysis for the cold rolled specimens was presented in chapter 5 and here we focus only on the recrystallization part. The misorientation levels observed in all materials after a 10 second holding interval are notably high, suggesting that the deformation strain induced by cold rolling remains largely unaffected by the subsequent annealing and brief holding period. With increasing time intervals, the FP sample exhibits a gradual decrease in misorientations; although even after 900s, regions with high misorientations persist. In contrast, the FB and FM samples show a distinct drop in misorientations in the matrix at 60 seconds, followed by the emergence of higher misorientations at some regions such as triple points. This observation aligns with the microstructural observations, indicating the potential presence of carbides/clusters at triple points with elevated misorientations. These findings suggest that the recrystallization kinetics are considerably faster in the case of FB and FM, reaching a saturation level in terms of recrystallization after 60s and subsequently forming carbides/clusters with prolonged annealing.

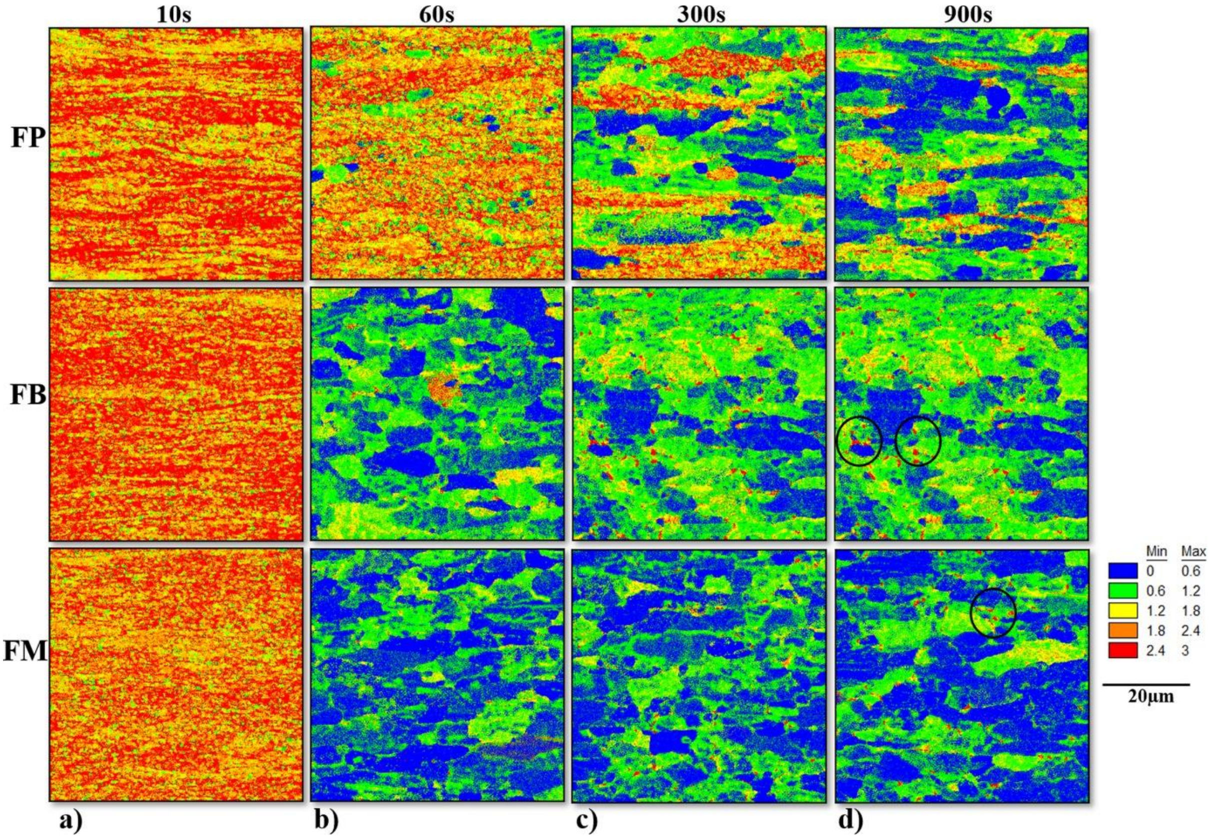

Figure 6-3: Kernel average misorientation maps for FP, FB, and FM at an annealing temperature of 725ºC after soaking for (a) 10s, (b) 60s, (c) 300s, and (d) 900s.

6.3.4 Effect of soaking time on KAM

The KAM maps shown in the previous sub-section are further analysed by plotting their distribution. Fig. 6-4 shows the overall KAM histograms for FP, FB, and FM. In Fig. 6-4(a), the KAM distribution of FP shows that at 1s and 60 s, higher misorientation is observed, whereas the misorientations decrease after 300s, indicating discernible recrystallization. In Fig. 6-4(b-c) for FB and FM at 10 seconds, the peak is at higher misorientation as expected. However, as the soaking time increases to 60 and beyond, the peak consistently shifts to the left, signifying lower misorientation in the samples and suggesting a high degree of recrystallization at those soaking times.

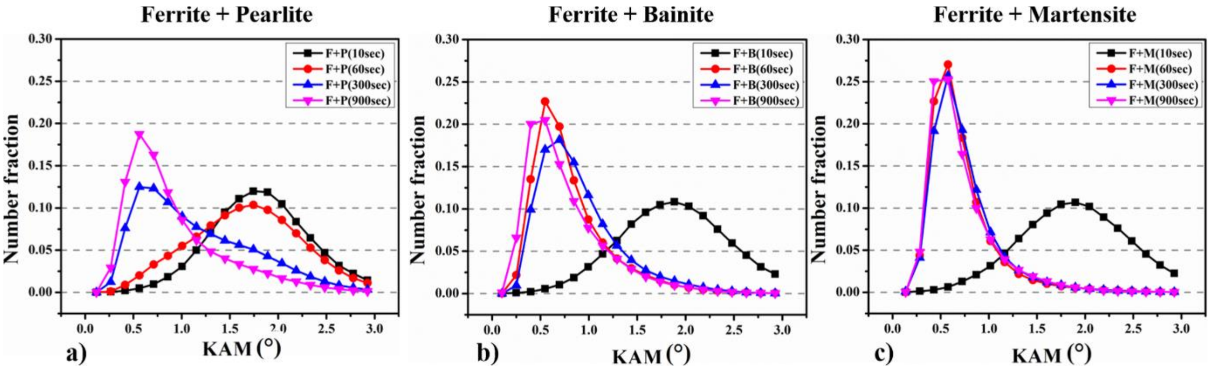

Figure 6-4: Kernel Average Misorientation distribution for (a) FP, (b) FB and (c) FM at different soaking times during annealing at 725ºC.

6.3.5 Recrystallization kinetics at 725ºC:

The EBSD data used for analysing the recrystallization data presented in the previous section is further used to determine the recrystallization kinetics The traditional Johnson and Mehl Avarami (JMAK) [23] model, which is shown in Eq. (1) and where x is the recrystallization fraction, t is the time, and n is the exponent, is used to model the kinetics of the recrystallization.

$x = 1 - \exp(-k\, t^{n})$……………………… (1)

The recrystallization fraction (x) is measured through EBSD data assuming kernel average misorientation <1º as fully recrystallized [24]. The obtained recrystallization fraction with respect to time is show in Fig. 6-5. The fraction increased abruptly in the case of FB and FM, but it is very gradual in the case of FP. After performing a non-linear minimization with the standard JMAK equation for FP, an activation energy (Q) of 307 KJ/mole and an exponent (n) of 1.1 was estimated which is in the range observed in literature [25]. However, it may be noted that there may be multiple concurrent processes that occur as seen from Fig. 6-5(b) and the estimate of the activation energy may not be accurate.

For FB and FM, immediately after 10s of holding period the fraction of recrystallization reaches a high value and remains constant. When compared to FP, the curves of FB and FM show higher slope and higher faction of recrystallization, indicating that they have stronger driving force. Due to the fast kinetics of FB and FM, the JMAK parameters could not be estimated.

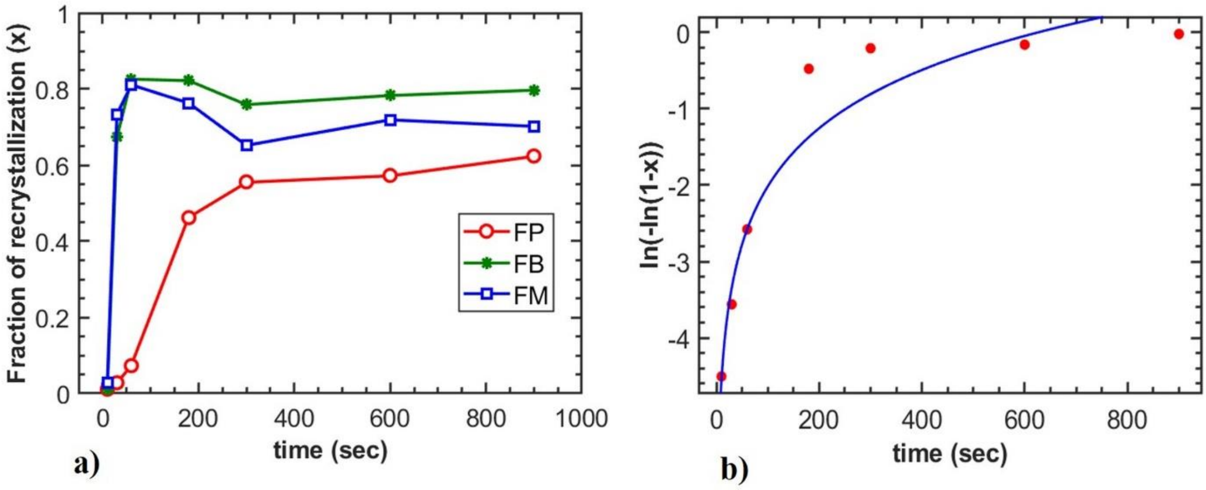

Figure 6-5:(a) Ferrite recrystallization fraction for FP, FB, and FM, and (b) JAMK fit of the recrystallization fraction for FP.

6.3.6 Micro hardness evolution:

Microhardness was measured for all the materials after cold rolling and after annealing at different soaking times as shown in Fig. 6-6. The initial hardness values after 80% cold rolling are high compared to other states, as expected with the FM showing the highest hardness. As soaking duration increases, the hardness of FP exhibits a sharp decline to lower values after an initial rise. This is due to the concurrent processes of recrystallization and bake hardening due to the formation of a Cottrell atmosphere. In contrast, in the case of FB and FM, the hardness shows a continuous decrease. Also, in the case of FP, the decrease in the hardness is gradual with respect to time unlike FB and FM, which show a drastic decrease and after 10s the hardness values are almost constant.

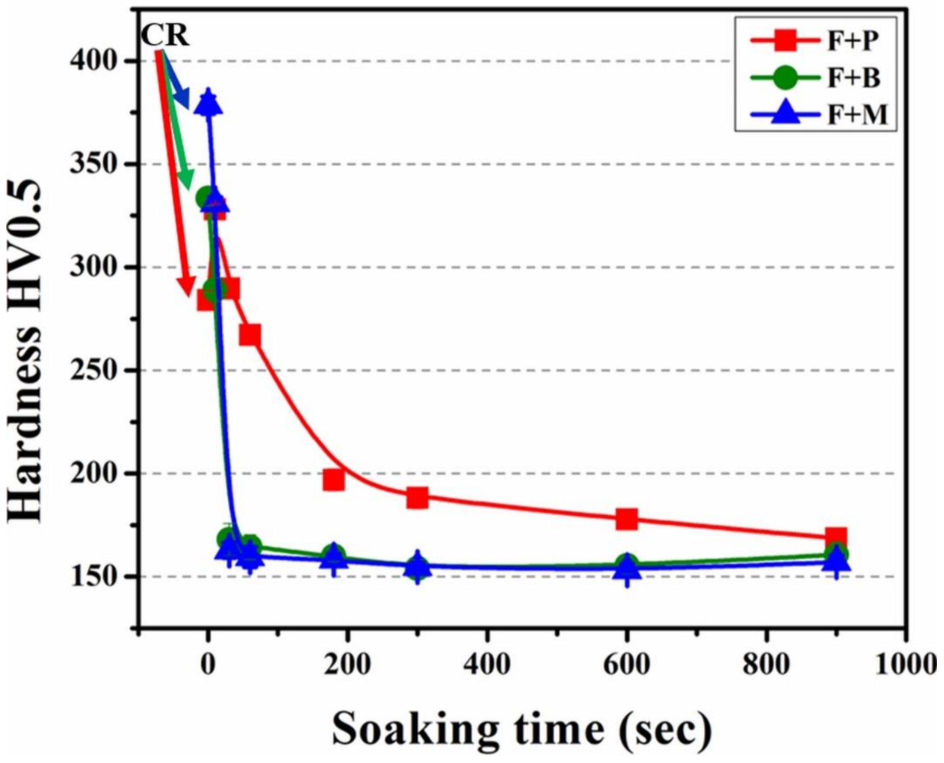

Figure 6-6: Evolution of Vickers microhardness at an annealing temperature of 725ºC for FP, FB, and FM at different soaking times.

6.3.7 Nanoindentation hardness mapping:

The spatial distribution of hardness in the material after cold rolling and annealing for different soaking times was investigated by nanoindentation high speed mapping, as shown in Fig. 6-7. The hardness map revealed two distinct regions with significant hardness contrast in almost all cases. In the case of FP, the region with lower hardness (blue) corresponds to ferrite, while the region with higher hardness represents pearlite in a banded form. The nanoindentation maps not only captured the variations in hardness between ferrite and pearlite, but also the effects of prior deformation, which were not completely eliminated until 60s of soaking time. These hardness results are consistent with the microstructure and KAM analysis presented earlier. The hardness of the ferrite region significantly decreased with increasing soaking the time from 300s to 900s. The extent of hardness decrease for all the samples will be discussed in detail in the next sub-section.

In the case of FB in the cold rolled state, two distinct regions can be observed. These regions correspond to bulk ferrite with lower hardness and ferrite/bainite mixture with higher hardness. The hardness distribution of the annealed sample with 10s holding period is similar to that of the cold rolled sample, as shown in Fig. 6-7(b). However, after 60s of soaking, the hardness of the material drops uniformly throughout, as shown in Fig. 6-7(c). With increasing soaking time, small localized regions with high hardness appear. These regions correspond to the carbides/clusters that are located at boundaries, triple points and are consistent with the micrographs and misorientation maps presented earlier.

In the case of the FM sample, the hardness is clearly higher than that of the FP and slightly higher than FB, as shown in Fig. 6-7(a). The hardness of the FM slightly decreased after annealing for 10s, but the effects of deformation were still evident, as shown in Fig. 6-7(b). However, after 60s of soaking, the hardness of the FM dropped to lower values, similar to the FB case, as shown in Fig. 6-7(c). With increasing soaking time, small regions with high hardness emerged especially after 300s at specific locations, which could be carbides/clusters formed due to longer holding periods as also seen in the case of FB.

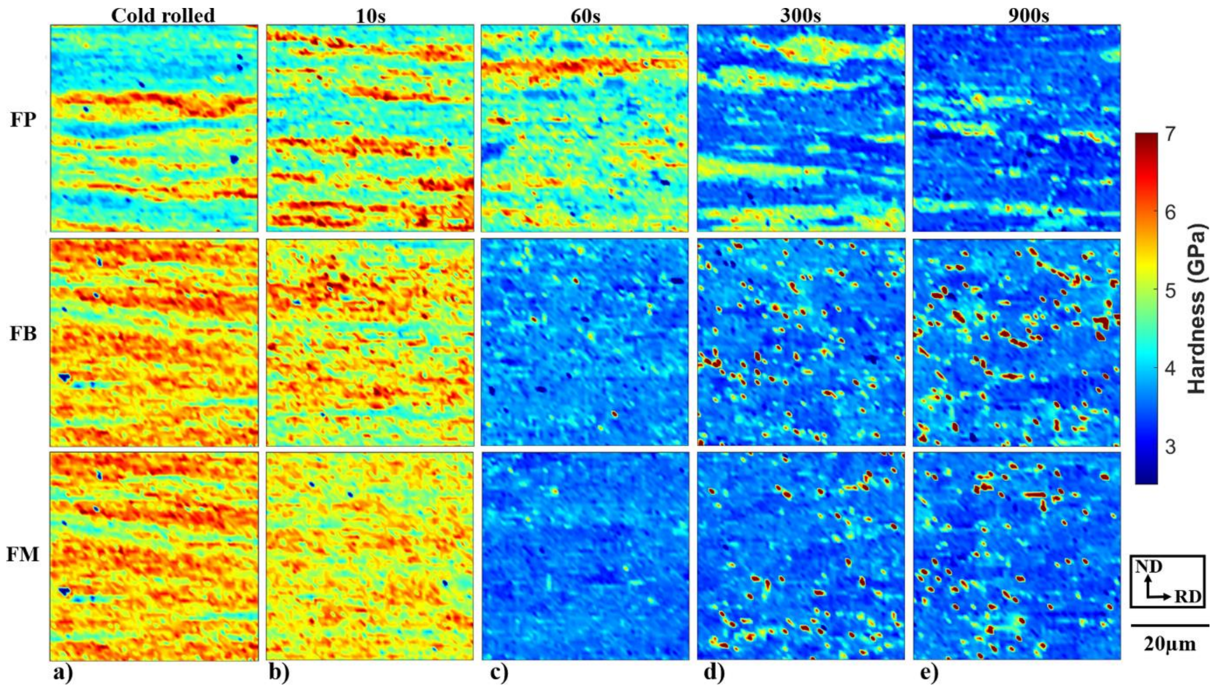

Figure 6-7: Nanoindentation hardness maps of FP, FB and FM after (a) 80% cold rolling and after subsequent annealing at 725ºC for different soaking times of (b) 10s, (c) 60s, (d) 300s and (e) 900s.

6.3.8 Nanoindentation hardness histogram:

Figure 6-8 shows the hardness histograms of FP, FB and FM after annealing for different durations. In the case of FP shown in Fig. 6-8(a), the cold-rolled state and the soaking durations up to 60s show high hardness. In fact, a slight increase in hardness up to 60s soaking can also be observed, as was the case in Vickers hardness measurements. Hardness clearly decreases with additional annealing. The 10s sample is closely followed by the cold rolled state in the FB and FM shown in Fig. 6-8(b-c) which exhibits the highest hardness. Further annealing results in significant reduction in hardness as evidenced by peak shift towards the left. This is in good agreement with the Vickers hardness results and the microstructural analysis that was previously provided. In the next section, we will present an assessment of the correlation between the microstructure and the hardness maps at the micrometer length scale.

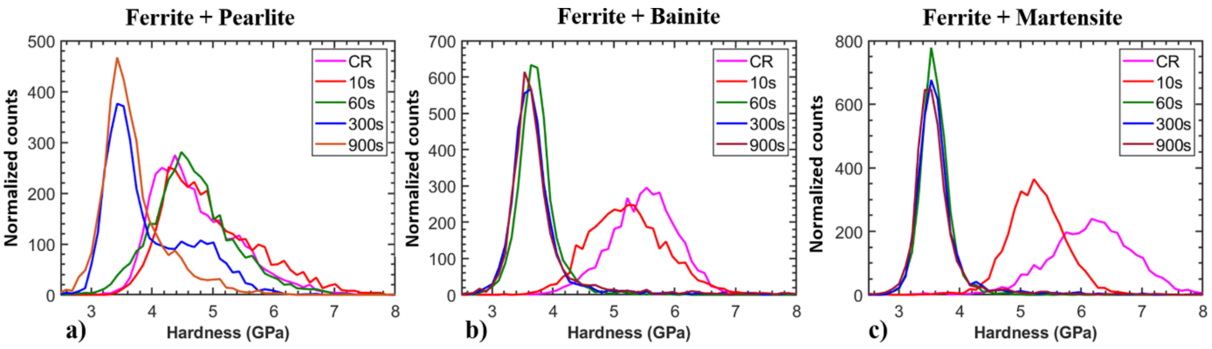

Figure 6-8: Nanoindentation hardness histograms after annealing at 725^{o}C for different soaking times in the case of (a) FP, (b) FB and (c) FM.

6.4 Discussion

6.4.1 Assessment of microstructure and mechanical properties at micrometer length scale during recrystallization annealing of ferrite-pearlite (FP):

Fig. 6-9 shows the SEM micrographs and the corresponding hardness maps of the FP samples annealed at 725^{o}C for different soaking times. Good agreement between the microstructure and hardness map is observed for all the cases. Fig. 6-9(a) shows the initial cold-rolled microstructure, where ferrite and pearlite have different contrasts in the SEM image, with pearlite being the lighter shade. Fig. 6-9(b) shows the sample after 10s of soaking time, where the hardness map reveals that the pearlite bands have higher hardness than the cold rolled condition, due to the Cottrell atmosphere formation as discussed earlier. Fig. 6-9(c) shows the sample after 60s of soaking time, where the recrystallization of ferrite at the grain boundary has started, as also evidenced by the decrease in hardness. Fig. 6-9(d-e) show the samples after 300s and 900s of soaking time, respectively, where the recrystallization of ferrite has progressed and the hardness has decreased further.

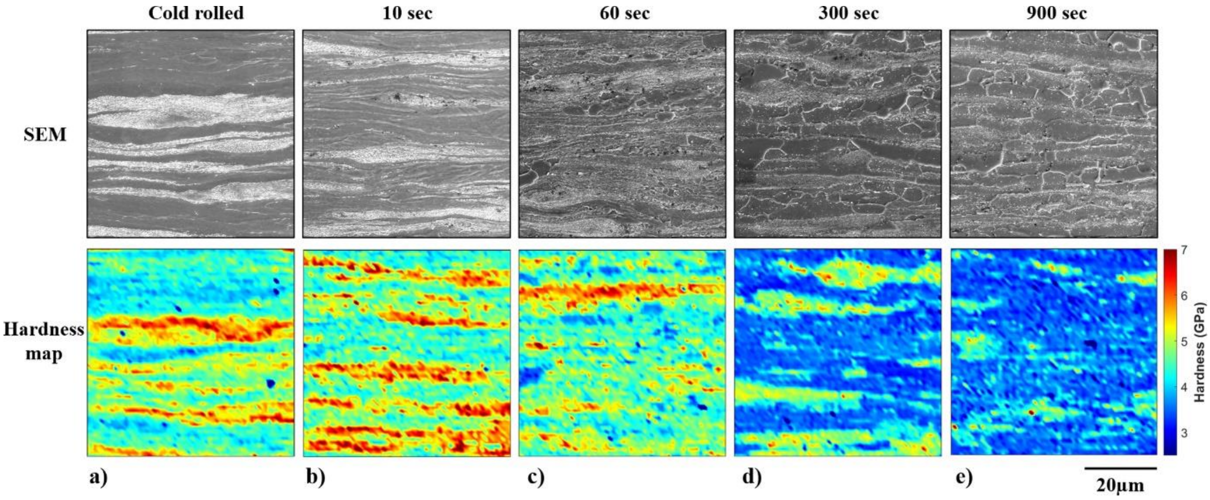

Figure 6-9: SEM micrographs along with the corresponding hardness maps in FP after (a) cold rolling and subsequent annealing at 725°C, for soaking times of (b) 10s, (c) 60s, (d) 300s, and (e) 900s.

To quantify the change in hardness during annealing, the hardness maps are deconvoluted to obtain the hardness of the individual constituents. Fig. 6-10 shows the deconvoluted maps and the hardness histograms corresponding to the maps assuming a Gaussian distribution. The blue color represents ferrite, while the red color corresponds to pearlite. The deconvoluted maps correspond well with the SEM micrographs shown in Fig. 6-9. The histograms not only show the hardness difference between ferrite and pearlite but also the corresponding change with annealing. During the initial stages of annealing, the hardness increases in both ferrite and pearlite due to bake-hardening like phenomena [19,20], subsequently followed by a hardness decrease due to ferrite recrystallization and cementite spheroidization.

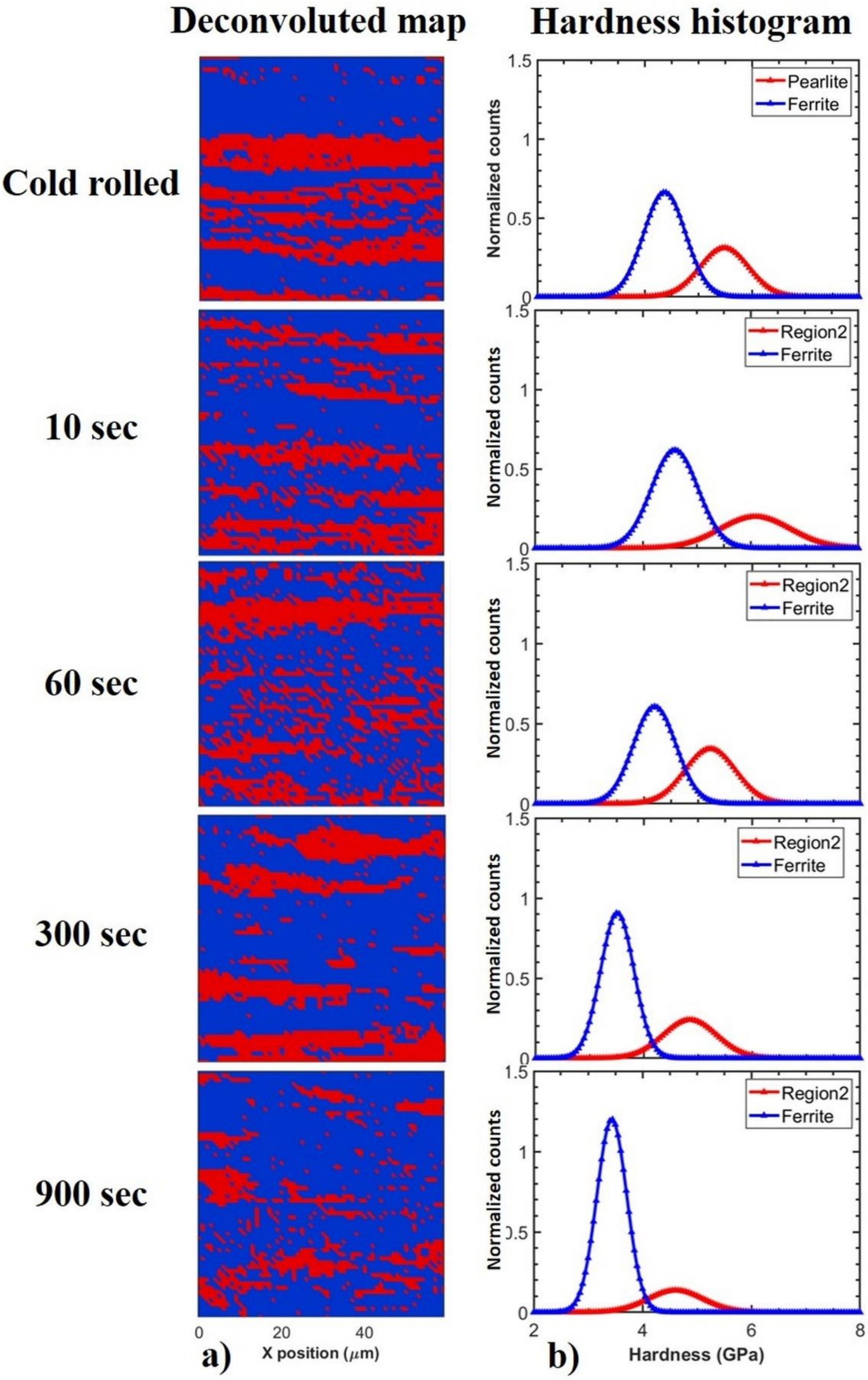

Figure 6-10: (a) Deconvoluted hardness maps and (b) hardness histograms in FP after cold rolling and subsequent annealing at 725^{o}C, for different soaking times.

6.4.2 Assessment of microstructure and mechanical properties at micrometer length scale during recrystallization annealing of ferrite-bainite (FB):

Figure 6-11 shows the SEM micrographs and the corresponding hardness maps of the FB samples annealed at 725^{o}C for different soaking times. Reasonable agreement between the microstructure and hardness map is observed for all the cases. The microstructure shown in Fig. 6-11(a-b) clearly shows the effect of cold rolling even after soaking for 10s. The corresponding hardness maps also indicate the same. Upon further soaking to 60s, the microstructure shows recrystallized ferrite grains and this change is more evident in the hardness map that shows a significant reduction in hardness in both the constituents. This trend continues in ferrite with increasing soaking time. However, with increasing soaking time (300s and 900s), carbides form at the triple junction of ferrite grain boundaries and this is well captured by nanoindentation, which shows elevated hardness at these locations.

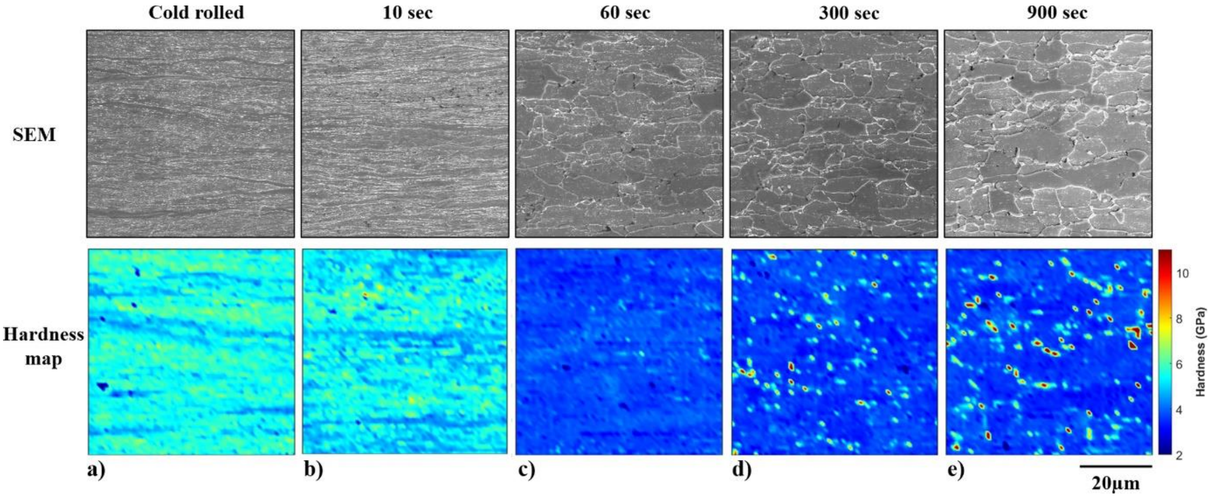

Figure 6-11: SEM micrographs along with the corresponding hardness maps in FB after (a) cold rolling and subsequent annealing at 725^{o}C, for soaking times of (b) 10s, (c) 60s, (d) 300s, and (e) 900s.

Similar to the case of FP, to quantify the change in hardness during annealing, the hardness maps are deconvoluted to obtain the hardness of the individual constituents. Fig. 6-12 shows the deconvoluted maps and the hardness histograms corresponding to the maps. The blue color represents ferrite, while the red color corresponds to mixture of bainite/carbide and ferrite labelled as region 2. Unlike the case of FP, where the pearlite was simple to identify, the finer length scale of bainite results in a mixture of ferrite and bainite/carbides being identified as the secondary constituent. In spite of this challenge, there is still reasonable agreement between the deconvoluted map and the microstructure. The corresponding histograms show that the hardness of the ferrite and the bainite-ferrite mixture (region 2) is retained up to 10s, followed by a drastic reduction in hardness of ferrite and to a lesser extent in bainite-ferrite mixture. However, further annealing results in formation of the carbides at the grain boundaries, which are much finer and the hardness of which may not be accurately determined. Also, broadening of the ferrite peak and near extinction of the ferrite+bainite peak (region 2) can be observed.

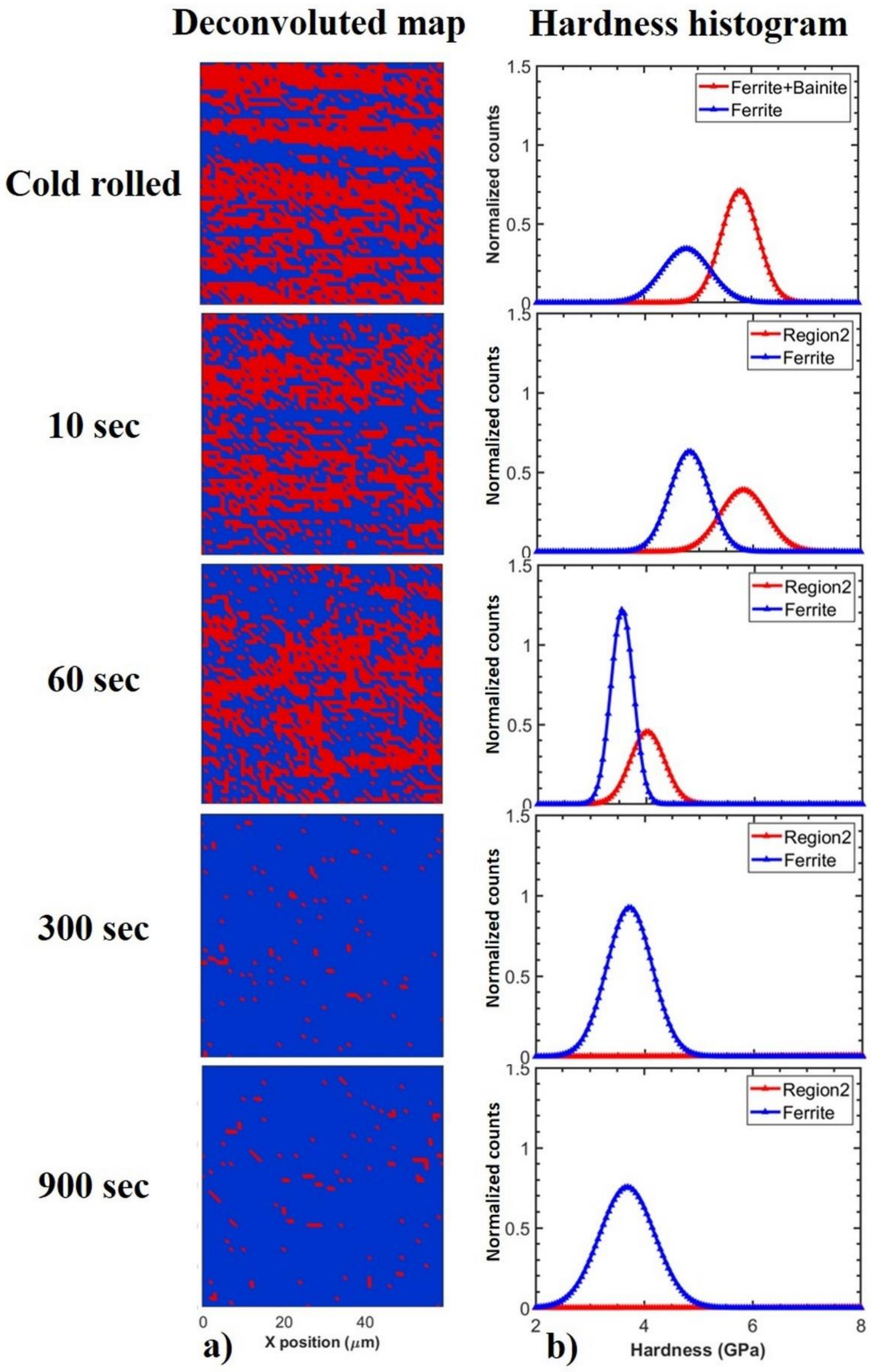

Figure 6-12: (a) Deconvoluted hardness maps and (b) hardness histograms in FB after cold rolling and subsequent annealing at 725°C, for different soaking times.

6.4.3 Assessment of microstructure and mechanical properties at micrometer length scale during recrystallization annealing of ferrite-martensite (FM):

Figure 6-13 shows the SEM micrographs and the corresponding hardness maps of the FM samples annealed at 725°C for different soaking times. Reasonable agreement between the microstructure and hardness map is observed for all the cases. The behavior of FM samples during recrystallization closely follows the trend described for FB in the previous sub-section. The microstructure shown in Fig. 6-13(a-b) clearly shows the effect of cold rolling even after soaking for 10s. The corresponding hardness maps also indicate the same. Upon further soaking to 60s, the microstructure shows recrystallized ferrite grains, and this change is more evident in the hardness map that shows a significant reduction in hardness in both the constituents. This trend continues in ferrite with increasing soaking time. However, with increasing soaking time (300s and 900s), carbides form at the triple junction of ferrite grain boundaries and this is well captured by nanoindentation, which shows elevated hardness at these locations. Slightly coarser carbides are observed in FM compared to FB.

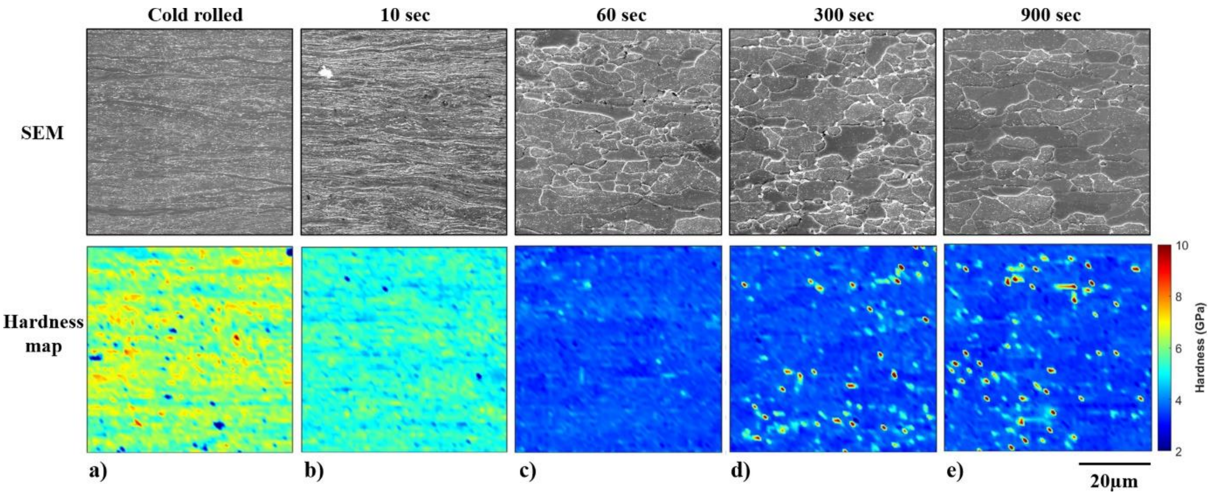

Figure 6-13: SEM micrographs along with the corresponding hardness maps in FM after (a) cold rolling and subsequent annealing at 725°C, for soaking times of (b) 10s, (c) 60s, (d) 300s, and (e) 900s.

Similar to the case of FP and FB, to quantify the change in hardness during annealing, the hardness maps are deconvoluted to obtain the hardness of the individual constituents. Fig. 6-14 shows the deconvoluted maps and the hardness histograms corresponding to the maps. The blue color represents ferrite, while the red color corresponds to mixture of carbide/martensite and ferrite labelled as region 2. As mentioned in the case of FB, the finer length scale of martensite results in a mixture of ferrite and carbide / martensite being identified as the secondary constituent or region 2. In spite of this challenge, there is still reasonable agreement between the deconvoluted map and the microstructure. The corresponding histograms show a trend similar to FB, with the hardness of ferrite being retained up to 10s, followed by a drastic reduction in hardness. The case of martensite-ferrite mixture the hardness shows continuous reduction starting from 10s itself. Similar to the case of FB at higher soaking times (300s and 900s), fine carbides at the grain boundaries, broadening of the ferrite peak and near extinction of the ferrite+carbide / martensite peak (region 2) can be observed.

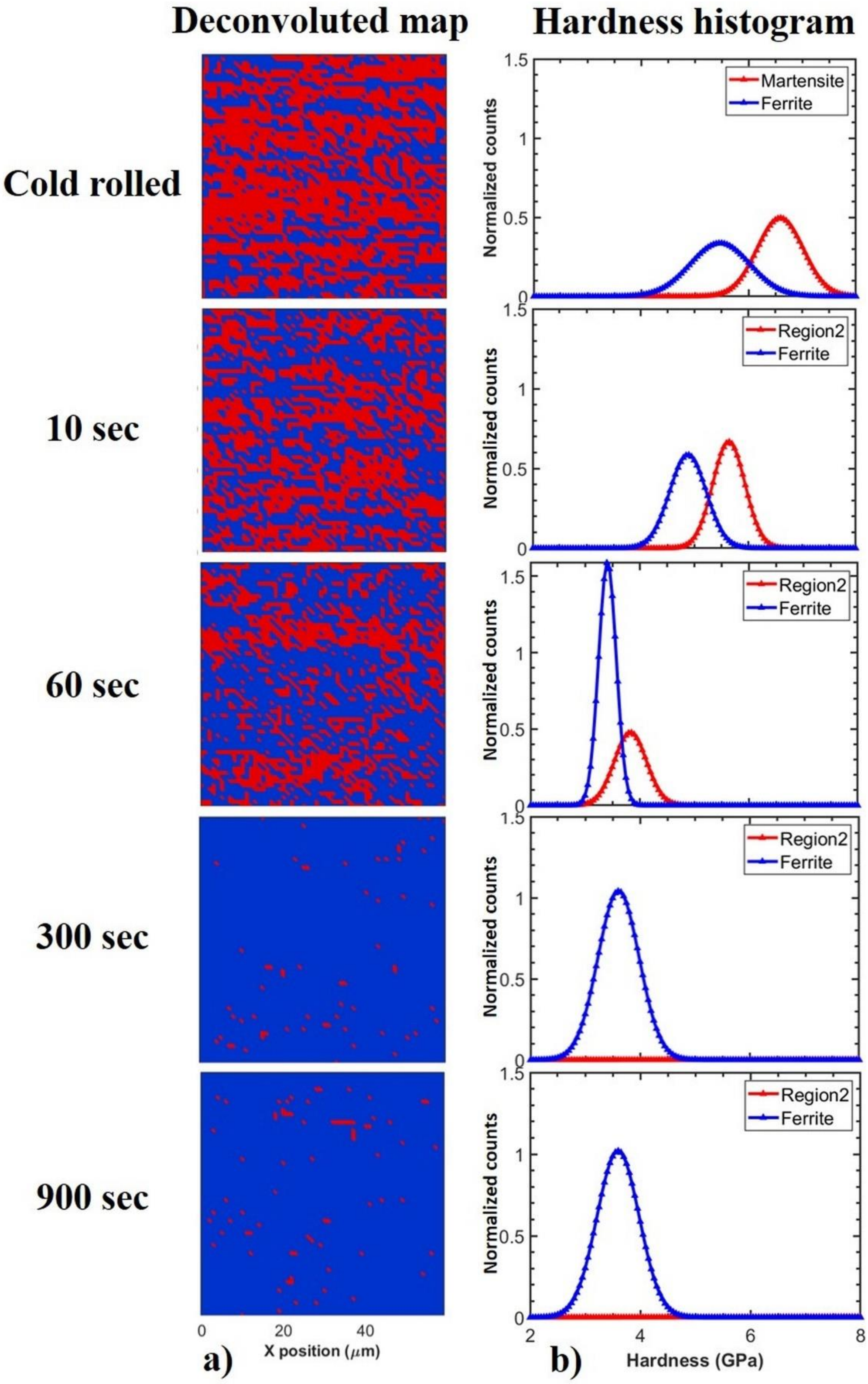

Figure 6-14: (a) Deconvoluted hardness maps and (b) hardness histograms in FM after cold rolling and subsequent annealing at 725°C, for different soaking times.

6.4.4 Effect of the initial microstructure on microstructure and mechanical property evolution during recrystallization:

The hardness evolution during recrystallization of the individual constituents for a given initial microstructure (FP, FB and FM) was presented in the previous sections. Here, the evolution of the hardness of the matrix phase and the secondary constituent will be compared for the different initial microstructures. Fig. 6-15 shows the hardness histograms of ferrite and the second phase constituents of FP, FB and FM for different soaking times during recrystallization annealing at 725ºC. The different colours represent the soaking time: red for 10s, olive green for 60s, blue for 300s and pink for 900s. In the case of ferrite matrix, the hardness in cold rolled state is highest for FM followed by FB and FP. Upon annealing, the hardness of the ferrite decreases gradually in FP compared to FB and FM. Interestingly, the hardness of ferrite after 900s is lowest in FP compared to the others. This is possibly due to the fine carbides observed in FB and FM that can potentially strengthen the ferrite matrix as also observed from the slight increase in hardness in these cases at the higher soaking times (300s and 900s).

It may be noted that the secondary constituent is pearlite in FP, bainite/carbide + ferrite mixture (region 2) in FB and carbide / martensite+ferrite mixture (region 2) in FM. The hardness of the secondary constituent is high in all cases during the initial stages of annealing, followed by different paths later. In the case of FP, hardness decreases due to cementite spheroidization, whereas in the case of FB and FM, the hardness decreases initially due to carbide dissolution and later (300s and 900s) becomes challenging to detect via nanoindentation due to the finer length scale wherein they are found mostly at the grain boundaries.

Overall, the recrystallization kinetics are faster in FM compared to FB and FP. This can be attributed to the higher defect density inherent in the FM microstructure, further enhanced by the 80% deformation acting as a potent driving force or reservoir of higher stored energy for faster ferrite recrystallization. This distinction is also evident in the kernel average misorientation maps shown in Fig. 6-3, wherein the FM microstructures exhibit substantially higher misorientation levels compared to the FB and FP counterparts. This heightened misorientation serves as a driving force for the recrystallization of ferrite in the FM microstructure relative to the FB and FP microstructures.

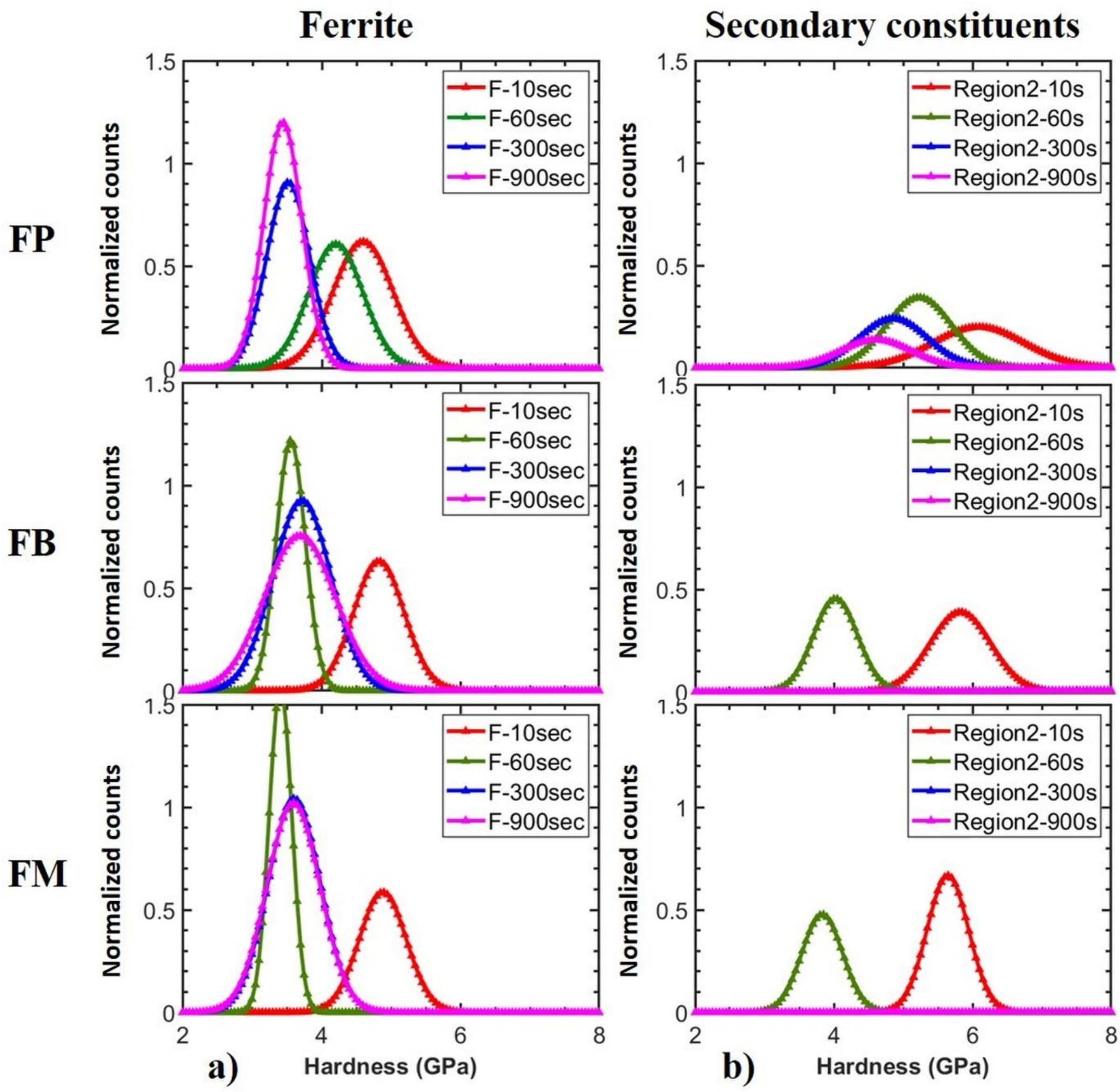

Figure 6-15: Hardness histograms of (a) ferrite and (b) secondary constituent in FP, FB and FM during recrystallization annealing at 725ºC.

6.5 Summary and conclusions:

Through a correlative characterization using electron microscopy and nanoindentation mapping, this chapter examines the impact of initial microstructure on the recrystallization annealing response of ferrite-pearlite, ferrite-bainite, and ferrite-martensite dual phase steels.

1. To investigate the recrystallization behavior of dual-phase steels with a nominal composition of DP600 but varying initial microstructures comprising ferrite-pearlite

(FP), ferrite-bainite (FB), and ferrite-martensite (FM), an isothermal annealing treatment was conducted at 725 °C, a temperature below the AC1 threshold. Preceding this, the samples underwent 80% cold rolling.

2. In the case of FP, the deformed microstructure as observed from SEM and KAM analysis was retained up to 60s of soaking followed by gradual recrystallization of the ferrite and spheroidization of the cementite in pearlite. In contrast, the FB and FM samples retained the deformed microstructure up to 10s followed by fast recrystallization by 60s. Further soaking resulted in formation of carbides at the ferrite grain boundaries.
3. The hardness maps obtained by nanoindentation showed excellent agreement with the microstructure during all stages of recrystallization. In the case of FP, the hardness increased during the initial stages of annealing (< 60s) in ferrite and pearlite due to bake-hardening like phenomena, followed by a gradual decrease due to recrystallization of ferrite and spheroidization of cementite as observed from the microstructure. In contrast, in the case of ferrite in FB and FM, the hardness is high up to 10s followed by a drastic drop confirming the microstructural observations. Also, the hardness of the secondary constituent in these cases drops due to carbide dissolution.
4. The micro-Vickers hardness measurements show a trend similar to nanoindentation although without showing the distinction between the constituents.
5. Overall, the recrystallization kinetics are faster in FM compared to FB and FP. This can be attributed to the higher defect density inherent in the FM microstructure, further enhanced by the 80% deformation acting as a potent driving force or reservoir of higher stored energy for faster ferrite recrystallization.

6.6 References:

[1] J.J. Roa, P. Sudharshan Phani, W.C. Oliver, L. Llanes, Mapping of mechanical properties at microstructural length scale in WC-Co cemented carbides: Assessment of hardness and elastic modulus by means of high speed massive nanoindentation and statistical analysis, Int. J. Refract. Met. Hard Mater. 75 (2018) 211–217. https://doi.org/10.1016/j.ijrmhm.2018.04.019.

[2] N. Fonstein, Dual-phase steels, 2017. https://doi.org/10.1016/B978-0-08-100638-2.00007-9.

[3] S.S. Shivathaya, Material design in steel making utilising mathematical modelling, knowledge-based and fuzzy logic approaches Recommended Citation, (1997). http://ro.uow.edu.au/theses/1586.

[4] J.N. Hall, J.R. Fekete, 2. Steels for auto bodies: a general overview, Elsevier Ltd, 2017. https://doi.org/10.1016/B978-0-08-100638-2.00002-X.

[5] Oxford Instruments, Electron Backscatter Diffraction - EBSD, Elsevier Ltd, n.d. https://nano.oxinst.com/products/ebsd/.

[6] J. Drillet, V. Hébert, P. Maugis, rolled advanced high-strength steels : In situ synchrotron X-ray di ff raction and modeling, Mater. Charact. 154 (2019) 20–30. https://doi.org/10.1016/j.matchar.2019.05.020.

[7] B. Bandi, J. Van Krevel, P. Srirangam, Interaction Between Ferrite Recrystallization and Austenite Formation in Dual-Phase Steel Manufacture, Metall. Mater. Trans. A Phys. Metall. Mater. Sci. 53 (2022) 1379–1393. https://doi.org/10.1007/s11661-022-06597-2.

[8] B. Sunil, S. Rajanna, Evaluation of mechanical properties of ferrite - martensite DP

steels produced through intermediate quenching technique, SN Appl. Sci. 2 (2020) 1–8. https://doi.org/10.1007/s42452-020-03246-4.

[9] H. Azizi-alizamini, M. Militzer, W.J. Poole, Formation of Ultrafine Grained Dual Phase Steels through Rapid Heating, 51 (2011) 958–964.

[10] Y.G. Deng, Y. Li, H. Di, Y.G. Deng, S. Key, W. Road, Y. Li, H. Di, E. Paso, E. Paso, Effect of Heating Rate during Continuous Annealing on Microstructure and Mechanical Properties of High-Strength Dual-Phase Steel, (2019) 3–11. https://doi.org/10.1007/s11665-019-04253-2.

[11] M. Kulakov, W.J. Poole, M. Militzer, The Effect of the Initial Microstructure on Recrystallization and Austenite Formation in a DP600 Steel, (2013). https://doi.org/10.1007/s11661-013-1721-z.

[12] D.Z. Yang, E.L. Brown, D.K. Matlock, G. Krauss, Ferrite Recrystallization and Austenite Formation in Cold-Rolled Intercritically Annealed Steel, 16 (1985).

[13] B. Bandi, J.V.A.N. Krevel, N. Aslam, ADVANCED HIGH-STRENGTH STEELS FOR AUTOMOBILES A Model and Experimental Validation to Predict Heating Rates for Overlap Between Ferrite Recrystallization and Austenite Transformation in Dual Phase Steel Manufacture, JOM. (2019). https://doi.org/10.1007/s11837-019-03358-2.

[14] K. Mukunthan, E.B. Hawbolt, Modeling Recovery and Recrystallization Kinetics in Cold-Rolled Ti-Nb Stabilized Interstitial-Free Steel, (n.d.).

[15] A.K. Rana, S.K. Paul, P.P. Dey, Effect of Martensite Volume . raction on Strain Partitioning Behavior of Dual Phase Steel, 21 (2018) 333–340. https://doi.org/10.1134/S1029959917040070.

[16] J. Kang, Y. Ososkov, J.D. Embury, D.S. Wilkinson, Digital image correlation studies for microscopic strain distribution and damage in dual phase steels, 56 (2007) 999–1002. https://doi.org/10.1016/j.scriptamat.2007.01.031.

[17] A. Varshney, S. Sangal, K. Mondal, Strain Partitioning and Load Transfer in Constituent Phases in Dual-Phase Steels, J. Mater. Eng. Perform. (2016). https://doi.org/10.1007/s11665-016-2196-z.

[18] P. Li, J. Li, Q. Meng, W. Hu, D. Xu, Effect of heating rate on ferrite recrystallization and austenite formation of cold-roll dual phase steel, J. Alloys Compd. 578 (2013) 320–327. https://doi.org/10.1016/j.jallcom.2013.05.226.

[19] S. Janakiram, P.S. Phani, G. Ummethala, H.V. Jagdeesh, S.K. Malladi, J. Gautam, L.A.I. Kestens, Insights on early recovery kinetics in ferrite - pearlite cold rolled high strength sheet steels, Mater. Charact. 193 (2022). https://doi.org/10.1016/j.matchar.2022.112332.

[20] S. Janakiram, P.S. Phani, G. Ummethala, S.K. Malladi, J. Gautam, L.A.I. Kestens, New insights on recovery and early recrystallization of ferrite-pearlite banded cold rolled high strength steels by high speed nanoindentation mapping, Scr. Mater. 194 (2021) 113676. https://doi.org/10.1016/j.scriptamat.2020.113676.

[21] P. Sudharshan Phani, W.C. Oliver, A critical assessment of the effect of indentation spacing on the measurement of hardness and modulus using instrumented indentation testing, Mater. Des. 164 (2019) 107563. https://doi.org/10.1016/j.matdes.2018.107563.

[22] J.-Y. Kang, D.-I. Kim, H.-C. Lee, Texture Development in Low Carbon Sheet Steels for Automotive Application, Microstruct. Texture Steels. (2009) 85–101. https://doi.org/10.1007/978-1-84882-454-6_5.

[23] C.W. Price, COMMENTS ON KINETIC MODELS FOR RECRYSTALLIZATION C., Scr. Mater. 19 (1985) 669–673.

[24] T. Ogawa, H. Dannoshita, Y. Adachi, K. Ushioda, Effect of initial microstructures prior to cold-rolling and intercritical annealing on ferrite recrystallization and ferrite-to-austenite phase transformation in Nb bearing low-carbon steels Effect of initial microstructures prior to cold-rolling and inte, J. Phys. Conf. Ser. (2019). https://doi.org/10.1088/1742-6596/1270/1/012016.

[25] B. Bandi, J. van Krevel, N. Aslam, P. Srirangam, A Model and Experimental Validation to Predict Heating Rates for Overlap Between Ferrite Recrystallization and Austenite Transformation in Dual Phase Steel Manufacture, Jom. 71 (2019) 1386–1395. https://doi.org/10.1007/s11837-019-03358-2.

Chapter 7 Effect of intercritical annealing on the microstructure and mechanical properties of dual phase steels with different initial microstructures

In this chapter, we explore the impact of the initial microstructure on the formation and characteristics of dual-phase (DP) steel subjected to different intercritical annealing durations. The intercritical annealing was carried out at 770ºC after a heating rate of 185°C/s, and the soaking time was varied. Microstructural changes were analysed using Field Emission Scanning Electron Microscopy (FESEM) and Electron Backscatter Diffraction (EBSD). Mechanical properties were characterized through Vickers microhardness testing, and local mechanical properties were investigated using nanoindentation technique. Excellent correlation between the microstructure and local mechanical properties was observed. The mechanisms underlying recrystallization and phase transformation during intercritical annealing were comprehensively analysed from the hardness of individual phases obtained from nanoindentation mapping.

7.1 Introduction:

Automotive industry has a strong demand for low carbon steels that provide a good combination of strength and ductility. This is because lighter cars use less fuel and produce less pollution [1]. To manufacture complex automotive parts good formability and high strength is required. Consequently, steels with combination of high strength & high ductility enables the fabrication of complex automotive components. Recent work in steel research has made it possible to improve the strength of steel without altering the formability.

Dual Phase steels are a class of Advanced High Strength Steels which are attractive for automotive industry as they are lower in cost and offer better mechanical properties [2–4]. The advantage of DP steel is that it has much higher ductility and strength as compared to other conventional steels. Therefore, they find applications in automotive body panels, wheels, and bumpers [5]. Typically, the dual phase microstructure is obtained by heating the specimen to intercritical range i.e., temperature between Ac1 and Ac3 followed by quenching. They contain 20-25 % of martensite along with a matrix of ferrite. In DP steels, strength or load carrying capacity is controlled by hard martensite phase and ductility or formability is controlled by the soft ferrite phase [6]. Additionally, cold rolling imparts higher stored stain energy and in intercritical temperature range it suppresses the recovery [7,8] and changes the recrystallization and austenite formation temperature [9–11]. According to Huang et al. [11], austenite production during heating is retarded in Fe-C-Mn-Si steel with ferrite-pearlite microstructure when the heating rate is increased from 1°C/s to 100°C/s. Philippot et al. [12] did note that the austenite volume percentage generated during heating is hardly affected by raising the heating rate from 1°C/s to 10°C/s. Austenite islands arise as a result of intercritical annealing and eventually transform to martensite. The distribution of the ensuing martensite in the microstructure is determined by the morphology and distribution of the austenite during intercritical annealing[13], which ultimately influences the dual phase steel's microstructure and mechanical properties [14–16]. Also, the effect of initial rolling above the austenite recrystallization temperature (TnR) and its subsequent effect on cold rolling texture before intercritical annealing is important to consider and has been reported by Gautam et.al. [17]. However, a systematic study involving the effect of different initial dual phase microstructures such as ferrite-pearlite (FP), ferrite-bainite (FB) and ferrite-martensite (FM) on the intercritical annealing behaviour for a fixed composition of carbon is not reported.

Hence, this chapter aims to explore the influence of prior thermomechanical processing on the intercritical annealing response. To this end, different initial microstructures are obtained by various prior processing steps such as hot rolling, coiling and cold rolling. Using a combination of electron microscopy and nanoindentation mapping, the intercritical annealing response for these samples at various soaking times is investigated, and microstructure-property correlations at the micrometer length scale are assessed.

7.2 Experimental Procedure:

7.2.1 Processing:

The initial dual phase microstructures were obtained by hot rolling, coiling, and then cold rolling to 80% reduction, as was covered in chapter 3. A heating rate of 185°C/s was used to reach the intercritical annealing temperature of 770°C followed by different soaking durations. To achieve the dual phase microstructure, the soaking duration was varied between 60s and 900s followed by water quenching.

7.2.2 Microstructural and mechanical characterization:

The specimen's microstructure was analysed using electron backscattered diffraction (EBSD) and a field emission scanning electron microscope (FESEM Model: FEI - NOVA NANOSEM450). The samples were polished using conventional metallographic polishing techniques, as covered in Chapter 3. EDAX OIM software was used to analyse the EBSD data. A Vickers hardness tester was used to determine the specimen's bulk hardness. Using a high-speed nanoindentation technique, the local mechanical characteristics were assessed. Each map had 3600 indents in a 60X60 grid pattern with a spacing of 1 µm and a maximum depth of 100 µm [18].

7.3 Results:

7.3.1 Initial microstructures:

Fig. 7-1 shows the microstructure of the specimens with different dual phase constituents that were subjected to 80% cold rolling. The ferrite-pearlite (FP) sample, shown in Fig. 7-1(a), has a banded structure with elongated ferrite (darker grey) and pearlite (the light grey) grains that are aligned along the rolling direction. The ferrite-bainite (FB) microstructure is shown in Fig. 7-1(b), that shows severe distortion and alignment of the ferrite phase along the deformation direction, while the bainite underwent significant fragmentation and dispersion throughout the ferrite matrix. Unlike the pearlite, which formed clear bands, the bainite had a more uniform distribution in the microstructure. Fig. 7-1(c) shows the ferrite-martensite (FM) microstructure, which has a more refined and elongated ferrite phase and a more uniform and dispersed martensite phase (light grey). A detailed discussion on the cold rolled microstructures are presented in chapter 5.

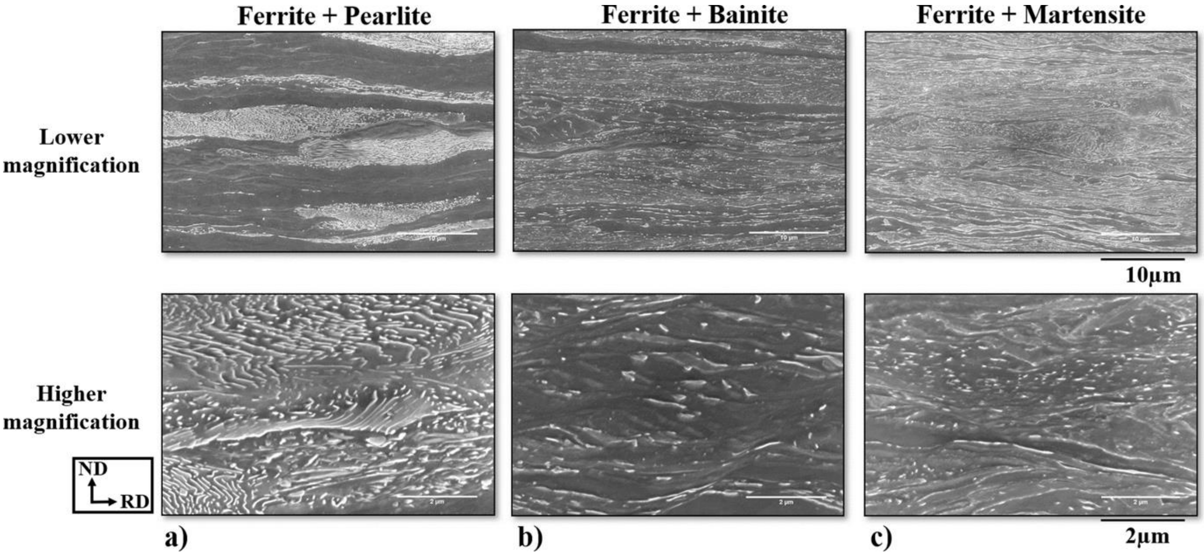

Figure 7-1: SEM micrographs after 80% cold rolling, accompanied by their higher magnification images, for (a) FP, (b) FB, and (c) FM.

7.3.2 Microstructural evolution during intercritical annealing at 770ºC:

The samples with different initial microstructures that are subjected to 80% cold rolling undergo intercritical annealing at 770ºC. This annealing process uses a salt bath furnace with a high heating rate of 185ºC/s and a holding time before water quenching to obtain a dual phase microstructure. Fig. 7-2 shows the microstructures after different intercritical annealing durations starting from different initial microstructures labelled as FP, FB and FM. In the case of FP samples, the micrographs reveal the martensite formation in the pearlitic regions and the banding effect is evident even after transformation. Ferrite recrystallization can also be observed. For FB and FM samples, martensitic transformation is less compared to FP in the initial stage. However, a higher degree of ferrite recrystallization can be observed. The necklace-type morphology of martensite was found in the FB and FM samples, whereas in the FP sample, banded morphology was observed.

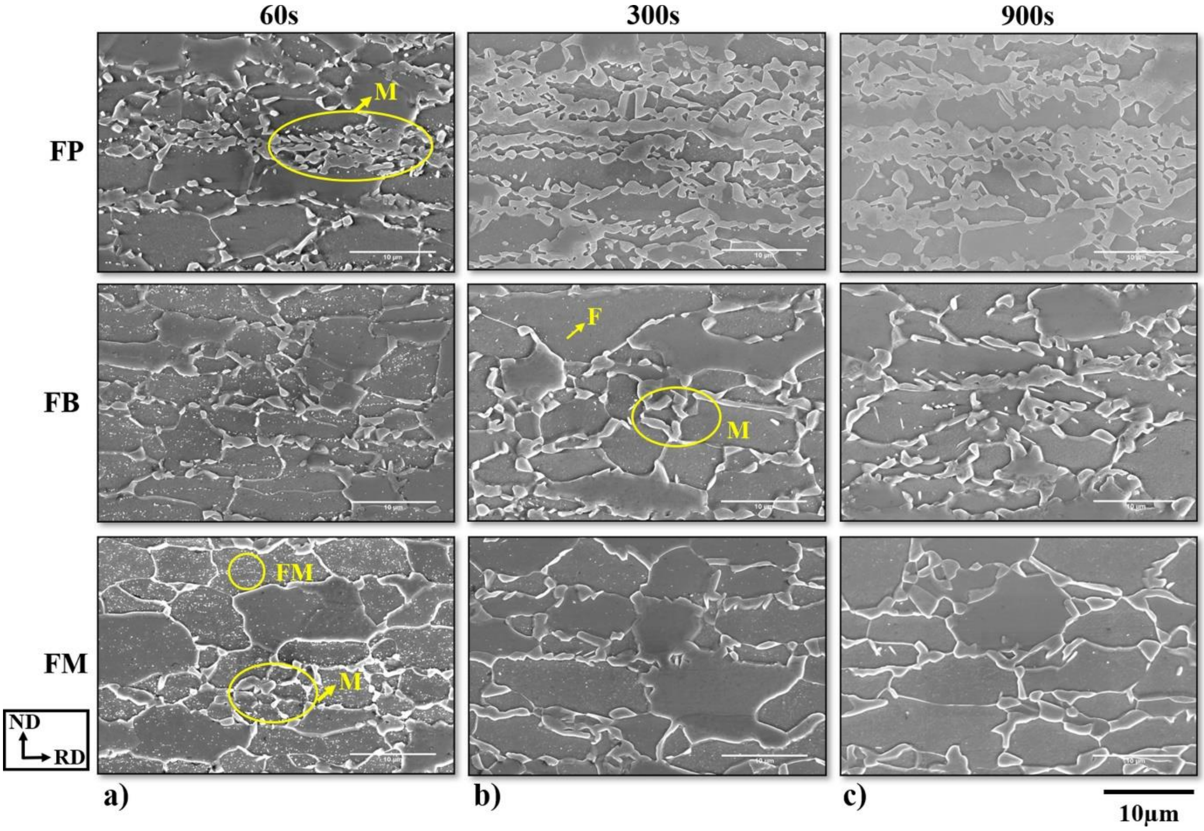

Figure 7-2: SEM micrographs after intercritical annealing at 770ºC for (a) 60s, (b) 300s, and (c) 900s in case of samples with initial microstructure consisting of FP, FB and FM.

7.3.3 Martensite volume fraction and ferrite grain size:

The martensite volume fraction and ferrite grain size as a function of soaking time are shown in Fig. 7-3. The ferrite grain size and the martensite volume fraction were measured using optical micrographs and SEM micrographs, respectively. The plot shows that the extent of austenite-to-martensite transformation and ferrite grain refinement increases with the soaking duration. The FP sample shows a higher martensite fraction compared to the others due to the slower recrystallization of FP presented in chapter 6, which leads to a faster austenite transformation. Concurrently, this also leads to a finer ferrite grain size in FP due to the faster transformation compared to FB and FM.

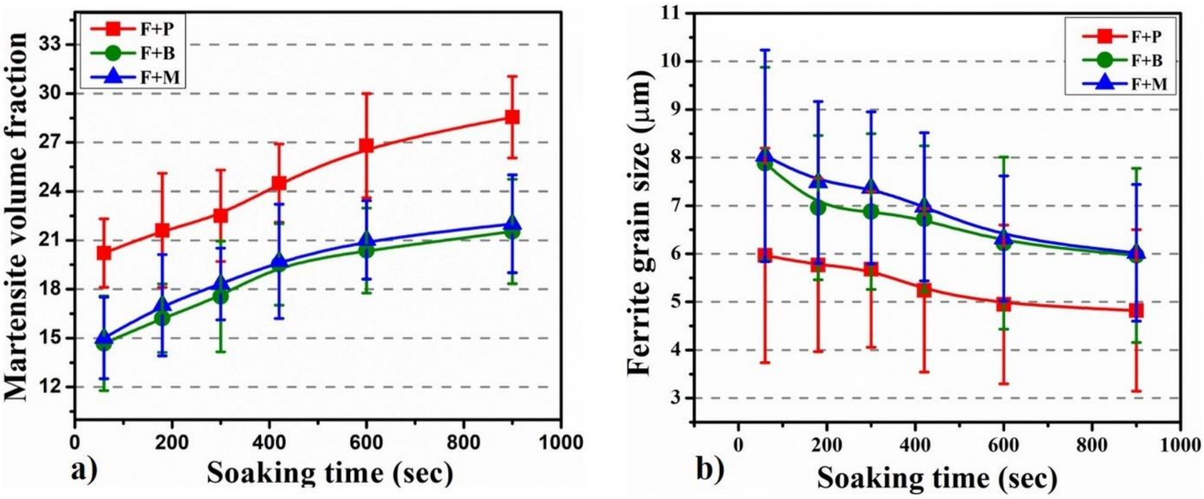

Figure 7-3: (a) Martensite volume fraction and (b) ferrite grain size after intercritical annealing at 770°C for different soaking durations in case of FP, FB and FM.

7.3.4 Microstructural evolution observed using EBSD: IQ maps

EBSD analysis was carried out on the intercritically annealed samples to further investigate the microstructure and local misorientations. As explained in the chapter 3, standard EBSD techniques cannot easily differentiate between martensite and ferrite phases. Here we use the IQ maps to analyze the microstructure. Fig. 7-4 shows the image quality (IQ) maps obtained from EBSD, after intercritical annealing for different durations of 60s, 300s, and 900s for the different initial microstructures. The contrast observed in a IQ maps is due to the combination of several factors including phase, topography, strain, grain boundary, etc. [19]. In the figure, the lower IQ regions correspond to martensite, whereas the higher IQ parts (bright regions) correspond to ferrite [20]. The IQ maps clearly show that FP samples have more martensite (darker regions) compared to FB and FM. Also, the banded morphology of the microstructure in FP is retained even after transformation, whereas in FB and FM, martensite is observed at ferrite grain boundaries.

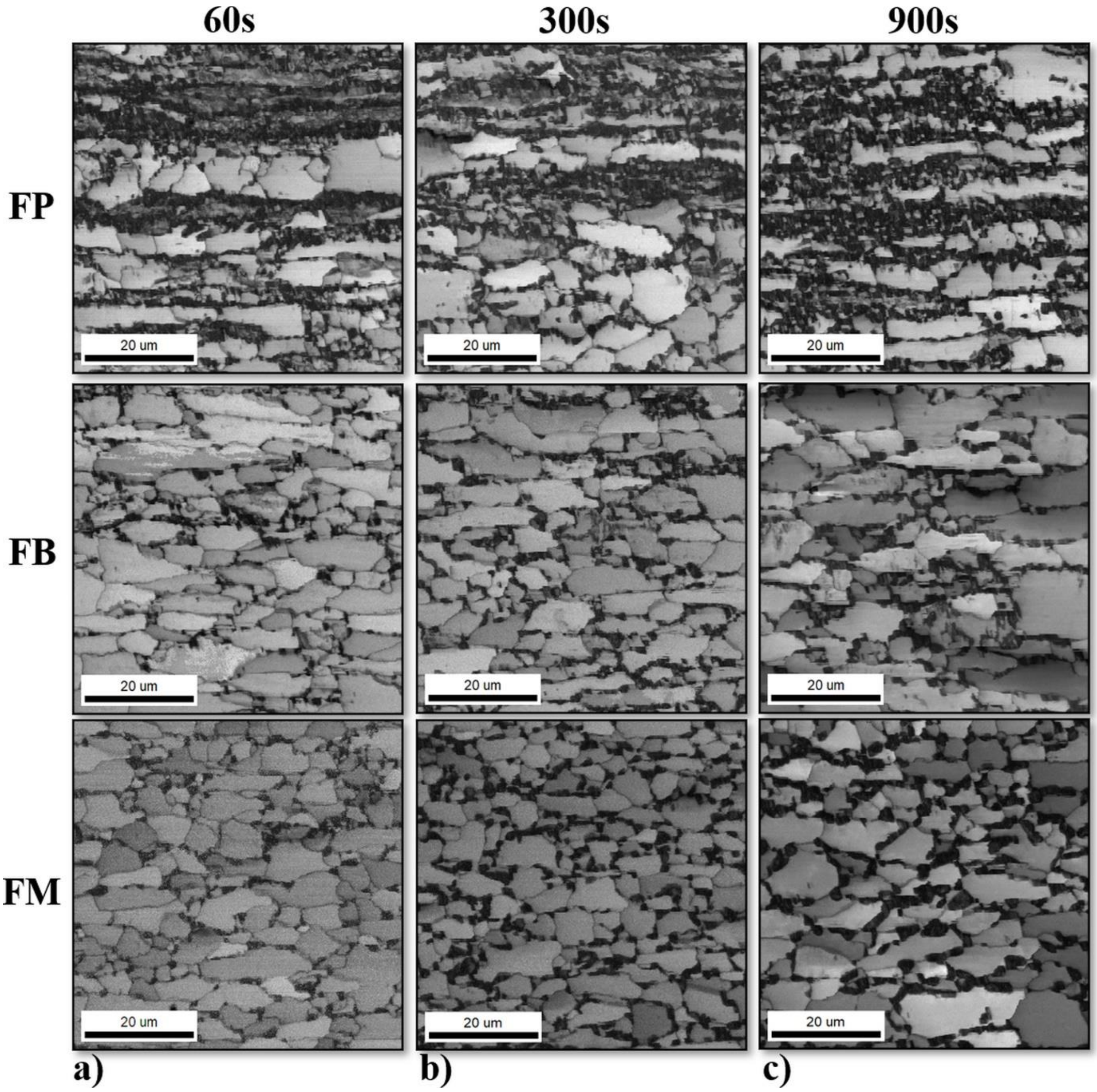

Figure 7-4: Image Quality maps after intercritical annealing at 770ºC for (a) 60s, (b) 300s, and (c) 900s in case of samples with initial microstructure consisting of FP, FB and FM.

7.3.5 Microstructural evolution observed using EBSD: KAM maps

To further analyze the microstructure especially for the local defect distribution, Kernel Average Misorientation (KAM) serves as a crucial parameter in providing a quantitative measure of local misorientation between a point and its neighboring points. In the intercritical annealing regime, phase transformation and ferrite recrystallization both operate and KAM analysis helps in investigating diverse facets such as strain localization, defect distribution, and grain boundary characterization. Figure 7-5 shows the spatial distribution of KAM (5th neighbor, < 3° threshold) for intercritically annealed samples subjected to varying soaking times. The observed misorientation levels across all samples exhibit distinct patterns for the different soaking durations. Notably, in the case of FP, a higher misorientation is evident, attributable to a higher martensite volume fraction. Conversely, lower misorientation levels are observed in FB and FM. With increasing soaking time, a concurrent rise in martensite volume fraction is noted, manifesting as elevated misorientation in the same region. This observation aligns well with the microstructure presented in Fig. 7-2 & 7-4. These findings clearly imply that transformation kinetics are faster in FP, compared to FB and FM. It may be noted that this trend is opposite to the recrystallization kinetics presented in chapter 6. This implies that the recrystallization and transformation compete at these annealing temperatures (725 and 770ºC) and one of them dominates at the cost of the other. It may also be recalled that the recrystallization kinetics are faster in FB and FM due to the higher stored energy (defect density) in those samples.

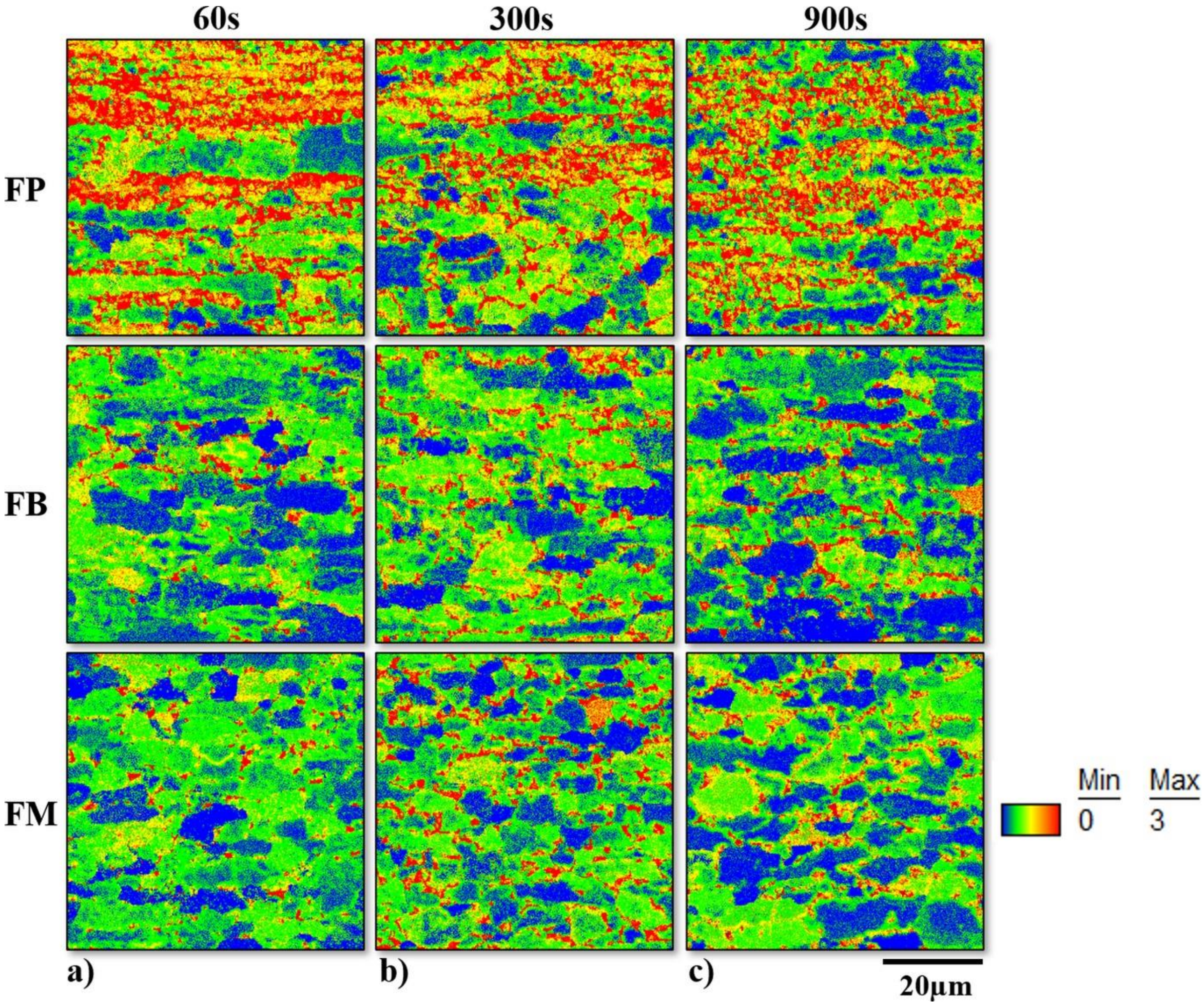

Figure 7-5: KAM maps after intercritical annealing at 770ºC for (a) 60s, (b) 300s, and (c) 900s in case of samples with initial microstructure consisting of FP, FB and FM.

7.3.6 Microstructural evolution observed using EBSD: KAM histograms

To quantify the KAM maps shown in Fig. 7-5, KAM histograms are plotted as shown in Fig. 7-6. The histograms prior to intercritical annealing (80% cold rolled) are also shown for comparison. All the samples show a clear decrease in misorientation with intercritical annealing, indicating recrystallization and transformation. While the role of individual phases cannot be commented from these histograms without partitioning, it can be reasonably concluded that ferrite recrystallization has occurred during intercritical annealing. Also, a slight rightward shift in peak position from 60s to 900s is observed in FP sample possibly due to the higher martensite formation. In the case of FB and FM, the misorientations remain constant after the initial drop.

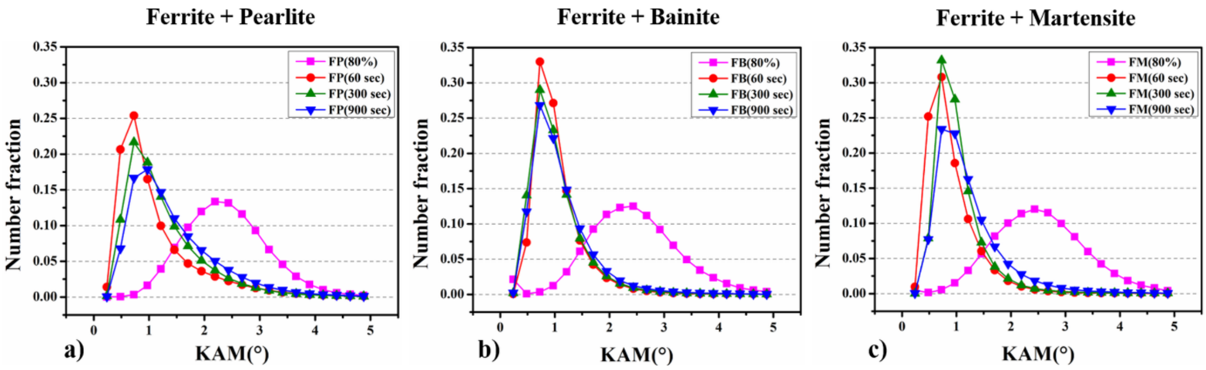

Figure 7-6: Kernel average misorientation distribution after different soaking duration during intercritical annealing of samples with initial microstructure consisting of (a) FP (b) FB and (c) FM.

7.3.7 Micro hardness evolution:

Micro hardness testing was carried out on all materials subsequent to cold rolling and intercritical annealing for different soaking times, as shown in Fig. 7-7. Initially, after 80% cold rolling, FM exhibited the highest hardness compared to FB and FP. The elevated hardness is attributed to grain refinement, fragmentation, increased defect density, and strain accumulation. After intercritical annealing, the hardness of all the samples increases from an initial low value, due to the continuous formation of martensite. It may be noted that the hardness of FP is higher than FB and FM at all times during annealing. As mentioned earlier, in FB and FM, ferrite recrystallization is faster, resulting in significant reduction in hardness compared to FP in the beginning. In contrast, the FP samples show higher hardness initially due to lower extent of recrystallization and higher hardness with increasing soaking time in the intercritical regime due to the higher martensite volume fraction. Overall, a clear trend in hardness is observed with increasing martensite volume fraction.

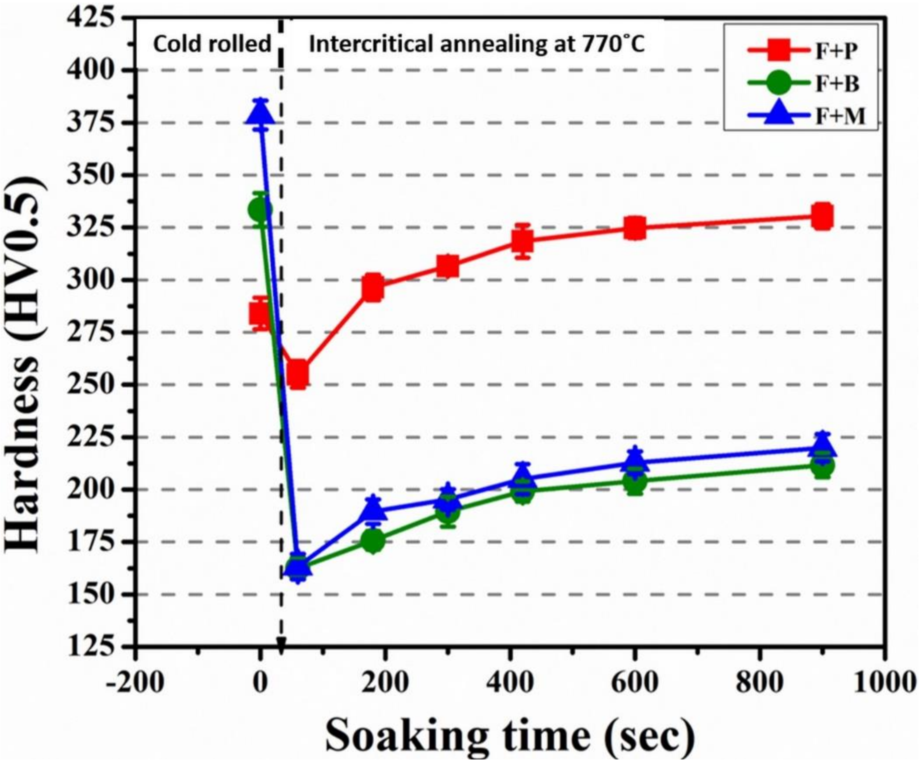

Figure 7-7: Vickers hardness after intercritical annealing at 770ºC for different durations in case of initial microstructures consisting of FP, FB and FM.

7.3.8 Nanoindentation hardness mapping:

To further investigate the local variations in hardness high speed nanoindentation mapping is used. Fig. 7-8 shows the hardness maps in the cold rolled and intercritically annealed states after different soaking durations. The hardness map shows two different regions with noticeable hardness difference in almost all cases. The region with lower hardness (blue) corresponds to ferrite, while the region with higher hardness (red) corresponds to second-phase component which is predominantly martensite. It may be noted that the length scale of the martensite is small and comparable to the indent spacing of 1 μm and hence it is possible that its hardness is affected by the surrounding ferrite.

In the case of FP, in the cold-rolled condition, a notable hardness difference between ferrite and pearlite is evident. Upon annealing at 770ºC in the intercritical regime, where ferrite and austenite coexist, immediate quenching results in martensite formation with elevated hardness compared to ferrite. This transformation is reflected in the hardness map, wherein an increase in soaking time results in higher hardness regions with a largely banded morphology corresponding to martensite. For FB and FM in the cold-rolled condition, higher hardness is observed, especially in the ferrite regions compared to FP, which drives recrystallization of ferrite during intercritical annealing, leading to lower hardness in the matrix. As discussed earlier, this concurrently reduces the driving force for austenite and thereby martensite formation and hence, the higher hardness regions corresponding to martensite are less compared to FP. Overall, the nanoindentation results effectively captured variations in hardness, encompassing the impact of prior deformation and different soaking durations during intercritical annealing. The observed hardness outcomes are in excellent agreement with the microstructural and Kernel Average Misorientation (KAM) analyses presented earlier.

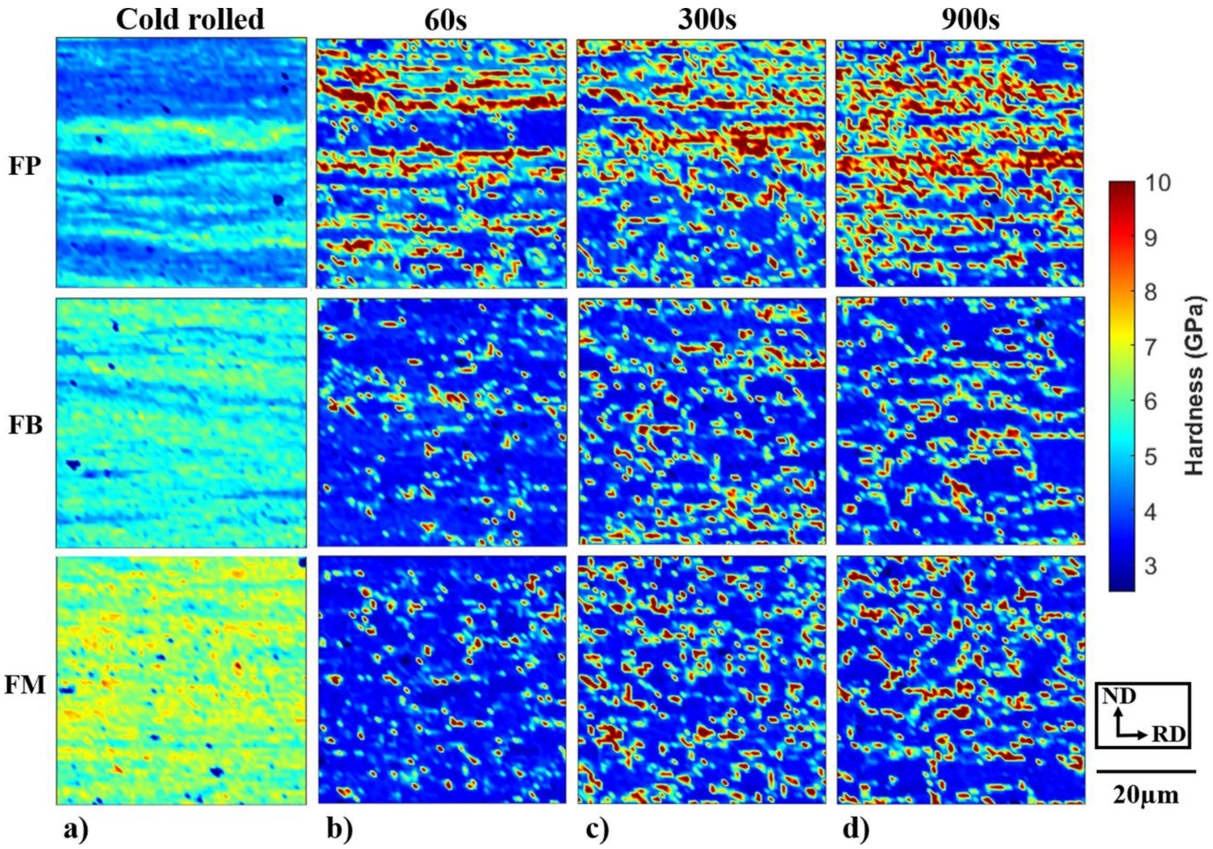

Figure 7-8: Nanoindentation maps for different initial microstructures (FP, FB and FM) after (a) cold rolling, and intercritical annealing at 770ºC for (b) 60s (c) 300s and (d) 900s.

7.3.9 Nanoindentation hardness data histogram

In order to further quantify the hardness maps shown in Fig. 7-8 and quantify the hardness evolution during intercritical annealing, the hardness histograms for the different initial microstructures are shown in Fig. 7-9, including the cold-rolled state. A clear reduction in hardness with intercritical annealing is observed in all cases which closely follows the trend observed in KAM histograms shown in Fig. 7-6. While these histograms show the combined effect of ferrite and martensite, it may be safely concluded that upon annealing the hardness of FB and FM immediately reduces due to ferrite recrystallization, whereas in the case of FP, the reduction is more gradual. To objectively analyse the competing processes of recrystallization and transformation, the hardness of individual phases is required. This will be presented and discussed in the next sub-section.

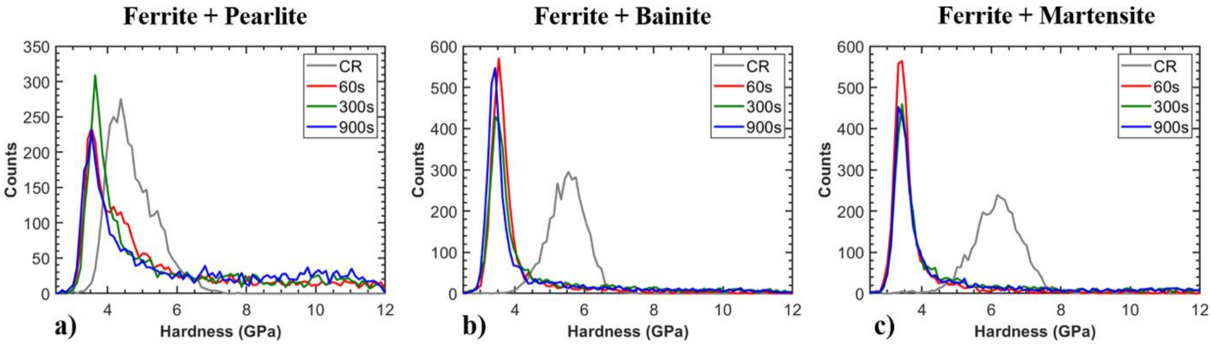

Figure 7-9: Hardness histograms of samples with initial microstructure consisting of a) ferrite-pearlite b) ferrite-bainite and c) ferrite-martensite after intercritical annealing at 770ºC for different soaking durations.

7.4 Discussion

7.4.1 Assessment of microstructure and mechanical properties at micrometer length scale during intercritical annealing of ferrite-pearlite steel (FP):

In this section, a direct comparison of the microstructure from SEM and the corresponding hardness map is presented for the different intercritical annealing durations as shown in Fig. 7-10 for FP. Excellent agreement between the microstructure and the hardness map can be observed with the ferrite regions showing lower hardness and the pearlite (in cold rolled) / martensite (annealed) regions showing higher values. Interestingly, the hardness maps also capture the morphology of the constituent phases as seen from the micrographs, The hardness maps not only capture the banded nature of the pearlite but also the martensite after transformation which also retains the banded morphology to a certain extent. Interestingly, the martensite at the ferrite boundaries is also well captured by the hardness map. As the resolution of the nanoindentation mapping is 1 µm, the finer constituent, which is martensite appears coarser in the hardness maps. With increasing soaking time, there is a rise in martensite volume fraction and a reduction in ferrite grain size, as discussed in section 7.3.3. The SEM micrographs shown here demonstrate the same, and the hardness map closely follows this trend as well.

To quantify the hardness changes of the individual constituents, the hardness maps are deconvoluted using the k-means clustering algorithm into two bins nominally corresponding to ferrite and martensite. Figure 7-10 also shows the deconvoluted map and the corresponding hardness histogram[21]. In the deconvoluted maps and histograms, blue color denotes ferrite, while red color (region 2) signifies secondary constituent, which is pearlite in cold rolled state and predominately martensite after intercritical annealing. The deconvoluted maps show good agreement with the SEM micrographs shown in Fig. 7-10. The hardness of pearlite in cold rolled state and martensite after intercritical annealing is higher than ferrite as expected. Interestingly, the hardness of ferrite shows only a slight reduction upon annealing even after prolonged soaking. The retention of hardness of ferrite upon annealing will be discussed in detail in section 7.4.4.

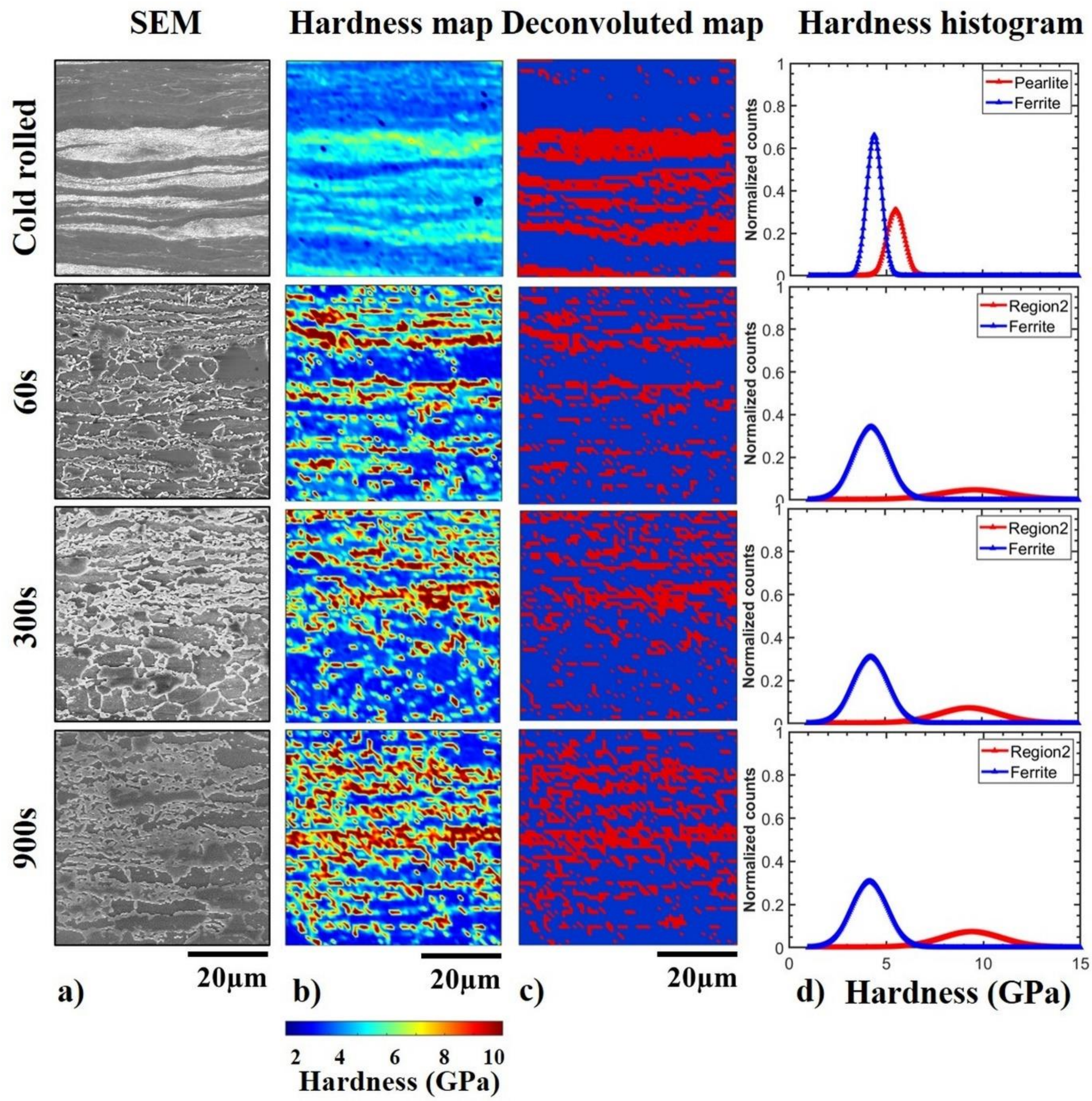

Figure 7-10: (a) SEM micrographs and corresponding (b) hardness maps, (c) deconvoluted hardness maps and (d) histograms after cold-rolling and intercritical annealing at 770ºC for 60s, 300s and 900s for samples with initial microstructure consisting of FP.

7.4.2 Assessment of microstructure and mechanical properties at micrometer length scale during intercritical annealing of ferrite-bainite steel (FB):

In this section we assess the microstructure-property correlations during intercritical annealing for cold rolled samples with initial microstructure consisting of ferrite-bainite. Fig. 7-11 shows the SEM micrographs and the corresponding hardness maps after cold rolling and after subsequent intercritical annealing. The deconvoluted maps and the hardness histograms are also shown. The plot clearly shows the excellent agreement between the microstructure and the local mechanical properties in all cases. The alignment of grains along rolling direction seen in the micrographs is also well captured by the hardness maps. Similarly, the martensite formed at the ferrite grain boundaries after transformation is also captured by the hardness maps. To further quantify the hardness data, deconvoluted maps are obtained by k-means clustering and they agree well with the SEM micrographs validating the deconvolution procedure. It may be noted that blue color in deconvoluted maps corresponds to ferrite, while red (region 2) corresponds to bainite/ferrite mixture in cold rolled state and martensite in annealed state. The histograms accordingly show the hardness difference between ferrite and bainite-ferrite mixture and martensite. The hardness of bainite and ferrite mixture in cold rolled state and martensite after intercritical annealing is higher than ferrite as expected. The hardness of martensite formed after transformation is more than that of the initial bainite. Unlike the case of FP, the hardness of ferrite decreases upon intercritical annealing which is similar to the observations during recrystallization annealing of FB presented in chapter 6.

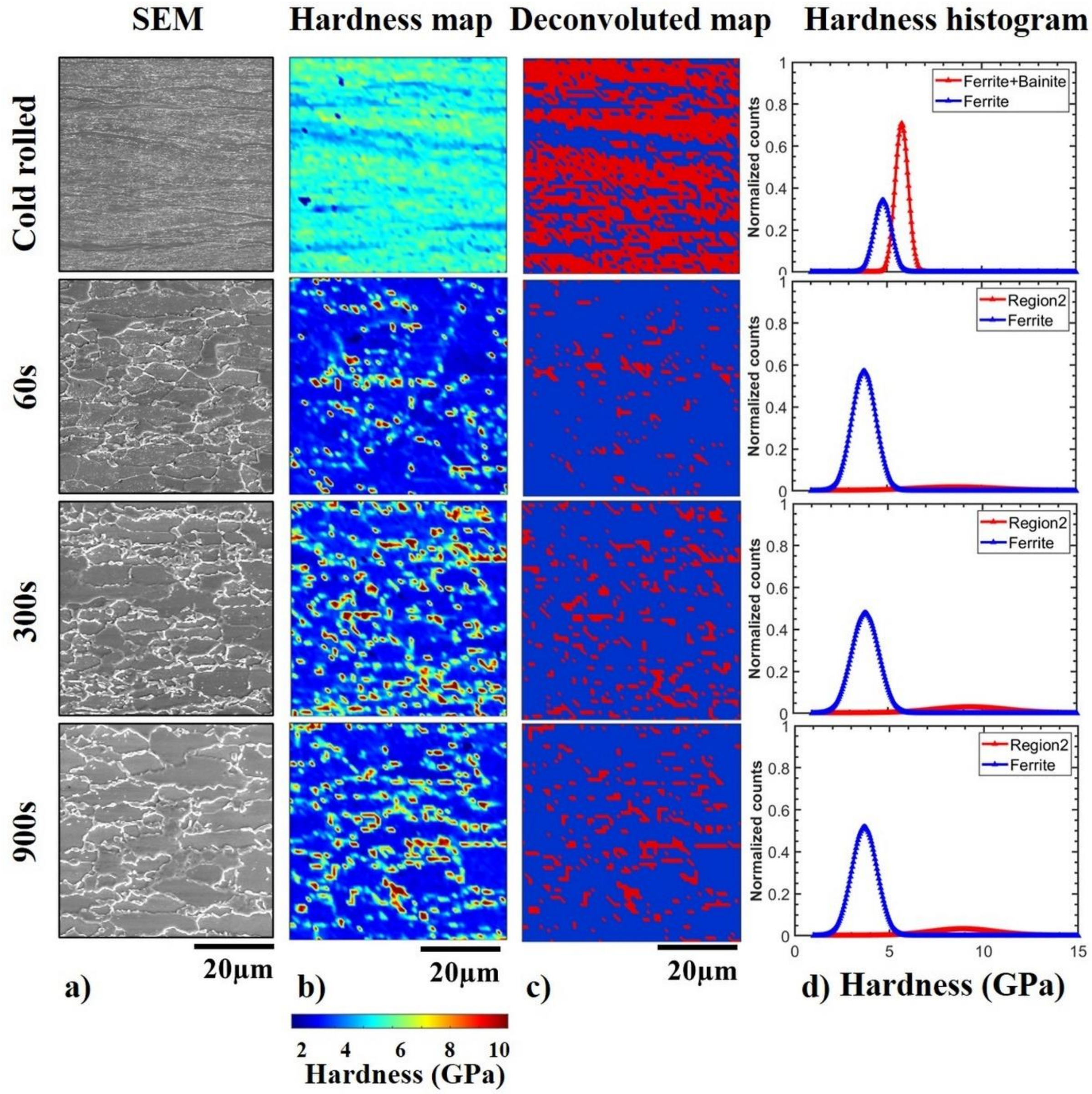

Figure 7-11: (a) SEM micrographs and corresponding (b) hardness maps, (c) deconvoluted hardness maps and (d) histograms after cold-rolling and intercritical annealing at 770°C for 60s, 300s and 900s for samples with initial microstructure consisting of FB.

7.4.3 Assessment of microstructure and mechanical properties at micrometer length scale during intercritical annealing of ferrite-martensite steel (FM):

Similar to the case of FP and FB presented earlier, here we assess the microstructure-property correlations during intercritical annealing for cold rolled samples with initial microstructure consisting of ferrite-martensite. Fig. 7-12 shows the SEM micrographs and the corresponding hardness maps after cold rolling and after subsequent intercritical annealing. The deconvoluted maps and the hardness histograms are also shown. As was the case with FP and FB, the plot clearly shows the excellent agreement between the microstructure and the local mechanical properties in all cases. The alignment of grains along rolling direction seen in the micrographs is also well captured by the hardness maps. The behaviour of FM samples after cold rolling and intercritical annealing, closely follows the trend observed in FB. The histograms accordingly show the hardness difference between ferrite and martensite. The hardness of martensite in cold rolled state and after intercritical annealing (region 2) is higher than ferrite as expected. The hardness of martensite formed after transformation is more than that of the initial martensite. This could be attributed to the fine distribution of martensite throughout the sample in the cold rolled state, wherein its measurement is affected by the neighbouring ferrite. The deconvoluted map in the cold rolled state clearly shows this aspect. Unlike the FP, the hardness of ferrite decreases after intercritical annealing.

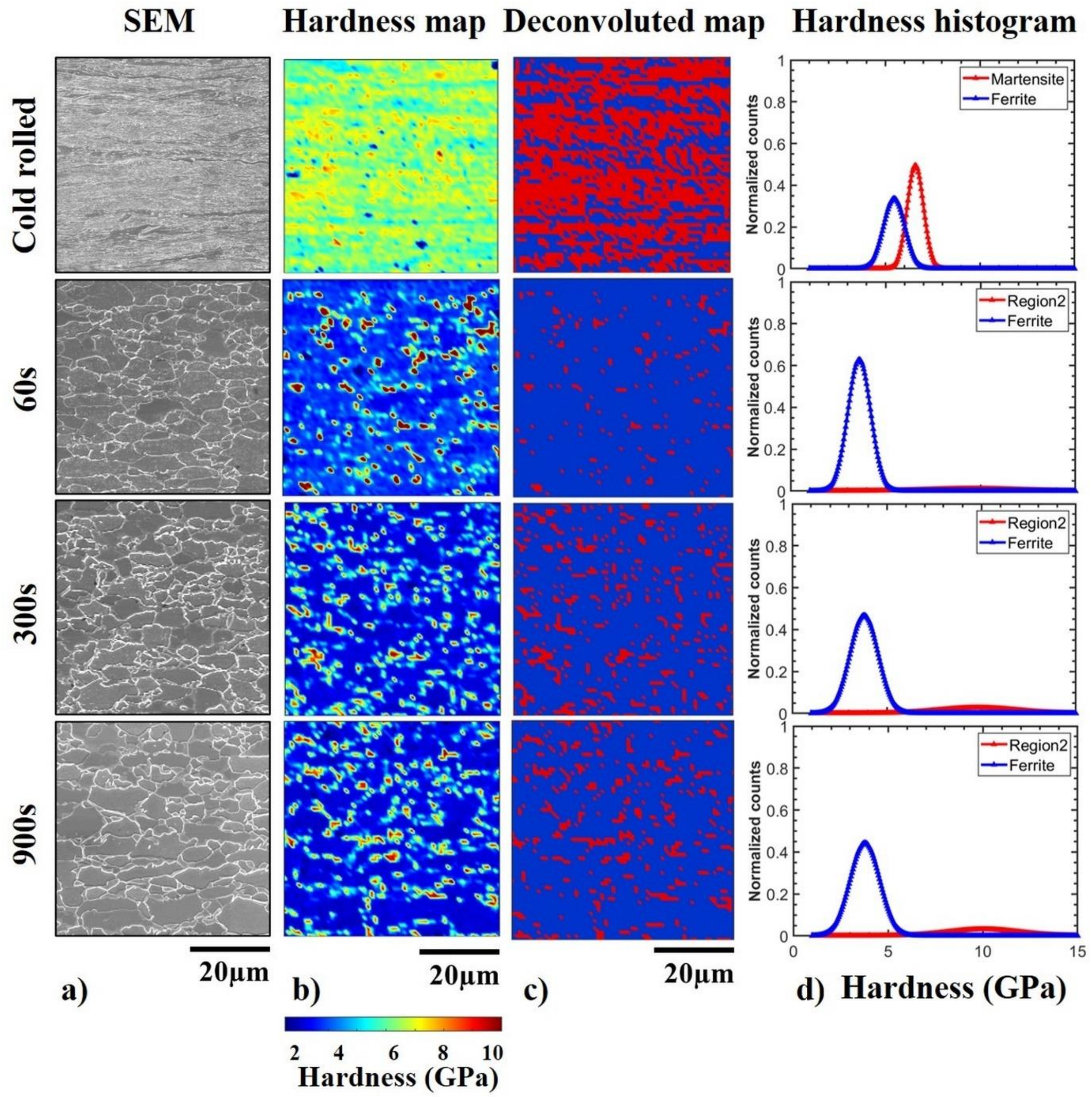

Figure 7-12: (a) SEM micrographs and corresponding (b) hardness maps, (c) deconvoluted hardness maps and (d) histograms after cold-rolling and intercritical annealing at 770^{o}C for 60s, 300s and 900s for samples with initial microstructure consisting of FM.

7.4.4 Impact of intercritical annealing on the local mechanical properties and microstructure of various dual phase steels

Fig. 7-13 shows the hardness histograms subsequent to intercritical annealing for different duration in samples with initial microstructures consisting of FP, FB, and FM. The hardness for ferrite matrix is shown in Fig. 7-13(a), whereas the secondary constituent is shown in Fig. 7-13(b). It may be noted that the secondary constituent in the cold rolled (CR) state is pearlite in FP, bainite-ferrite mixture in FB and martensite-ferrite mixture in FM, whereas the secondary constituent after intercritical annealing is predominantly martensite in all cases. In the case of ferrite of the FP sample, the hardness in the cold rolled state is retained even after annealing. However, a distinct broadening of the peak with annealing is observed. In contrast, the ferrite in FB and FM samples show a clear decrease with annealing, indicating ferrite recrystallization. The reasons for the apparent lack of significant recrystallization of ferrite in FP will be discussed later in this section. In the case of the secondary constituent, the area fraction of martensite is higher in the case of FP as was observed from the SEM micrographs. Also, a clear increase in the hardness upon intercritical annealing is evident. This indicates that the martensite formed upon quenching from the intercritical regime is harder than prior pearlite or bainite. Interestingly, the martensite obtained after intercritical annealing is harder than that obtained after coiling and cold working. This is in part due to the fine distribution of martensite throughout the sample in the prior cold rolled state, wherein its measurement is affected by the neighbouring ferrite. In summary, the deconvoluted hardness histograms show significant ferrite recrystallization in FB and FM and more austenite to martensite transformation in the case of FP. This can be attributed to higher stored energy in cold rolled FB and FM, driving recrystallization and consequently slowing down transformation, whereas the reverse is true for FP.

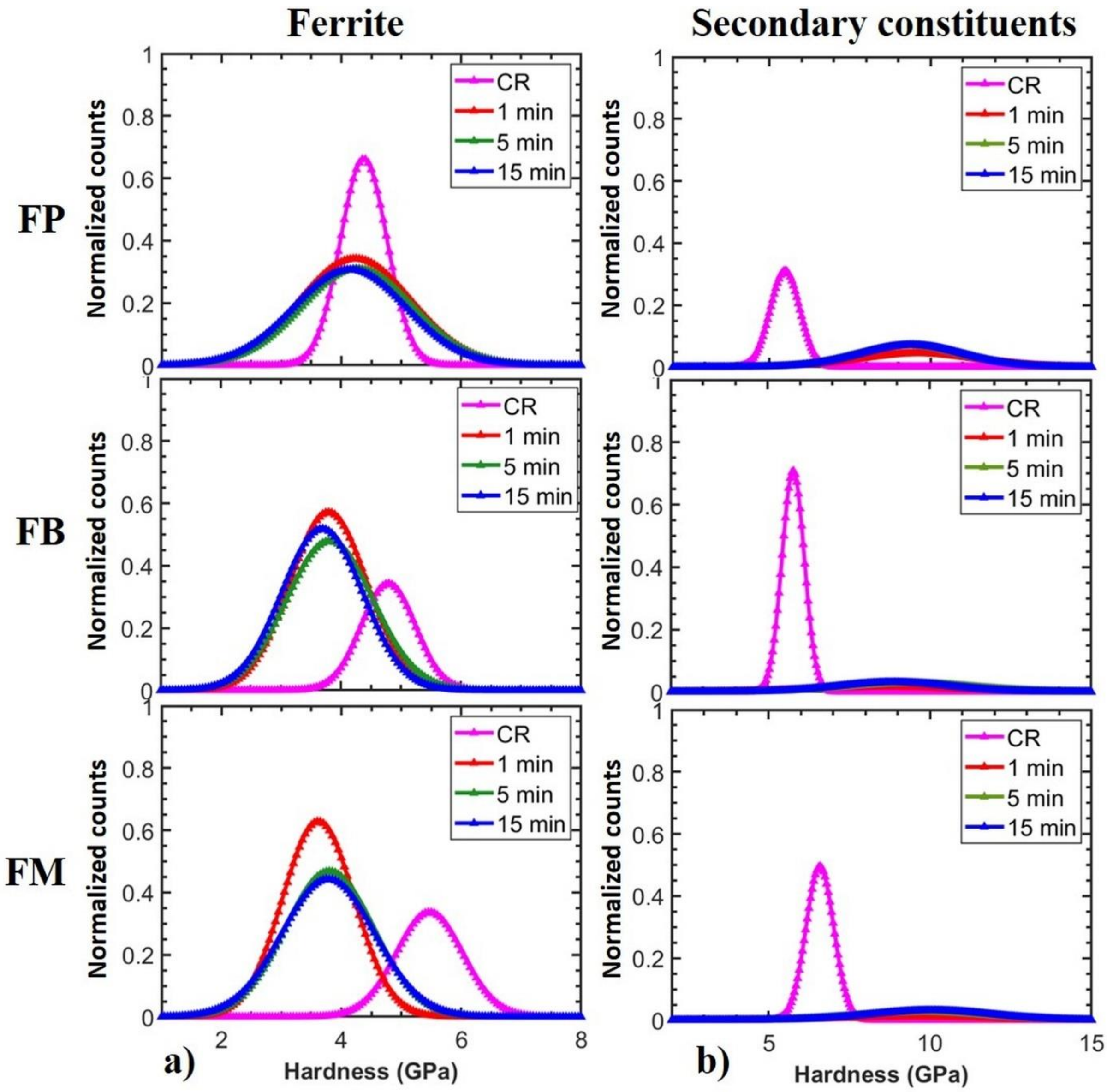

Figure 7-13: Hardness distribution of (a) ferrite and (b) secondary constituents in samples with initial microstructure consisting of FP, FB and FM after cold rolling and intercritical annealing to different durations.

At this juncture, it is instructive to examine why the hardness of ferrite in the FP sample is retained even after intercritical annealing, unlike the other samples. In this regard, the KAM maps provide a simple way to probe the extent of recrystallization at the local level. Fig 7-14, shows the etched SEM micrographs and the corresponding KAM and hardness maps after 1 min of soaking at the intercritical annealing temperature. Assuming that regions with <1° misorientation to be recrystallized, the KAM maps for FP clearly show that the extent of recrystallization shown by the blue coloured regions is much less compared to FB and FM. The corresponding hardness maps also show lower hardness in the recrystallized regions identifiable from the KAM maps and higher hardness in regions with greater misorientations.

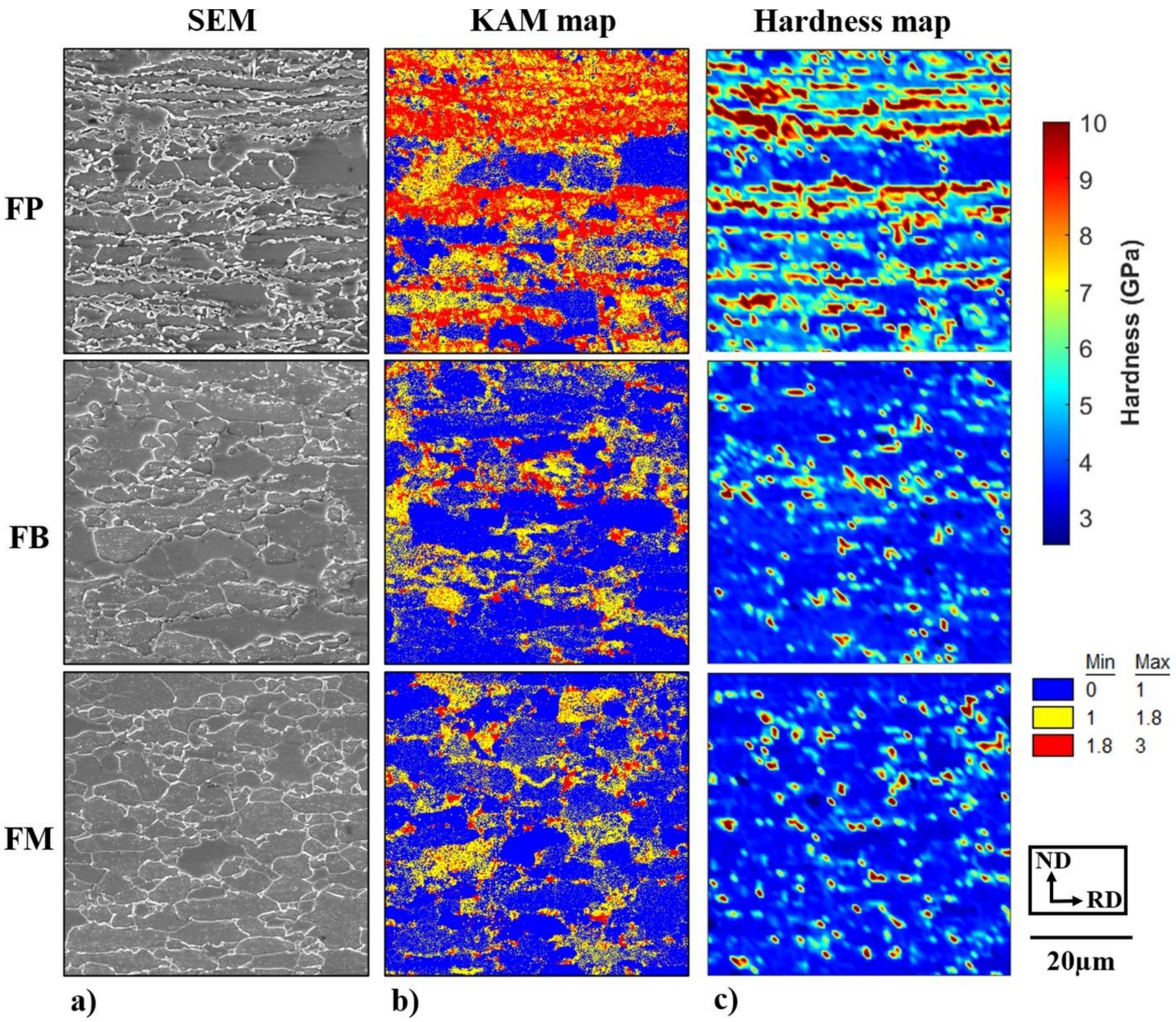

Figure 7-14: Comparison of (a) SEM micrographs, (b) KAM maps and (c) hardness maps after intercritical annealing for 1 min in samples with initial microstructure consisting of FP, FB and FM.

In order to quantitatively assess the correspondence between KAM and hardness, the KAM and hardness histograms are shown in Fig. 7-15 after 1 min of soaking time. The FB and FM samples show a predominant single peak at lower misorientation compared to the FP, which shows a second peak / shoulder at higher misorientation as was observed from the KAM maps. Interestingly, the hardness histograms show a similar trend, both in terms of the relative peak positions and shapes. This clearly establishes the one-one correspondence between KAM and hardness in this case. This implies that the broadening of the ferrite hardness peak with intercritical annealing of FP shown in Fig. 7-13(a) is due to the retardation of recrystallization in ferrite in many locations resulting in a mixture of recrystallized and unrecrystallized grains. Furthermore, as ferrite recrystallization and austenite transformation compete in this temperature range, the unrecrystallized regions promote faster austenite transformation and higher martensite formation in the case of FP. In contrast, the FB and FM samples recrystallize fast leading to reduced driving force for transformation and hence show slower transformation kinetics.

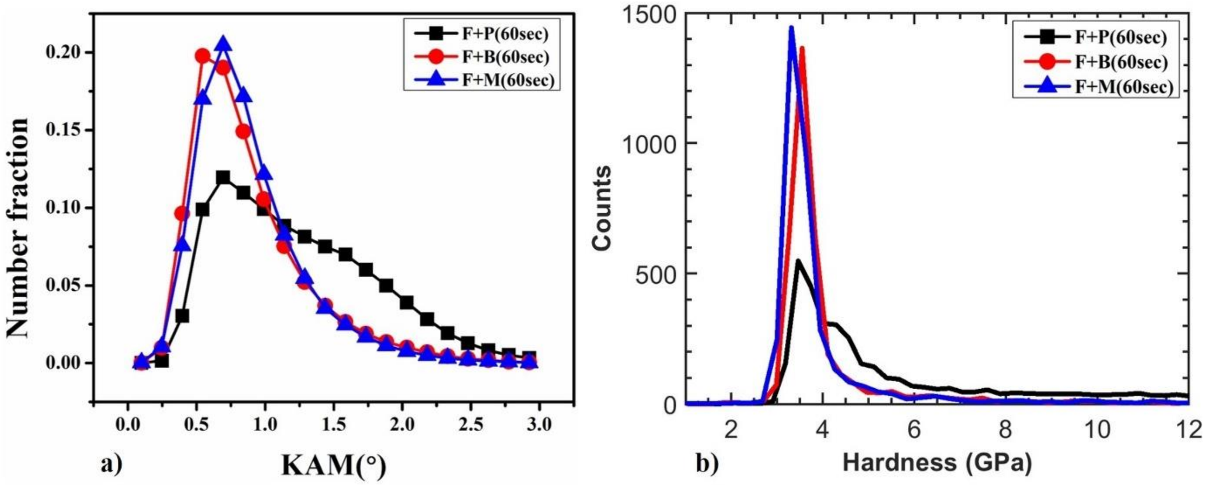

Figure 7-15: Comparison of (a) KAM histogram and (b) hardness histogram after intercritical annealing for 60s in samples with initial microstructure consisting of FP, FB and FM.

To further compare the hardness of recrystallized ferrite regions in FP with FB and FM, the hardness map of FP is deconvoluted into 3 bins using the KAM map as shown in Fig. 7-16. In the KAM map, the blue regions correspond to recrystallized grains. In order to distinguish the hardness of recrystallized and unrecrystallized regions, the deconvoluted map shows the recrystallized ferrite regions in blue, unrecrystallized ferrite regions in green and martensite in red. Subsequent to this deconvolution, hardness of recrystallized ferrite in FP is 3.7 GPa which agrees well with the corresponding value of 3.76 & 3.60 GPa obtained in FB and FM. This implies that the nature of ferrite after intercritical annealing is largely similar irrespective of the starting microstructure if sufficient recrystallization can be ensured.

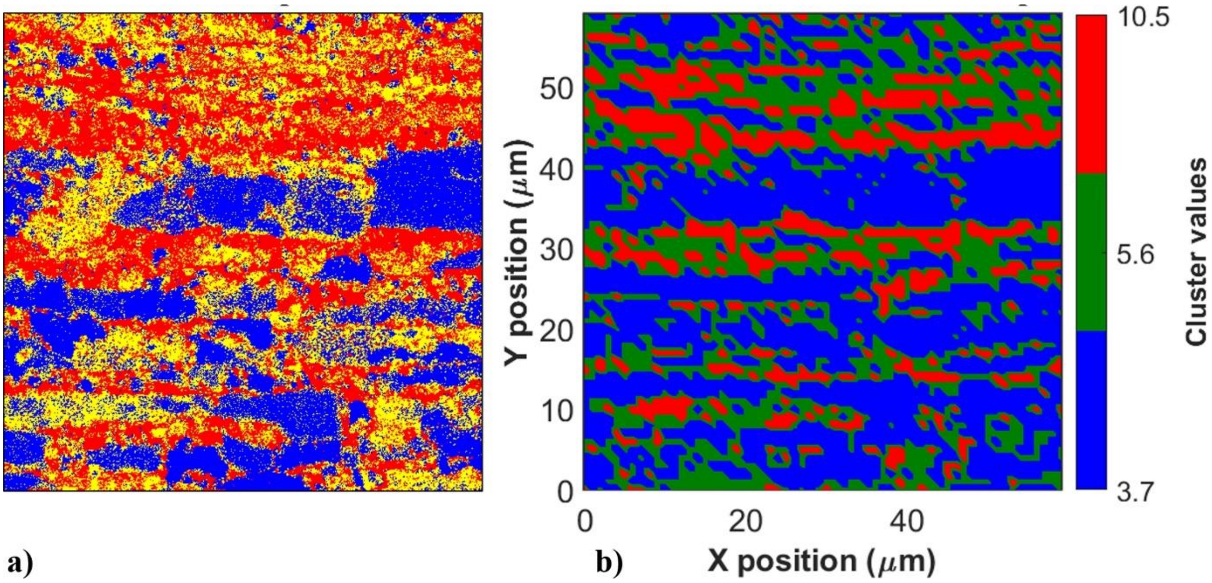

Figure 7-16: Comparison of (a) KAM map and (b) deconvoluted hardness map with 3 bins after intercritical annealing for 60s in sample with initial microstructure consisting of FP.

7.5 Summary and conclusions:

In this chapter, the effect of initial microstructure on the microstructural and mechanical property evolution during intercritical annealing is presented.

1. Dual phase ferrite-martensite microstructure was obtained starting with different initial microstructures consisting of cold rolled ferrite-pearlite (FP), ferrite-bainite (FB), and ferrite-martensite (FM), by intercritical annealing at 770^{o}C for different durations followed by water quenching.

2. The microstructural investigations show that in the case of FP, martensite formation kinetics is faster upon intercritical annealing compared to FB and FM, whereas ferrite recrystallization is retarded.
3. The hardness maps obtained from high-speed mapping show excellent agreement with the microstructural observations.
4. Micro-Vickers hardness measurements show a trend similar to nanoindentation although without showing the distinction between the constituents.
5. One to one correspondence between the KAM maps and hardness maps was observed.
6. The hardness maps are deconvoluted to obtain the hardness distribution of the individual constituents. Similar to the microstructural observations, the deconvoluted hardness histograms show significant ferrite recrystallization in FB and FM and more austenite to martensite transformation in the case of FP. This is attributed to higher stored energy in cold rolled FB and FM, driving recrystallization and consequently slowing down transformation, whereas the reverse is true for FP. In the case of FP, the faster cementite spheroidization enables faster austenite formation which in turn slows down ferrite recrystallization.

7.6 References:

[1] A. Karmakar, M. Ghosh, D. Chakrabarti, Cold-rolling and inter-critical annealing of low-carbon steel: Effect of initial microstructure and heating-rate, Mater. Sci. Eng. A. 564 (2013) 389–399. https://doi.org/10.1016/j.msea.2012.11.109.

[2] X.L. Cai, J. Feng, W.S. Owen, The dependence of some tensile and fatigue properties

of a dual-phase steel on its microstructure, Metall. Trans. A. 16 (1985) 1405–1415. https://doi.org/10.1007/BF02658673.

[3] Jose Gerbase-Filho, Mechanical properties of dual phase steels, Mater. Sci. Eng. (1979).

[4] F.M. Al-Abbasi, J.A. Nemes, Micromechanical modeling of dual phase steels, Int. J. Mech. Sci. 45 (2003) 1449–1465. https://doi.org/10.1016/j.ijmecsci.2003.10.007.

[5] A. Fallahi, Microstructure property correlation of dual phase steels produced by controlled rolling process, J. Mater. Sci. Technol. 18 (2002) 451–454.

[6] S. Fiore, B. Ruffino, M.C. Zanetti, Automobile Shredder Residues in Italy: Characterization and valorization opportunities, Waste Manag. 32 (2012) 1548–1559. https://doi.org/10.1016/j.wasman.2012.03.026.

[7] C. Revilla, B. López, J.M. Rodriguez-Ibabe, Carbide size refinement by controlling the heating rate during induction tempering in a low alloy steel, Elsevier Ltd, 2014. https://doi.org/10.1016/j.matdes.2014.05.053.

[8] F.J. Humphreys, M. Hatherly, Recrystallization and Related Annealing Phenomena, Recryst. Relat. Annealing Phenom. (2012) 1–497. https://doi.org/10.1016/C2009-0-07986-0.

[9] V. Massardier, A. Ngansop, D. Fabrègue, J. Merlin, Identification of the parameters controlling the grain refinement of ultra-rapidly annealed low carbon Al-killed steels, Mater. Sci. Eng. A. 527 (2010) 5654–5663. https://doi.org/10.1016/j.msea.2010.05.024.

[10] M. Ferry, D. Muljono, D.P. Dunne, Recrystallization kinetics of low and ultra low carbon steels during high-rate annealing, ISIJ Int. 41 (2001) 1053–1060.

https://doi.org/10.2355/isijinternational.41.1053.

[11] J. Huang, W.J. Poole, M. Militzer, Austenite formation during intercritical annealing, Metall. Mater. Trans. A Phys. Metall. Mater. Sci. 35 A (2004) 3363–3375. https://doi.org/10.1007/s11661-004-0173-x.

[12] C. Philippot, J. Drillet, P. Maugis, V. Hebert, M. Dumont, Austenite formation in a ferrite/martensite cold-rolled microstructure during annealing of advanced high-strength steels, Metall. Res. Technol. 111 (2014) 3–8. https://doi.org/10.1051/metal/2014004.

[13] I. Pushkareva, Microstructural evolution of Dual Phase steel . Improvement of damage resistance To cite this version : HAL Id : tel-01748776 soutenance et mis à disposition de l ’ ensemble de la Contact : ddoc-theses-contact@univ-lorraine.fr, (2018).

[14] N.K. Balliger, T. Gladman, Work hardening of dual-phase steels, Met. Sci. 15 (1981) 95–108. https://doi.org/10.1179/030634581790426615.

[15] M. Mazinani, W.J. Poole, Effect of martensite plasticity on the deformation behavior of a low-carbon dual-phase steel, Metall. Mater. Trans. A Phys. Metall. Mater. Sci. 38 (2007) 328–339. https://doi.org/10.1007/s11661-006-9023-3.

[16] G. Avramovic-Cingara, Y. Ososkov, M.K. Jain, D.S. Wilkinson, Effect of martensite distribution on damage behaviour in DP600 dual phase steels, Mater. Sci. Eng. A. 516 (2009) 7–16. https://doi.org/10.1016/j.msea.2009.03.055.

[17] J. Gautam, A. Miroux, J. Moerman, L. Kestens, TNR dependent hot rolling microstructure and texture development in c-Mn dual phase and HSLA steels, Defect Diffus. Forum. 391 (2019) 120–127. https://doi.org/10.4028/www.scientific.net/DDF.391.120.

[18] S. Janakiram, J.P. Gautam, A. Miroux, J. Moerman, L. Kestens, Microstructure and Texture Control in Cold Rolled High Strength Steels, Diffus. Found. 22 (2019) 84–93. https://doi.org/10.4028/www.scientific.net/df.22.84.

[19] S.I. Wright, M.M. Nowell, EBSD image quality mapping, Microsc. Microanal. 12 (2006) 72–84. https://doi.org/10.1017/S1431927606060090.

[20] P.R.& F.F. S. ZAEFFERER∗, EBSD as a tool to identify and quantify bainite and ferrite in low-alloyed Al-TRIP steels, J. OfMicroscopy. 230 (2008) 499–508. https://doi.org/https://doi.org/10.1111/j.1365-2818.2008.02010.x.

[21] J.J. Roa, P. Sudharshan Phani, W.C. Oliver, L. Llanes, Mapping of mechanical properties at microstructural length scale in WC-Co cemented carbides: Assessment of hardness and elastic modulus by means of high speed massive nanoindentation and statistical analysis, Int. J. Refract. Met. Hard Mater. 75 (2018) 211–217. https://doi.org/10.1016/j.ijrmhm.2018.04.019.

Chapter 8 Summary, conclusions and future scope of work

This chapter provides an overall summary of the investigations and conclusions drawn thereof, during the various stages of thermomechanical processing of an Advanced High-Strength Steel (AHSS). The focus is on the key processing steps of AHSS sheets such as hot rolling and coiling, cold rolling, recrystallization, and intercritical annealing. Three different AHSS sheets with identical chemical composition but different microstructures were obtained by hot rolling followed by coiling at different conditions, all featuring ferrite as the matrix but different secondary constituent/phase such as pearlite, bainite, or martensite. These samples were subsequently cold rolled to different levels and subjected to annealing treatment independently in recrystallization and intercritical regime.

Observations and analyses of microstructure and mechanical properties was carried out after hot rolling and coiling, cold rolling, and subsequent annealing at temperatures of 725ºC and 770ºC, utilizing techniques such as SEM, EBSD, Vickers microhardness, and high speed nanoindentation mapping. A qualitative correlation was successfully established between observed microstructure as revealed by SEM / EBSD, and corresponding mechanical properties assessed through Vickers microhardness and nanoindentation mapping at different length scales. While a detailed summary and conclusions from the investigations on each processing step are provided at the end of the corresponding chapter, here we present a representative example as shown in Fig. 8-1 and 8-2 to highlight the key findings and also to compare across the different processing steps as shown in Fig. 8-3.

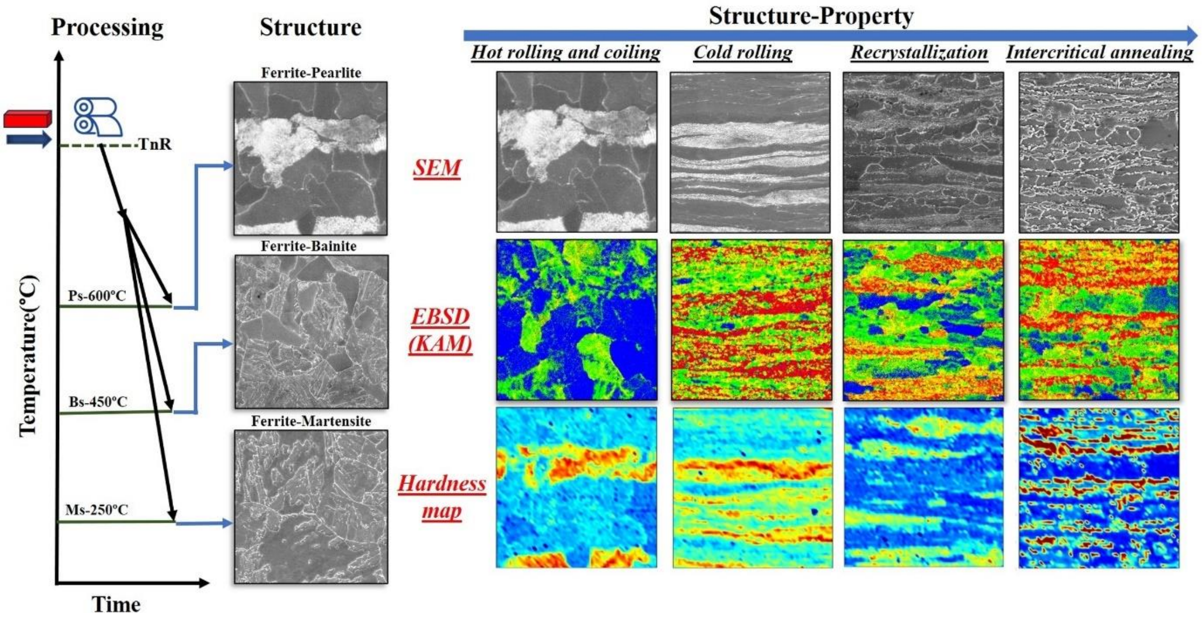

Figure 7-17: Representative example showing the thermo-mechanical processing steps, microstructure and hardness maps. The correlation between structure and property at the micrometer length scale can be clearly observed in all the cases.

Figure 8-1 shows a schematic of the initial processing steps that includes hot rolling above TnR followed by cooling at different rates and coiling at different temperatures to obtain microstructures consisting of ferrite-pearlite (FP), ferrite-bainite (FB) and ferrite-martensite (FM). The SEM micrographs after hot rolling and coiling are shown in the figure. In the case of ferrite-pearlite, a banded morphology and a coarse microstructure is observed with clear distinction between the ferrite and pearlite largely due to the higher processing temperatures and near equilibrium conditions. In the case of ferrite-bainite, a mixture of large grains of bulk ferrite and a finely mixed region of bainite/carbide and ferrite is observed, whereas in the case of ferrite-martensite, finely distributed martensite throughout the ferrite matrix is observed.

Representative EBSD-KAM maps and hardness maps for the regions shown in the SEM micrographs are also shown. Excellent correlation between the SEM micrographs and hard ness maps can be observed in all the cases. The correlation between KAM and hardness is good in certain cases and unclear in few others. In order to quantify the hardness of individual constituents and understand their evolution with processing, the hardness maps are deconvoluted using a clustering algorithm as shown in the example in Fig. 8-2. The hardness map corresponds to ferrite-pearlite, wherein the low hardness regions correspond to ferrite and high hardness regions to pearlite. The deconvoluted map algorithmically identifies the two regions – ferrite (blue) and pearlite (red) and enables representation of the deconvoluted data in terms of histograms as also shown in the figure. Representative histograms of the ferrite and the secondary constituent for each processing step is also shown. The shift in the peak position and width with processing can be observed from the histograms.

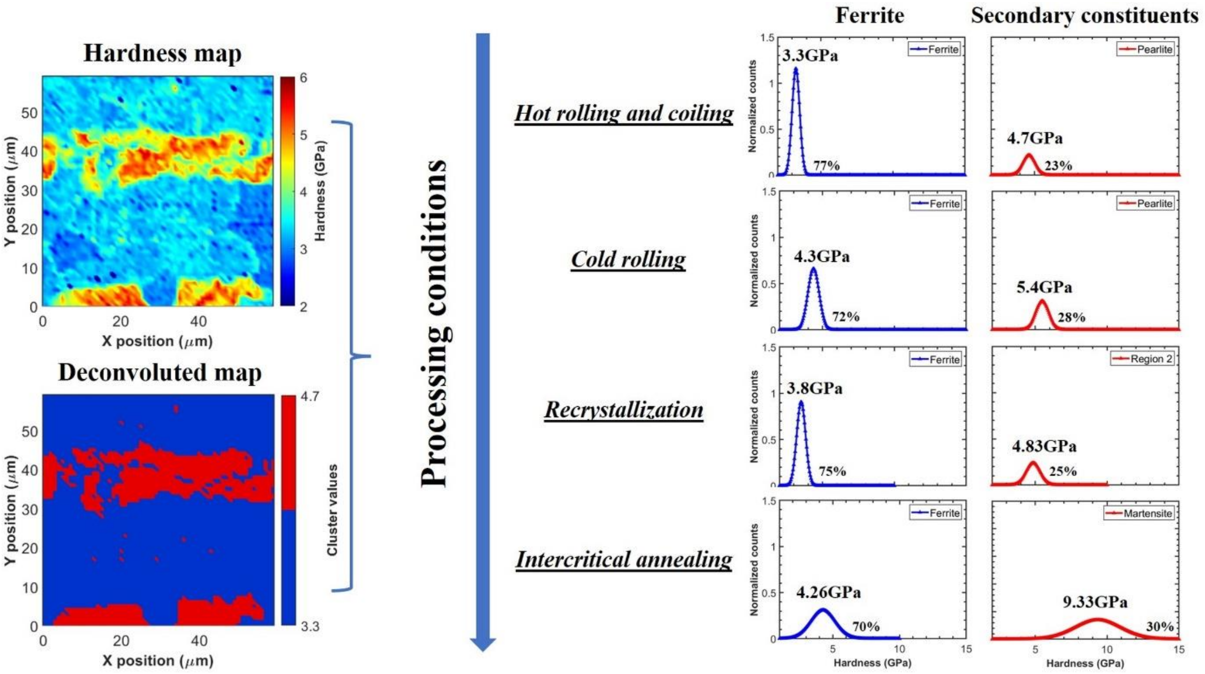

Figure 7-18: Quantification of the hardness of individual constituents by deconvolution.

Given the excellent correlation between the microstructure and local hardness (Fig. 8-1), and the ability of the clustering algorithm to identify and provide quantitative estimates of the hardness of the individual constituents (Fig. 8-2), a plot showing the evolution of the hardness of ferrite and secondary constituent during different stages of processing can be used to present a comprehensive picture. Such a plot is shown in Fig. 8-3, wherein the hardness of ferrite and the secondary constituent is plotted for all the processing steps investigated in this work. In the case of ferrite shown in Fig. 8-3(a), the hardness is higher after hot rolling and coiling in the case of FM due to the fine distribution of the hard martensite phase compared to FB and FP. After subsequent cold rolling, hardness increases in all the cases due to work hardening. During recrystallization, the hardness of ferrite in FB and FM reduce immediately due to the higher stored energy during cold working of FB and FM that have finer distribution of harder phase. In contrast, the ferrite in FP shows delayed recrystallization. Interestingly, after intercritical annealing, the hardness of ferrite in FB and FM is lower than that of FP. This is due to the retardation of ferrite recrystallization in the intercritical regime as was also observed in the recrystallization regime. However, if we only consider the hardness of the recrystallized grains in FP as shown by the yellow symbols, its hardness matches with that of FB and FM. This implies that the nature of ferrite after intercritical annealing is largely similar irrespective of the starting microstructure if sufficient recrystallization can be ensured.

In the case of the secondary constituent shown in Fig. 8-13 (b), the hardness is similar after hot rolling and coiling and shows an increasing trend with cold rolling. This implies that the hardness measurements of the secondary phase are slightly affected by the hardening of the surrounding matrix or ferrite. During recrystallization, the hardness in case of FB and FM drops drastically due to their dissolution and subsequently rises due to carbide formation and coarsening. This process is delayed in the case of FP. Finally, the hardness of martensite formed after intercritical annealing is similar in all cases as the nominal carbon content is similar. The delayed ferrite recrystallization in case of FP has important implications for austenite-martensite transformation as the unrecrystallized regions along with quick cementite spheroidization leads to greater transformation in the case of FP. While this plot does not show the volume fractions, the martensite volume fraction and formation kinetics are faster in case of FP.

The comprehensive study covering various processing steps and extensive microstructural and mechanical property measurements presented in this work along with hardness deconvolution, establish a robust framework to explore processing-structure-property correlation in high strength steels that can be gainfully used to tweak the processing to obtain the desired properties. .

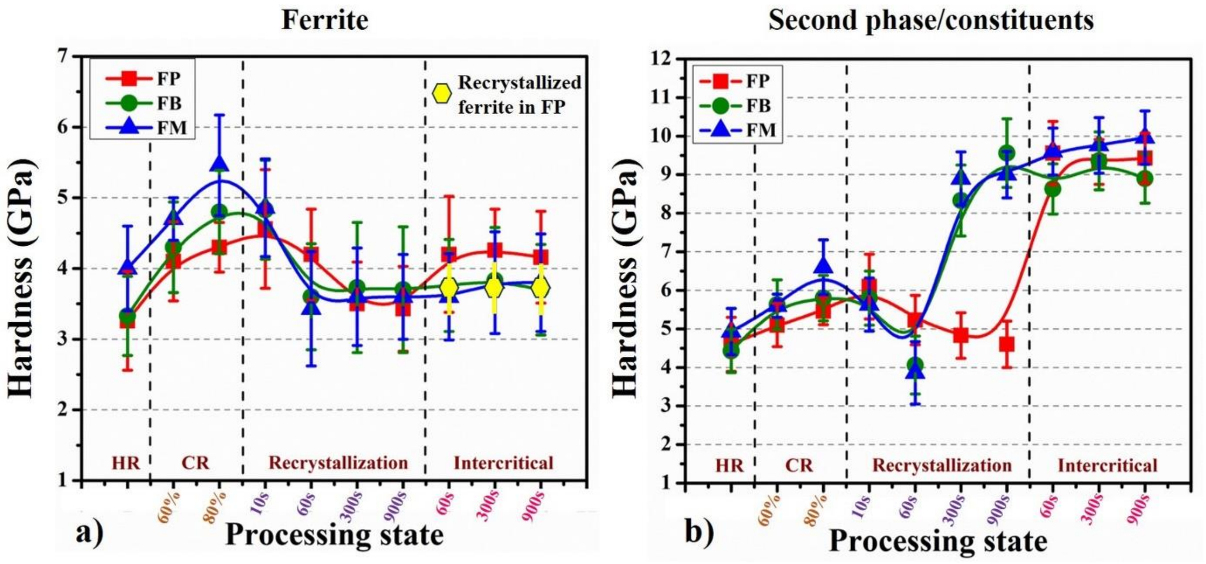

Figure 7-19: Deconvoluted hardness during various stages of processing in case of (a) bulk ferrite and (b) secondary phase / constituents for samples with initial microstructure consisting of FP, FB, and FM.

8.1 Future scope of work:

The study has provided a framework to establish correlation between microstructure and mechanical properties at the micrometer length scale for several key steps in thermomechanical processing of AHSS, employing techniques such as scanning electron microscopy and nanoindentation. However, for a more in-depth analysis of structural changes at the submicron level, including the defect and second phase interaction, advanced characterization using Transmission Electron Microscopy (TEM) is warranted. On the other hand, while mechanical properties at the micrometer length scale is investigated in this work using nanoindentation, uniaxial testing at the macro and micro scale, will provide insights on the overall strength and ductility under varying processing conditions.

With regards to data analysis, in this work the nanoindentation mapping data was deconvoluted using the k-means clustering algorithm. While this method is robust and has been widely used, the potential use of other algorithms for deconvoluting data from multiphase steels should be explored. Furthermore, in this work, the correlations were established based on the distributions obtained from the deconvoluted data. However, a pixel level correlation between the microstructure and property, although very challenging, should be undertaken.

Assessment of microstructure and mechanical properties of dual phase C-Mn AHSS during thermomechanical processing via electron microscopy and high speed nanoindentation

by Akash Chavan

Librarian
Indira Gandhi Memorial Library
UNIVERSITY OF HYDERABAD
Central University P.O.
HYDERABAD-500 046.

Submission date: 01-Apr-2024 02:59PM (UTC+0530)
Submission ID: 2336793309
File name: Akash_Thesis_Final_-_Plagarism_check_28_march_2024.pdf (12.42M)
Word count: 30204
Character count: 172665

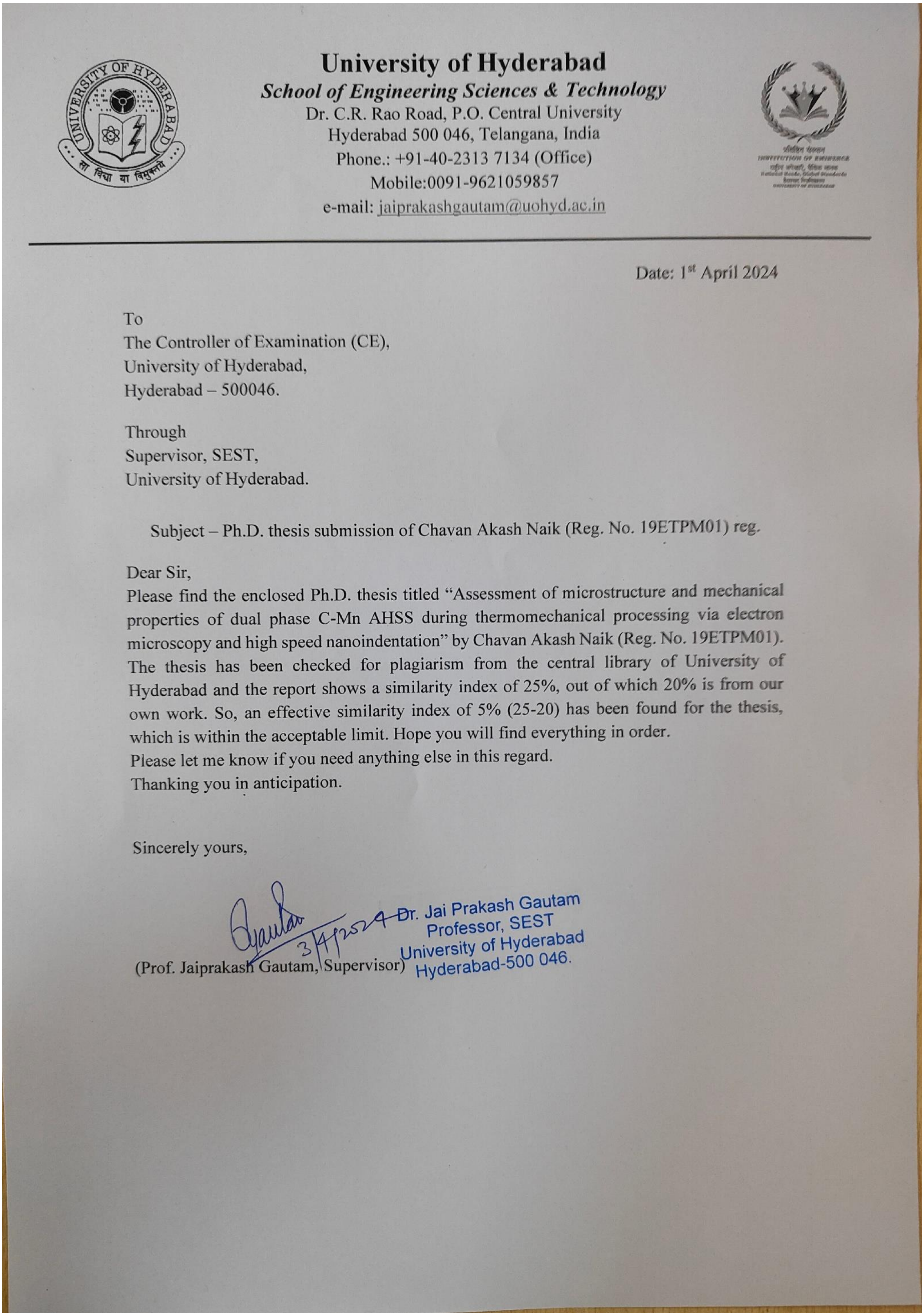

University of Hyderabad
School of Engineering Sciences & Technology
Dr. C.R. Rao Road, P.O. Central University
Hyderabad 500 046, Telangana, India
Phone.: +91-40-2313 7134 (Office)
Mobile:0091-9621059857
e-mail: jaiprakashgautam@uohyd.ac.in

Date: 1st April 2024

To
The Controller of Examination (CE),
University of Hyderabad,
Hyderabad – 500046.

Through
Supervisor, SEST,
University of Hyderabad.

Subject – Ph.D. thesis submission of Chavan Akash Naik (Reg. No. 19ETPM01) reg.

Dear Sir,
Please find the enclosed Ph.D. thesis titled "Assessment of microstructure and mechanical properties of dual phase C-Mn AHSS during thermomechanical processing via electron microscopy and high speed nanoindentation" by Chavan Akash Naik (Reg. No. 19ETPM01). The thesis has been checked for plagiarism from the central library of University of Hyderabad and the report shows a similarity index of 25%, out of which 20% is from our own work. So, an effective similarity index of 5% (25-20) has been found for the thesis, which is within the acceptable limit. Hope you will find everything in order.
Please let me know if you need anything else in this regard.
Thanking you in anticipation.

Sincerely yours,

Gautam 3/4/2024

Dr. Jai Prakash Gautam
Professor, SEST
University of Hyderabad
Hyderabad-500 046.

(Prof. Jaiprakash Gautam, Supervisor)

Assessment of microstructure and mechanical properties of dual phase C-Mn AHSS during thermomechanical processing via electron microscopy and high speed nanoindentation

ORIGINALITY REPORT

25%	5%	20%	5%
SIMILARITY INDEX	INTERNET SOURCES	PUBLICATIONS	STUDENT PAPERS

PRIMARY SOURCES

✓ 1	Chavan Akash Naik, B.K. Sarath Kumar, S. Harita, Suuraj Roshan, P. Sudharshan Phani, Jai Prakash Gautam. "Assessment of structure-property relationships at the micrometer length scale in dual phase steels by electron microscopy and nanoindentation", Materials Today Communications, 2023 Publication	14%
✓ 2	Submitted to University of Hyderabad, Hyderabad Student Paper	4%
3	S. Janakiram, P. Sudharshan Phani, Govind Ummethala, Hima Viswa Jagdeesh, Sairam K. Malladi, J. Gautam, Leo A.I. Kestens. "Insights on early recovery kinetics in ferrite - pearlite cold rolled high strength sheet steels", Materials Characterization, 2022 Publication	1%
✓ 4	nanospd8.iisc.ac.in Internet Source	1%

Dr. Jai Prakash Gautam
Professor, SEST
University of Hyderabad
Hyderabad-500 046.

Dr. Jai Prakash Gautam
Professor, SEST
University of Hyderabad
Hyderabad-500 046.

Dr. Jai Prakash Gautam
Professor, SEST
University of Hyderabad
Hyderabad-500 046.

Scanned with ACE Scanner

5	Chavan Akash Naik, B.K. Sarath Kumar, S. Harita, Suuraj Roshan, S. Janakiram, P. Sudharshan Phani, Jai Prakash Gautam. "Assessment of structure-property relationships at the micrometer length scale in dual phase steels by electron microscopy and nanoindentation", Materials Today Communications, 2024 Publication	1%
6	biblio.ugent.be Internet Source	<1%
7	worldwidescience.org Internet Source	<1%
8	"HSLA Steels 2015, Microalloying 2015 & Offshore Engineering Steels 2015", Springer Science and Business Media LLC, 2016 Publication	<1%
9	www.researchgate.net Internet Source	<1%
10	www.mdpi.com Internet Source	<1%
11	Advanced High Strength Sheet Steels, 2015. Publication	<1%
12	S. Janakiram, P. Sudharshan Phani, Govind Ummethala, Sairam K. Malladi, J. Gautam, Leo A.I. Kestens. "New insights on recovery and	<1%

Dr. Jai Prakash Gautam
Professor, SEST
University of Hyderabad
Hyderabad-500 046.

Dr. Jai Prakash Gautam
Professor, SEST
University of Hyderabad
Hyderabad-500 046.

Scanned with ACE Scanner

	early recrystallization of ferrite-pearlite banded cold rolled high strength steels by high speed nanoindentation mapping", Scripta Materialia, 2021 Publication	
13	B. Vignesh, W.C. Oliver, G. Siva Kumar, P. Sudharshan Phani. "Critical assessment of high speed nanoindentation mapping technique and data deconvolution on thermal barrier coatings", Materials & Design, 2019 Publication	<1 %
14	newsletterkim.or.kr Internet Source	<1 %
15	link.springer.com Internet Source	<1 %
16	I.V. Samarasekera. "Hot Rolling", Elsevier BV, 2001 Publication	<1 %
17	G. R. Speich, V. A. Demarest, R. L. Miller. "Formation of Austenite During Intercritical Annealing of Dual-Phase Steels", Metallurgical Transactions A, 1981 Publication	<1 %
18	www.escholar.manchester.ac.uk Internet Source	<1 %
19	iopscience.iop.org Internet Source	<1 %

Dr. Jai Prakash Gautam
Professor, SEST
University of Hyderabad
Hyderabad-500 046.

Scanned with ACE Scanner

20	www.hereon.de Internet Source	<1%
21	www.science.gov Internet Source	<1%
22	Deekshith G. Kalali, Harita Seekala, P. Sudharshan Phani, K. Bhanu Sankara Rao, Koteswararao V. Rajulapati. "High speed nanoindentation aided correlative study between local mechanical properties and chemical segregation in equiatomic MoNb and MoNbTi alloys", Journal of Materials Research, 2023 Publication	<1%
23	Tekkaya, A.E., J.M. Allwood, P.F. Bariani, S. Bruschi, J. Cao, S. Gramlich, P. Groche, G. Hirt, T. Ishikawa, C. Löbbe, J. Lueg-Althoff, M. Merklein, W.Z. Misiolek, M. Pietrzyk, R. Shivpuri, and J. Yanagimoto. "Metal forming beyond shaping: Predicting and setting product properties", CIRP Annals - Manufacturing Technology, 2015. Publication	<1%
24	Y. Mazaheri, A. Kermanpur, A. Najafizadeh, A. Ghatei Kalashami. "Kinetics of Ferrite Recrystallization and Austenite Formation During Intercritical Annealing of the Cold-Rolled Ferrite/Martensite Duplex Structures",	<1%

Dr. Jai Prakash Gautam
Professor, SEST
University of Hyderabad
Hyderabad-500 046.

	Metallurgical and Materials Transactions A, 2016 Publication	
25	unsworks.unsw.edu.au Internet Source	<1 %
26	assets.researchsquare.com Internet Source	<1 %
27	Ali Bayram, Agah Uğuz, Murat Ula. "Effects of Microstructure and Notches on the Mechanical Properties of Dual-Phase Steels", Materials Characterization, 1999 Publication	<1 %
28	Ankita Bhattacharya, Anupam Bagdi, Debdulal Das. "Influence of microstructure on high-stress abrasive wear behaviour of a microalloyed steel", Perspectives in Science, 2016 Publication	<1 %
29	M. Sebastiani, R. Moscatelli, F. Ridi, P. Baglioni, F. Carassiti. "High-resolution high-speed nanoindentation mapping of cement pastes: Unravelling the effect of microstructure on the mechanical properties of hydrated phases", Materials & Design, 2016 Publication	<1 %

Dr. Jai Prakash Gautam
Professor, SEST
University of Hyderabad
Hyderabad-500 046.

Scanned with ACE Scanner

30	Tarek M. Belgasam, Hussein M. Zbib. "Microstructure Optimization of Dual-Phase Steels Using a Representative Volume Element and a Response Surface Method: Parametric Study", Metallurgical and Materials Transactions A, 2017 Publication	<1 %
31	Ghaheri, Ali, Ali Shafyei, and Mehrdad Honarmand. "Effects of inter-critical temperatures on martensite morphology, volume fraction and mechanical properties of dual-phase steels obtained from direct and continuous annealing cycles", Materials & Design, 2014. Publication	<1 %
32	Surajit Kumar Paul. "Effect of material inhomogeneity on the cyclic plastic deformation behavior at the microstructural level: micromechanics-based modeling of dual-phase steel", Modelling and Simulation in Materials Science and Engineering, 2013 Publication	<1 %
33	etd.library.vanderbilt.edu Internet Source	<1 %
34	scholars.wlu.ca Internet Source	<1 %

Dr. Jai Prakash Gautam
Professor, SEST
University of Hyderabad
Hyderabad-500 046.

Scanned with ACE Scanner

35	Ali Ghatei Kalashami, Ahmad Kermanpur, Abbas Najafizadeh, Yousef Mazaheri. "Effect of Nb on Microstructures and Mechanical Properties of an Ultrafine-Grained Dual Phase Steel", Journal of Materials Engineering and Performance, 2015 Publication	<1%
36	Saroj Kumar Basantia, Ankita Bhattacharya, Niloy Khutia, Debdulal Das. "Plastic Behavior of Ferrite–Pearlite, Ferrite–Bainite and Ferrite–Martensite Steels: Experiments and Micromechanical Modelling", Metals and Materials International, 2019 Publication	<1%
37	Emil Evin, Ján Kepič, Katarína Buriková, Miroslav Tomáš. "The Prediction of the Mechanical Properties for Dual-Phase High Strength Steel Grades Based on Microstructure Characteristics", Metals, 2018 Publication	<1%
38	M. A. Mostafaei, M. Kazeminezhad. "Microstructural evolution during ultra-rapid annealing of severely deformed low-carbon steel: strain, temperature, and heating rate effects", International Journal of Minerals, Metallurgy, and Materials, 2016 Publication	<1%

Dr. Jai Prakash Gautam
Professor, SEST
University of Hyderabad
Hyderabad-500 046.

Scanned with ACE Scanner

39	B.-C. Hwang. "Effects of ferrite grain size and martensite volume fraction on dynamic deformation behaviour of 0·15C–2·0Mn–0·2Si dual phase steels", Materials Science and Technology, 08/01/2005 Publication	<1%
40	Calcagnotto, M.. "Deformation and fracture mechanisms in fine- and ultrafine-grained ferrite/martensite dual-phase steels and the effect of aging", Acta Materialia, 201101 Publication	<1%
41	idr.l4.nitk.ac.in Internet Source	<1%
42	Marion Calcagnotto, Dirk Ponge, Dierk Raabe. "Microstructure Control during Fabrication of Ultrafine Grained Dual-phase Steel: Characterization and Effect of Intercritical Annealing Parameters", ISIJ International, 2012 Publication	<1%
43	Muransky, O.. "In situ neutron diffraction investigation of the collaborative deformation-transformation mechanism in TRIP-assisted steels at room and elevated temperatures", Acta Materialia, 200808 Publication	<1%

Dr. Jai Prakash Gautam
Professor, SEST
University of Hyderabad
Hyderabad-500 046.

Scanned with ACE Scanner

44	Suehiro, Masayoshi. "A Mathematical Model for Predicting Microstructural Evolution and Mechanical Properties of Hot-Rolled Steels", Dekker Mechanical Engineering, 2003. Publication	<1%
45	Submitted to Higher Education Commission Pakistan Student Paper	<1%
46	Ji, F. Q., C. N. Li, S. Tang, and G. D. Wang. "Interphase precipitation of nanometre-sized carbides in Ti bearing steels", Materials Research Innovations, 2015. Publication	<1%
47	Zhang, Fan, Annie Ruimi, and David P. Field. "Phase Identification of Dual-Phase (DP980) Steels by Electron Backscatter Diffraction and Nanoindentation Techniques", Microscopy and Microanalysis, 2016. Publication	<1%
48	Zhuang Li, Di Wu. "Effects of finishing rolling temperatures and reduction on the mechanical properties of hot rolled multiphase steel", Journal of Zhejiang University-SCIENCE A, 2007 Publication	<1%

Dr. Jai Prakash Gautam
Professor, SEST
University of Hyderabad
Hyderabad-500 046.

Scanned with ACE Scanner